UNIVERSITÉ DE GENÈVE
Département de physique
nucléaire et corpusculaire
CERN

FACULTÉ DES SCIENCES
Prof. Alain Blondel

Dr. Cristobal Padilla

Performance Studies of the High Level Electron Trigger of ATLAS

THÈSE

présentée à la Faculté des sciences de l'Université de Genève
pour obtenir le grade de Docteur ès Sciences, mention physique

par

Manuel Díaz Gómez

d'Espagne

Thèse N° 3739

GENÈVE

2006

La Faculté des sciences, sur le préavis de Messieurs A. BLONDEL, professeur ordinaire et directeur de thèse (Département de physique nucléaire et corpusculaire), C. PADILLA, docteur (Organisation européenne pour la Recherche nucléaire – Département de physique – Genève, Suisse), A. CLARK, professeur ordinaire (Département de physique nucléaire et corpusculaire), M. POHL, professeur ordinaire (Département de physique nucléaire et corpusculaire), et N. ELLIS, docteur (Organisation européenne pour la Recherche nucléaire – Genève, Suisse), autorise l'impression de la présente thèse, sans exprimer d'opinion sur les propositions qui y sont énoncées.

Genève, le 12 mai 2006

Le Doyen, Pierre SPIERER

Dedicated to
my mother

Performance Studies of the High Level Electron Trigger of ATLAS

Manuel Díaz Gómez

Submitted for the degree of Doctor of Philosophy
February 2006

Abstract

The work presented here was carried out at the European Organization for Nuclear Research (CERN) in the framework of the ATLAS collaboration which is building a general-purpose detector at the Large Hadron Collider (LHC). The main goal of the ATLAS experiment is to search for the Higgs boson (a particle predicted by the Standard Model) and to chart the territory up to the TeV scale in cms energy. As the theory, the instrumentation used to probe the new realms and to verify the predictions of the theory has likewise grown in its complexity. HEP experiments in general are craving for the investment of knowledge into the construction of detector elements, into analysis techniques, electronics and computing.

This thesis presents most of my work in the High Level Triggers (HLT) group of the ATLAS collaboration, performed during the three years and a half of my engagement. One should understand that ATLAS will begin its operation in the year 2007 and that it is currently in its last experiment-building phase. While the ATLAS physics aims were the determinant of all the goals set in the process, the results can only form a skeleton on which the flesh of real data will attach to form the body of physical results.

My work focused on the identification of isolated high transverse momentum electrons ($p_T \geq 25\,GeV/c$) by the HLT system of ATLAS, which is essential for physics studies at the LHC. After the First Level Trigger (LVL1), The HLT system (formed by the Level 2 (LVL2) trigger and the Event Filter (EF)) has a critical role in the electron identification performance. Indeed, the trigger must be able to select electrons in a very efficient manner, while keeping the background rate to a minimum. Typical examples are the searches for decays of the Higgs boson into four electrons $H \rightarrow ZZ^{(*)} \rightarrow 4e$, with a cross section of $0.2\,fb$ for a Higgs mass of $130\,GeV/c^2$, the production of Z with decays $Z \rightarrow e^+e^-$ ($\sigma = 1.5\,\text{nb}$), or the production of W with decays $W \rightarrow e\nu$ ($\sigma = 1.515\,\text{nb}$). The QCD di-jet cross section being of the order of $1\,mb$, to obtain an inclusive electron signal, a rejection factor 10^7 is required on QCD jets.

After a complete overview of the LHC environment, the ATLAS detector, and the ATLAS trigger system (chapters 1 and 2), chapter 3 presents a Monte Carlo

study of the HLT single electron trigger performance and its rejection capability against QCD jets, using the electromagnetic and the hadronic calorimeter as well as the inner detector systems. The performance of the electron triggers has been analyzed for low, $2 \times 10^{33} \, cm^{-2} \, s^{-1}$ (design, $10^{34} \, cm^{-2} \, s^{-1}$) luminosity, and using a more up to date detector description and a more realistic tuning of the MC generators. A final LVL2 rate of $137 \pm 12 \, Hz (420 \pm 16 \, Hz)$ for an electron efficiency of $86.6 \pm 0.6 (90.6 \pm 0.6)$ for the e25i(e30i) trigger has been found. At the EF, a rate of $30 \pm 5 \, Hz$ ($176 \pm 11 \, Hz$) and an electron efficiency of $79.0 \pm 0.7 (78.2 \pm 0.7)$ has been obtained. These results are comparable to the rate estimates obtained in earlier studies. As a cross-check, the efficiency to select $W \rightarrow e\nu$ events for which the electron has a $p_T > 25 \, GeV$ at generator level is $(90.6 \pm 0.9\%)$ after LVL2 and $(79.8 \pm 1.2\%)$ after EF. These results show that the HLT software and the selection algorithms are working satisfactory.

As the trigger efficiency will be an important parameter in several physics analyses, it is important to have independent methods of estimating it, depending as little as possible on the Monte Carlo description of the detector and running conditions, as this is necessarily incomplete. Indeed, for the energies and interaction rates expected at the LHC, the background components, and more generally, the underlying interaction physics are only approximatively known, and therefore uncertainties up to a factor of 5 can be expected in the Monte Carlo predictions. Furthermore, the HLT event selection is a complex online proccess, which is itself integrated in the ATLAS Data Acquisition (DAQ) system, where many factors could act as a potential source of inefficiencies (network related problems, hardware failures, buffer overflows, etc.). A new procedure to estimate the HLT electron trigger efficiency using $Z \rightarrow e^+e^-$ data is described in chapter 4. This method was tested on a $Z \rightarrow e^+e^-$ Monte Carlo sample resulting in an efficiency of 87.0% for the particular set of cuts used in the e25i signature. The same value was found by counting simulated events selected by this signature. Moreover, assuming an instantaneous luminosity of $10^{33} \, cm^{-2} \, s^{-1}$, for a $Z \rightarrow e^+e^-$ cross section of 1.515 nb, the method can provide an estimate for the overall electron trigger efficiency with a statistical uncertainty of less that $\sim 3\%$, after 1 hour of data acquisition. The robustness of the method was tested against different levels of background contribution. The QCD di-jet reconstructed invariant mass profile, assumed to be the main source of noise, was normalized to arbitrary large values so that it represented up to 60% of the signal under the $Z \rightarrow e^+e^-$ mass window. For the equivalent of ~ 1hour of data acquisition, the calculated efficiency was found the same, within the statistical uncertainty, for each background scenario. In addition, an upper limit to the systematic error contribution due to different background substraction methods was found to be $\sim 0.55\%$, and therefore it is not expected to countribute significantly to the overall uncertainty.

Test beam periods are of great importance during the research and development

period of a detector, since they represent a great opportunity to face and solve unexpected problems that might arise in a later stage of the detector operation. The Combined Test Beam (CTB) activity carried out between the spring and fall of 2004 was particularly important, because small sections of all the ATLAS subdetectors using final or quasi-final readout electronics were integrated together for the first time with the Trigger and Data Acquisition system (TDAQ). Chapter 5 studies the e/π separation in the LVL2 trigger system using test beam electrons and pions at momenta of 20 and $50\,\mathrm{GeV/c}$. The results of this analysis are important, since this is the first and only occasion that a full slice of ATLAS has been assembled and tested before the full ATLAS detector becomes operational. Pure samples of electrons and pions have been obtained using Cherenkov counters and the TRT subdetector. These samples have been used as input to the LVL2 system, where the high-p_T single electron trigger algorithms have been executed. This study shows that using LVL2 calorimeter and calorimeter-track matching information, electron selection efficiencies of $\sim 90\%$ can be obtained while maintaining the pion fake rate at a level of 7 per mil.

May 26, 2006

Acknowledgments

It is a pleasure to thank the many people who made this thesis possible.

I cannot express my gratitude to Profs. Allan Clark and Nick Ellis, who supported me in a difficult moment of my career and opened me the doors of the brave and exciting new world of high energy physics.

I would like to thank my supervisor at Geneva University, Prof. Alain Blondel, for his nearly four years of supervision, for his wise advice, always delivered with a big smile, and especially for his availability and commitment to guide me through my doctoral research, as well as for the time he has spent reading the various drafts of this thesis.

I would also like to thank all my working colleagues at DPNC: Annie Leger and Daniel La Marra for all the nice moments we had debugging the capricious bits and short-circuited connections of the LAr ROD motherboards; Arno Straessner for all the fruitful discussions we had about the Zee channel; Imma Riu for her supervision at the begining of my thesis, her support and advice, and all the lifts she gave me to university and back to CERN. It was great working with you guys!.

Thanks to the DPNC secretaries Peggy Argentin, and Catherine Blanchard for taking care, always with a smile, of my chaotic administration of legal issues(health ensurance, work permit, etc.).

I am extremely grateful for the opportunity to work for the ATLAS experiment at CERN under the supervision of Dr. Cristobal Padilla. With his enthusiasm, his half-Andalusian sense of humor, and his great patience and availability to explain things clearly and simply, he contributed enormously to make all these research years a pleasant and fruitful experience. His critical comments on my work have played a major role in both the content and presentation of my discussion and arguments. Throughout my thesis-writing period, he provided encouragement, sound advice, good teaching, good company, and lots of good ideas. I would have been lost without him!.

I thank also my colleagues of the PESA group at CERN, especially Cibrán Santamarina, and Patricia Conde for all the good advice and all the many coffee and lunch hours we spent rebuilding the world from scratch.

I really appreciated the company, daily tips and cool easy-going character of my office-mate Eric Thomas. Wish you the best for the future!.

Thanks to all my mates here at CERN: Andi, praesi, Ed, Rob, Jonny, Etam,

Emlyn, Gianluca, Alex, etc.. for all the funky nights out and excellent moments we shared. Without you, life in Geneva would have been extremely boring.

My mother has been an inspiration throughout my life. She has always supported my dreams and aspirations making great efforts and sacrifices, and if I do say so myself, I think she did a fine job raising me. I'd like to thank her for all she is, and all she has done for me.

Thanks to my sister for coping with a non-expressive and grouchy brother. I miss having you around!

Thanks to the Bretaudeau clan for their love and support, and for accepting "un abroutie d'espagnol" as a family member.

Last but not least, I would like to thank my girlfriend Christelle for her love, company, understanding, and all the sacrifices she made throughout this period.

May 26, 2006

Contents

List of Figures

List of Tables

Chapter 1

Résumé

Le travail présenté ici a été réalisé au Centre Européen de Recherche Nucléaire (CERN) dans le cadre de la collaboration ATLAS, qui construit un détecteur d'usage universel auprès du grand collisionneur hadronique (LHC). Le but principal de l'expérience ATLAS est de rechercher le boson de Higgs (une particule prévue par le modèle théorique standard) et de dresser une carte énergétique jusqu'à 1 TeV, et au dela, dans l'énergie de cms. Comme la théorie, l'instrumentation employée pour étudier les nouvelles limites de la physique des hautes énergies, et pour vérifier les prévisions de la théorie, s'est développée avec la même complexité. Cette thèse représente la majeure partie de mon travail que j'ai realisé dans le groupe des déclenchements de haut niveau (HLT) de la collaboration ATLAS.

Mon travail s'est concentré sur l'identification des électrons isolés de haute impulsion transverse ($p_T \geq 25\,GeV$) par le système HLT d'ATLAS, qui est essentiel pour des études de physique au LHC. Après le premier déclenchement de niveau (LVL1), le système HLT (constitué par le déclenchement de niveau 2 (LVL2) et le filtre d'événement (EF)) a un rôle critique dans la méthode d'identification des électrons. En effet, le déclenchement doit pouvoir choisir des électrons d'une façon très efficace, tout en gardant le taux de bruit de fond à un minimum. Les exemples typiques sont les recherches sur la désintégration du boson de Higgs en quatre électrons $H \rightarrow ZZ^{(*)} \rightarrow 4e$, avec une coupe transverse de $0.2\,fb$ pour une masse de Higgs de $130\,GeV/c^2$, la production de Z avec désintégrations $Z \rightarrow e^+e^-$ ($\sigma = 1,5 \times 10^{-6}\,mb$), ou la production de W avec désintégrations $W \rightarrow e\nu$ ($\sigma = 1,5 \times 10^{-5}\,mb$). La coupe du di-jet QCD, étant de l'ordre de $1\,mb$, pour obtenir un signal inclusif d'électron, un facteur 10^7 de rejet est exigé sur des di-jets QCD.

Après une vue d'ensemble complète de l'environnement du LHC, du détecteur ATLAS, et de son système de déclenchement(dans les chapitres 1 et 2), le chapitre 3 présente une étude Monte Carlo sur la performance du système de déclenchement HLT d'électrons et de ses possibilités de rejet contre les di-jets QCD, en utilisant le calorimètre électromagnétique et hadronique aussi bien que les systèmes de détecteur central.

Comme l'efficacité de déclenchement sera un paramètre important dans de nom-

breuses analyses physiques, il est important d'avoir plusieurs méthodes d'évaluation indépendantes les unes des autres, dépendant le moins possible de la description Monte Carlo du détecteur et de ses conditions d'utilisation, puisque cette méthode est forcément incomplète. Une nouvelle méthode pour estimer l'efficacité du système de déclenchement d'électron HLT, employant des données $Z \rightarrow e^+e^-$ est décrite dans le chậpitre 4.

Le faisceau d'essais combinés réalisé entre le printemps et l'automne 2004 a été particulièrement important, car une section de tous les sous-détecteurs ATLAS utilisant le système électronique final ou quasi-final de lecture a été assemblée pour la première fois avec le système de déclenchement et d'acquisition de données (TDAQ). Le chậpitre 5 étudie la séparation e/π dans le système de déclenchement LVL2 en utilisant des électrons et des pions provenant du faisceau d'essais avec des impulsions de 20 et de 50 gev/c. Les résultats de cette analyse sont importants, puisque c'est la première et unique fois où une tranche complète d'ATLAS a pu être assemblée et étudiée avant que le détecteur ne devienne totalement opérationnel.

1.1 L'expérience ATLAS au LHC

ATLAS (A Toroidal LHC ApparatuS) est l'un des deux détecteurs généralistes qui seront construits auprès du LHC, le futur collisionneur proton-proton du CERN. Le LHC produira des faisceaux de protons de 7 TeV, donnant ainsi accès à des collisions d'une énergie de 14 TeV dans le centre de masse. Il est destiné à fonctionner à terme à une luminosité de $(10^{34}\,\mathrm{cm}^{-2}\mathrm{s}^{-1})$. Les croisements des faisceaux de protons s'effectueront toues les 25 ns, et à haute luminosité il y aura près de 24 collisions proton-proton par croisement. Le détecteur Atlas est situé au point 1, en face de l'entréé du CERN. Le détecteur est composé de quatre sous détecteurs principaux, le trajectographe interne qui mesure les trajectoires et les impulsions des particules chargées, les calorimètre qui mesurent l'énergie transportée par les particules, le spectromètre à muons qui identifie et mesure les muons et le système d'aimants qui courbe les trajectoires des particules chargées pour permettre la mesure de leur impulsion. Le détecteur a la forme d'un cylindre d'une longueur totale de 42 m, un rayon de 11 m et un poids d'environ 7000 tonnes.

Le détecteur a été optimisé à l'aide de l'étude détaillée d'un grand nombre de signatures de physique. Le détecteur se caractérise de la façon suivante :

- reconstruction efficace des traces chargées à haute luminosité pour la mesure des leptons, l'étiquetage des quarks-b, et l'aide à l'identification des électrons et des gammas. à basse luminosité, reconstruction de vertex secondaires provenant de tau et de quarks lourds pour l'étude de certains états finals de B.

- calorimétrie électromagnétique de grande précision pour l'identification et la mesure des électrons et des gammas, complétée par la mesure des jets et de

l'énergie manquante à l'aide de calorimètres hadroniques.

- mesure précise et autonome des muons de toute la gamme d'énergie accessible à haute luminosité.

Le domaine de physique est optimisé par l'obtention d'une grande acceptance en eta, et par la capacité de déclenchement (trigger) sur des particules de petit p_T.

Le détecteur interne permettra de reconstruire les traces des particules chargées d'impulsion transverse p_T supérieure á $0,5\,\mathrm{GeV/c}$ dans la région de pseudorapidité en [-2,5; 2,5], d'étiqueter les jets issus de quarks b et de reconstruire les vertex des désintégrations secondaires. Pour parvenir á ces résultats, ce détecteur est scindé en deux parties : les détecteurs les plus internes (pixels, SCT) utilisent la technologie des semiconducteurs et fournissent un nombre limité de points de mesure d'une très grande précision. Le trajectographe (TRT) donne un suivi des traces quasi-continu grâce á un grand nombre de points de mesure. L'ensemble du détecteur interne est entouré d'un solénoide supraconducteur qui délivre un champ de 2 Tesla. La quantité de matière de cet aimant a été minimisée pour éviter que les gerbes électromagnétiques ne soient initiées dans le détecteur interne, ce qui dégraderait les mesures de l'énergie des électrons et des photons.

Le calorimètre á argon liquide est divisé en plusieurs composantes: un calorimètre électromagnétique á échantillonnage en plomb avec une géométrie en accordéon dans les parties tonneau et bouchons, un calorimètre hadronique utilisant des électrodes en cuivre plates dans les bouchons, et le calorimètre en avant près du tube du faisceau, dans la partie bouchons, fait de cuivre et de tungstène. De plus, les pré-échantillonneurs sont constitués d'une couche d'argon liquide en amont du calorimètre électromagnétique pour aider á corriger les pertes d'énergie en amont du calorimètre (dues essentiellement aux parois du cryostat et du solénoide tonneau).

Entourant le calorimètre èlectromagnétique, on trouve Calorimètre à Tuiles. Ce calorimètre utilise comme absorbeur des plaques de fer et comme millieu actif des tuiles à scintillation, placées radialement, d'une épaisseur de 3 mm, dont le signal de chaque face est lu par des photomultiplicateurs (PM) via des fibres optiques. Le calorimètre est constitué d'un Tonnneau central et de deux Tonneaux de chaque coté, l'ensemble, composé de trois couches en profondeur et d'un rayon externe de $4,25\,\mathrm{m}$, couvrant la zone $|\eta| < 4.9$.

Dans la partie tonneau ($|\eta| < 1$), qui est couverte par le grand système toroidal, les muons sont mesurés par trois couches de chambres, autour de l'axe du faisceau, utilisant des tubes á dérives de précision - Monitored Drift Tubes (MDTs) - et des chambres á plaques résistives - Resistive Plate Chambers (RPCs). Dans les région de grande pseudo-rapidité, trois couches de chambres sont aussi installées, mais verticalement. Là, des chambres á intervalles fins - Thin Gap Chambers (TGCs) - sont utilisées pour le sytème de déclenchement. Les mesures de précision sur les muons sont effectuées par les MDTs, á l'exception de la roue la plus interne des bouchons et pour $|\eta| > 2$. Dans la partie tonneau, les chambres á muons sont

installées dans trois cylindres concentriques par rapport á l'axe du faisceau á des rayons de 5, 7,5 et 10 m. Elles sont agenciées pour former des tours projectives vers le vertex d'interaction nominal. Dans les bouchons, la distance suivant z au vertex est d'environ 7, 120 et 14 m pour chacune des couches.

1.2 Le système de déclenchement d'ATLAS

Au sein du détecteur ATLAS les événements seront générés à une fréquence de 40 MHz. Si onse base sur les sections efficaces de production et de désintégration des particules et les connaissances des caractéristiques du détecteur, on peut estimer que chaque événement correspondra à environ 2 Mo de données générées, cequi signifie que le flux de données au sein du détecteur sera de l'ordre de 8.1013 octets/s (80 To/s).

Cet objectif de passer de 80 To/s a 200 Mo/s sera réalis é à travers l'utilisation de trois modules différents nommés niveau1 (LVL1) , niveau2 (LVL2) et filtre dévénements (Event Filter).

La solution envisagée est basée sur ldée que la physique que l'on va chercher à mettre en évidence dans ATLAS sera noyée au milieu d'une physique bien connue. Un événement comportant un boson de Higgs, par exemple, ne représentera quun événement sur plusieurs millions, les autres événements ne reflétant qu'une physique déjà connue ou représentative dun bruit de fond(collisions sur des molécules résiduelles dans l'accélérateur). L'idée consiste alors à rejeter le maximum d'événements qui nesont pas susceptibles de porter une nouvelle physique. On va chercher dans cette méthode à enrichir notre lot d'événements en événements intéressants. Dans cette approche, la taille des événements reste la même, c'est le taux de ces événements qui diminue au fur et à mesure qu'ils passent dans les filtres.

Le schéma ci-dessous (Fig.1.1) montre les trois niveaux de sélection du détecteur ATLAS et leur placement dans la chaîne d'acquisition .

- Level 1

  Le premier niveau de trigger ou LVL1 est un niveau de sélection purement électronique. La tche principale du système LVL1 est de procéder à un rejet préliminaire du bruit de fond, afin de réduire le taux initial de 40 MHz à moins de 2.2 νs. Il utilise des données du calorimètre (granularité grossière) et des systèmes de détecteur de muons, mais pas des chambres de trajectoires des détecteurs internes. Les critères qui vont amener à cette prise de décision sont de plusieurs ordres. Ils correspondent pour les calorimètres, au dépassement dun seuil, à des dépts d'énergie dans certains secteurs des calorimètres. Dans le cas des chambres à muons, le critère va porter essentiellement sur la présence d'une ou plusieurs particules ayant un moment transverse supérieur à un certain seuil. Le trigger de premier niveau va ainsi créer une information de première importance pour les trigger ssuivants. Il va définir les secteurs du
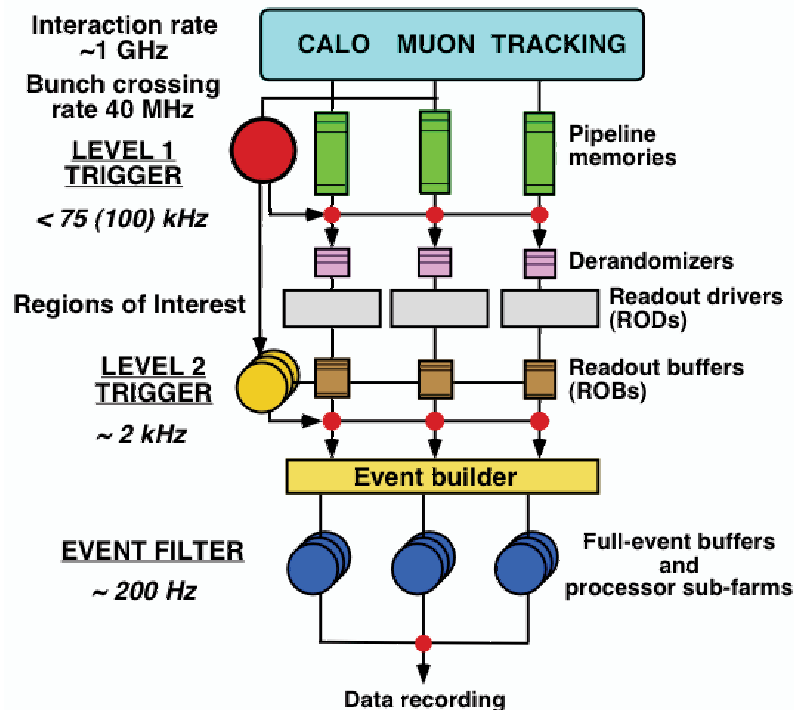
Figure 1.1: *Architecture globale du système de déclenchement et d'acquisition de données (TDAQ).*

détecteur où se concentre l'information utile, c'est ce quel'on appelle lesROI (Regions Of Interest). La localisation des ROI et leur contenu en termes d'information physique(comme la présence de jets, le franchissement d'un seuil enénergie,etc) vont être transmises au niveau deux, pour lui permettre de connaître immédiatement quelles sont les zones du détecteur intéressantes à analyser, supprimant ainsi le besoin de parcourir l'ensemble du détecteur.

- Level 2
  Le deuxième niveau de trigger doit, lui, diminuer d'unfacteur 50 à 100 le taux de données. Le LVL2 doit donc faire passer le flux de données à un taux de1à 2kHz en sa sortie et cela dans un temps maximum del'ordre de 10 ms. Ici on dispose de plus de temps, car n'oublions pas que, à ce niveau là nous avons 100 kHz de données entrantes, ce qui laisse un peu plus de temps pour faire la sélection que n'en avait le trigger de niveau un.

  Le processeur central du système va déclencher le trigger de niveau deux et lui passer l'information concernant les ROI, permettant ainsi au trigger de connaître les zones du détecteur intéressantes.

  Le temps, de l'ordre de quelques millisecondes, imparti à ce trigger lui permet de faire une sélectionsur des critères plus complets que cequ'a fait le niveau précèdent. Le niveau un n'a fait sa sélection que sur des seuils enénergie dans les calorimètres et sur une identification grossière des muons. Les critères de

May 26, 2006

sélection du niveau deux seront plus complets, plus précis et ils porteront sur des arguments liés à la physique de l'événement.

- Event Filter
  Les sélections qui seront effectuées au niveau du filtre d'événements auront pour objectif de ne laisser passer que 100 à 200 événements par seconde sur les 1000 à 2000 qui sont acceptés par le niveau deux. Le temps estimé pour la sélection d'un événement est del'ordre de la seconde. On s'attend à des temps de traitement qui seront de l'ordre de 0,1 seconde, pour les événements rapidement rejetés, à plus de1 seconde pour les événements qui réclament une analyse plus complète. Le taux de 200 événements par seconde retenu en sortie de chaîne d'acquisition, provient des estimations qui ont été faites sur la statistique nécessaire pour faire ressortir un signal de découverte, mais aussi des estimations des ressources disponibles qui permettront d'analyser les données. Par rapport aux deux niveaux précédents l'Event Filter présente la particularité d'effectuer sa sélection sur un événement entier. C'est le seul niveau de trigger où l'on dispose de l'ensemble de l'information concernant un événement. Les critères de sélection vont ainsi pouvoir être appliqués sur l'événement dans sa globalité et non plus uniquement sur des fragments.

1.3 Identification des electrons a haute p_T par le systeme HLT d'ATLAS

L'identification des électrons isolés de haute impulsion transverse ($p_T \geq 25\,GeV$) par le système HLT d'ATLAS est essentiel pour des études de physique au LHC. En effet, le déclenchement doit pouvoir choisir des électrons d'une façon très efficace, tout en gardant le taux de bruit de fond à un minimum. Les exemples typiques sont les recherches sur la désintégration du boson de Higgs en quatre électrons $H \to ZZ^{(*)} \to 4e$, avec une coupe transverse de $0.2\,fb$ pour une masse de Higgs de $130\,GeV/c^2$, la production de Z avec désintégrations $Z \to e^+e^-$ ($\sigma = 1,5 \times 10^{-6}\,mb$), ou la production de W avec désintégrations $W \to e\nu$ ($\sigma = 1,5 \times 10^{-5}\,mb$). La coupe du di-jet QCD, étant de l'ordre de $1\,mb$, pour obtenir un signal inclusif d'électron, un facteur 10^7 de rejet est exigé sur des di-jets QCD.

Ce chapitre présente une étude Monte Carlo sur la performance du système de déclenchement HLT d'électrons isolés de haute impulsion transverse et de ses possibilités de rejet contre les di-jets QCD, en utilisant le calorimètre électromagnétique et hadronique aussi bien que les systèmes de détecteur central des traces. Les données utilisées ont été produits à basse ($2 \times 10^{33}\,cm^{-2}\,s^{-1}$) et haute luminosité ($10^{34}\,cm^{-2}\,s^{-1}$), et sont composés des electrons simple ($p_T \geq 25\,GeV$, $p_T \geq 30\,GeV$) et di-jets QCD ($p_T \geq 17\,GeV$, $p_T \geq 17\,GeV$).

Le tableau 4.9 indique les efficacités obtenues, ainsi que le taux d'événement lorsqu'on applique successivement les coupures mentionées dans les paragraphes

	Basse Luminosité		Haute Luminosité	
Niveau Trigger	**Efficacité(%)**	**Taux (Hz)**	**Efficacité (%)**	**Taux (Hz)**
LVL2 Calo	95.9 ± 0.3	2114 ± 48	97.4 ± 0.3	3408 ± 62
LVL2 Tracking	88.0 ± 0.5	529 ± 24	92.0 ± 0.3	780 ± 30
LVL2 Matching	86.6 ± 0.6	137 ± 12	90.6 ± 0.4	420 ± 16
EF Calo	84.4 ± 0.6	56 ± 8	90.5 ± 0.5	340 ± 15
EF Tracking	82.4 ± 0.6	46 ± 8	84.8 ± 0.6	279 ± 13
EF Matching	79.0 ± 0.7	30 ± 5	78.2 ± 0.6	176 ± 11

Table 1.1: *Performance of the single electron HLT trigger at low (design luminosity). The results are presented in a single sequence. The efficiencies are given for single electrons of $p_T = 25\,GeV$ ($30\,GeV$) over the full rapidity range $|\eta| < 2.5$, and excluding the barrel/end-cap overlap region. The efficiencies and rates are given with respect to a LVL1 output efficiency of 95% and a LVL1 rate for EM clusters of $12kHz$ ($16kHz$). Some problems in the LVL2 tracking code as discussed in the text result in a drop in efficiency of around 3% (10%). Events with at least one track found by xKalman (offline equivalent of IDScan), but with zero tracks reconstructed on-line, were not considered for the analysis.*

    précédents. Selon ces résultats, la réduction globale du taux d'évenement réalisé à basse (haute) luminosité par LVL2, est 90(100) pour une perte d'efficacité de 9%(10%) par rapport au LVL1. La réduction additionnelle du taux d'événement fourni par l'EF est d'un facteur 5(4), avec une perte aditionelle d'efficacité de 8%(12%). Ces résultats sont conformes à ceux obtenus dans les études précédentes, et ceux sugéré dans le Rapport du Design Technique (TDR).

1.4 Estimation de l'efficacité du trigger des electron HLT à partir des événements $Z \to e^+ e^-$

Comme l'efficacité de déclenchement des électrons sera un paramètre important dans de nombreuses analyses de physique, il est important d'avoir plusieurs méthodes d'évaluation indépendantes les unes des autres, dépendant le moins possible de la description Monte Carlo du détecteur et de ses conditions d'utilisation, puisque cette méthode est forcément incomplète. Une méthode pour déterminer l'efficacité du trigger HLT des électrons a été ainsi développée employant des événements $Z \to e^+ e^-$. La méthode propose la selection des événements $Z \to e^+ e^-$ en utilisant un declenchement d'electron simple, et de étiqueté tout les événements pour lesquelles un deuxième électron aurait été déclenché par le trigger. Après la reconstruction des événements, on choisit un échantillon dans lequel une paire $e^+ e^-$ est identifiée. L'histogramme de la masse invariante est alors centrée près de la masse du Z en utilisant une distribution gaussienne plus une fonction linéaire. A partir du résultat du fit, le nombre d'événements identifiés contenant des $Z \to e^+ e^-$, N_1^z, est déterminé

avec le nombre d'événements de bruit du fond dans la région du fit, B_1. Le même processus est suivi en utilisant un double déclenchement d'électron avec la même efficacité. Ceci a comme conséquence le nombre d'événements de signal et de bruit de fond N_2^z et B_2. Le nombre d'événements $Z \to e^+e^-$ obtenues avec les déclenchements simples et doubles est alors:

$$N_1^Z = \epsilon_{rec}(2\epsilon_{trig} - \epsilon_{trig}^2)N_0^Z + B_1 \tag{1.1}$$

et

$$N_2^Z = \epsilon_{rec}\epsilon_{trig}^2 N_0^Z + B_2 \tag{1.2}$$

Dans le cas où N_0^z est la quantité initiale des $Z \to e^+e^-$ dans notre échantillon, ϵ_{rec} est l'efficacité de reconstruction du Z, y compris l'acceptation de détecteur, et ϵ est l'efficacité. A partir des équations 1.1 et 1.2, l'efficacité de déclenchement d'un electron peut être obtenue par :

$$\epsilon_{trig} = \frac{2(N_2^Z - B_2)}{(N_1^Z + N_2^Z) - (B_1 + B_2)} \tag{1.3}$$

On s'attend à ce que la contamination du bruit de fond soit très petite dans la région sous le pic de la masse invariante. Néanmois cette contamination peut contribuer à l'erreur systématique de la mesure. Pour évaluer cet effet, des histogrammes de masse invariante, obtenus à partir des événements QCD, ont été ajoutés à notre signal de façon a qu'ils réprésentent 5%, 20% ou 60% du nombre d'entrées dans la fenêtre de masse du Z (Fig.5.11). Il en résulte que la limite supérieure de la contribution systématique d'erreur s'est avérée $\sim 1.0\%$, et donc on ne le prévoit pas qu'il contribue sensiblement à l'incertitude globale. La même efficacité a été trouvée, indépendamment de la fraction du bruit de fond ajoutée. Cette méthode a été examinée avec des événements $Z \to e^+e^-$, et une efficacité de 87.0% a été trouvée pour l'ensemble des coupures utilisées dans la sélection d'electrons. La même valeur a été obtenue en utilisant l'information Monte Carlo des événements simulés choisis par cette signature. Assumant une luminosité instantanée de $10^{33}\,\mathrm{cm}^{-2}\mathrm{s}^{-1}$, pour $Z \to e^+e^-$ une coupe transverse de $1.515\,\mathrm{nb}$, ceci mène à une incertitude statistique estimée pour l'efficacité globale de $\sim 3\%$ après 1 heure d'acquisition.
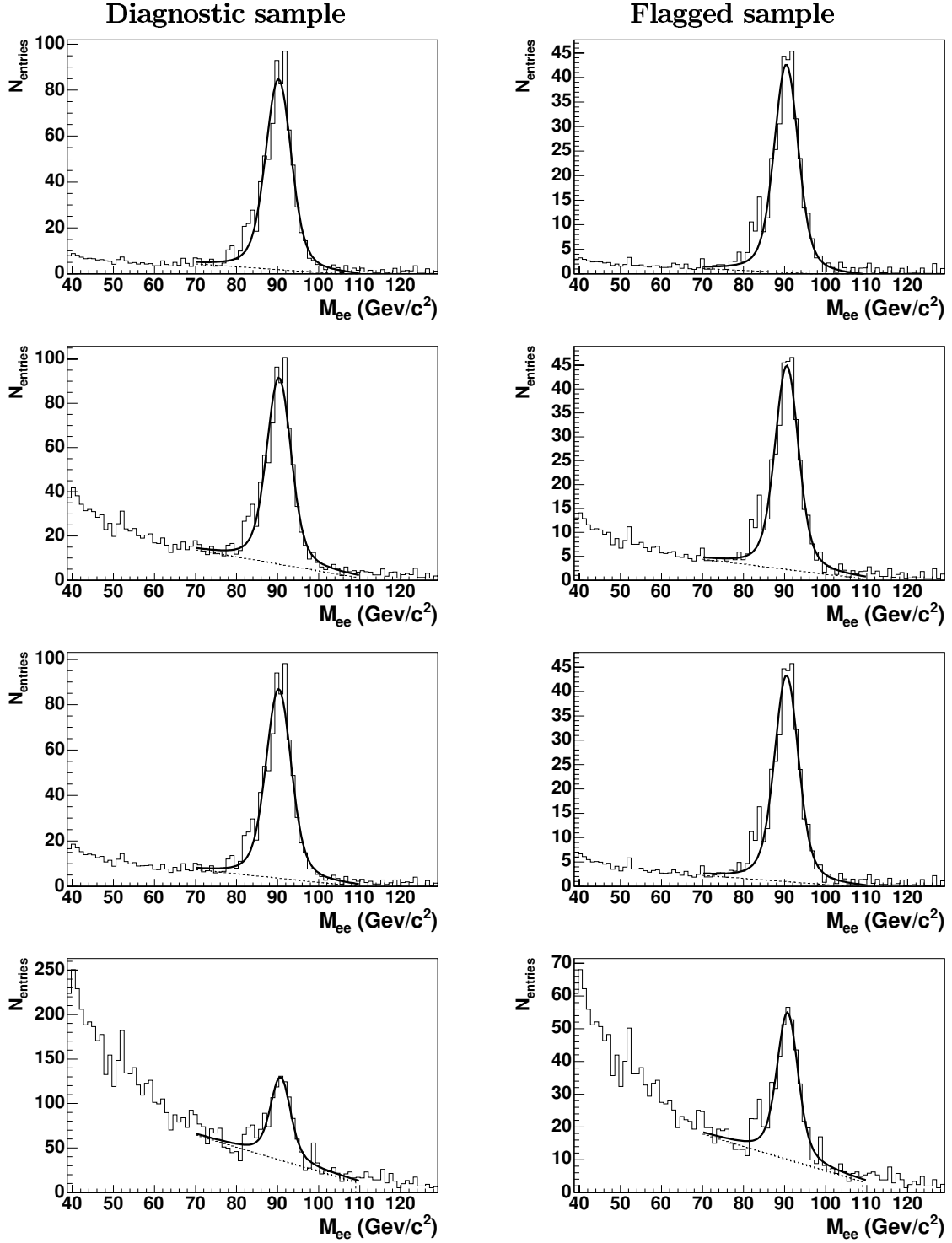
Figure 1.2: *Invariant mass distribution of the diagnostic (left column), and flagged (right column) sample under different background levels scenarios. Des événements QCD, ont été ajoutés à notre signal de façon a qu'ils contribuent: 5% (4%), 10% (9%), 20% (19%), et 60% (59%) du nombre d'entrés dans la fenêtre de masse du Z.*

Figure 1.3: Schematic view of the experimental setup in the CERN H8 area.

1.5 Performance du système de déclenchement HLT dans le faisceau d'essais combinés 2004

Les faisceaux d'essais combinés sont de grande importance pendant la période de recherche et de développement d'un détecteur, puisqu'ils représentent une grande occasion de faire face et résoudre des problèmes inattendus, qui pourraient surgir à une étape postérieure, une fois que le détecteur est opérationnel. Le faisceau d'essais combinés effectué entre le printemps et l'automne 2004 a été particulièrement important, car une tranche d'ATLAS (détecteur de traces dans un champ magnétique, calorimètres électromagnétique et hadronique, chambres à muons) utilisant le système électronique final ou quasi-final de lecture a été assemblée pour la première fois avec le système de déclenchement et d'acquisition de données (TDAQ). Un schéma de l'installation est présenté sur la Fig. 6.1.

La séparation e/π par le système LVL2 d'ATLAS a été étudiée dans ce contexte lors de l'exposition aux électrons et aux pions entre 20 et 50 gev/c. Des échantillons propres d'électrons et de pions ont été initialement choisis. Pour ce choix, les détecteurs de faisceau (Muon veto et Chrenkov), ainsi que le détecteur de TRT ont été employés pour obtenir des échantillons . En exigeant une trace reconstruite dans le TRT avec au moins 7 hits de transition de radiation, un échantillon très pur d'électrons est choisi. Des Pions ont été choisis en tant que traces reconstruites de TRT avec au maximum 2 hits de transition de radiation.

20 *GeV* nominal electron beam

20 *GeV* nominal pion beam

50 *GeV* nominal electron beam

50 *GeV* nominal pion beam
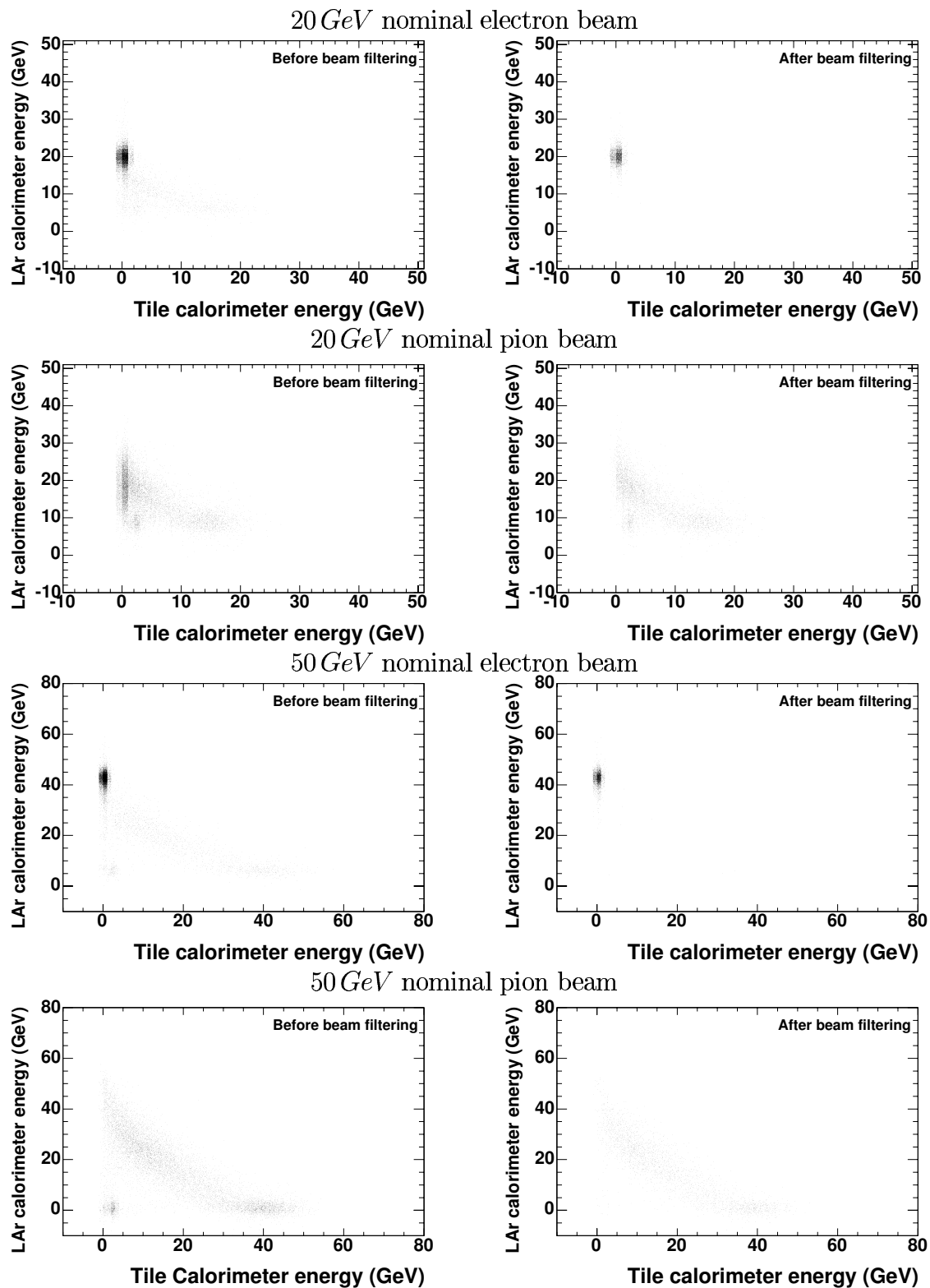
Figure 1.4: Correlation plots of the signal in the LAr EM calorimeter and the Tile hadronic calorimeter for nominal beams of 20 and 50 GeV electrons and pions. The plots are shown before (left column) and after (right column) beam filtering.

La figure 6.9 compare le dépôt d'énergie dans les calorimètres argon liquide avant et aprés le filtrage du faisceau pour entre électrons et mésons pi de 20 et 50 gev/c. Comme on peut observer, la contamination résultante de chaque échantillon est très petite et ils peuvent être considérées comme100% purs dans l'analyse suivante de l'efficacité du sytème HLT. Les critères d'identification d'électron par le niveau 2 employant le calorimètre électromagnétique incluent le rapport de l'énergie déposé dans la deuxième couche entre une fenetre de 3x7 cellules et d'une fenêtre des 7x7 cellules, de toute l'énergie transversale (E_T), de 2 variables de forme de la gerbe (R_η^{strips}, et R_η^{core}), et de toute l'énergie transversale hadronique (E_T^H). Les Pixel et les SCT ont été également employés pour choisir des électrons. Les variables distinctives avec une trace reconstruite dans les Pixel et le SCT incluent l'impulsion de la trace p_t, le rapport entre l'énergie transversale dans le calorimètre et le p_T de la trace, et la distance ($\Delta\eta, \Delta\varphi$) entre la trace et le cluster. Après un réglage des coupures, une efficacité de $\sim 90\%$ est obtenue pour les électrons, avec une contamination négligeable des pions. Les distributions E_t et E_t^h des pions (ligne pointillée rouge) et des électrons (ligne solide noire) ainsi que l'efficacité du trigger des électrons selon la valeur de la coupure sont montrées dans la figue 6.10-6.14.

Cette étude montre qu'en utilisant le calorimètre et le détecteur interne (SCT et Pixel), on peut atteindre une efficacité du trigger de niveau 2 pour les électron de $\sim 90\%$, tout en gardent le taux des pions à un niveau de 7 par mille.
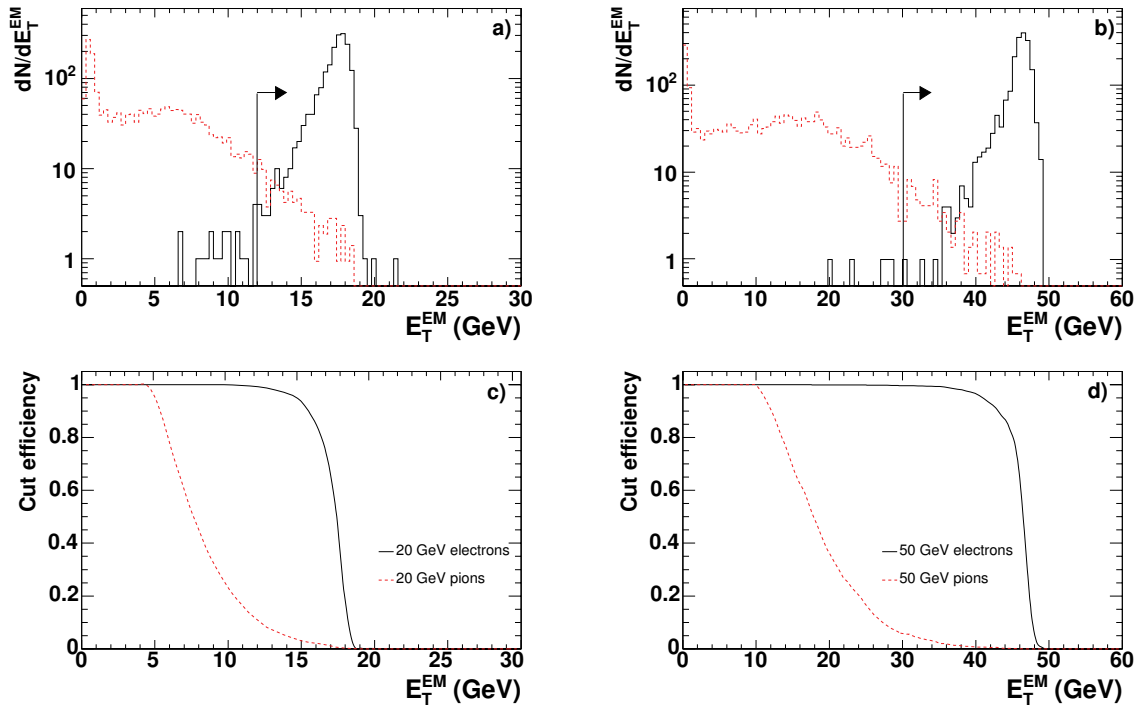
Figure 1.5: Transverse energy deposited in the second sampling of the EM calorimeter. Distributions are shown for 20 GeV, a), and 50 GeV, b), particles. The continuous line corresponds to electrons and the dotted one to pions. The arrow shows the selected events. Figures c) and d) show the efficiency of selecting the corresponding particles as a function of the cut in the E_T^{EM} variable, for 20 GeV and 50 GeV, respectively.
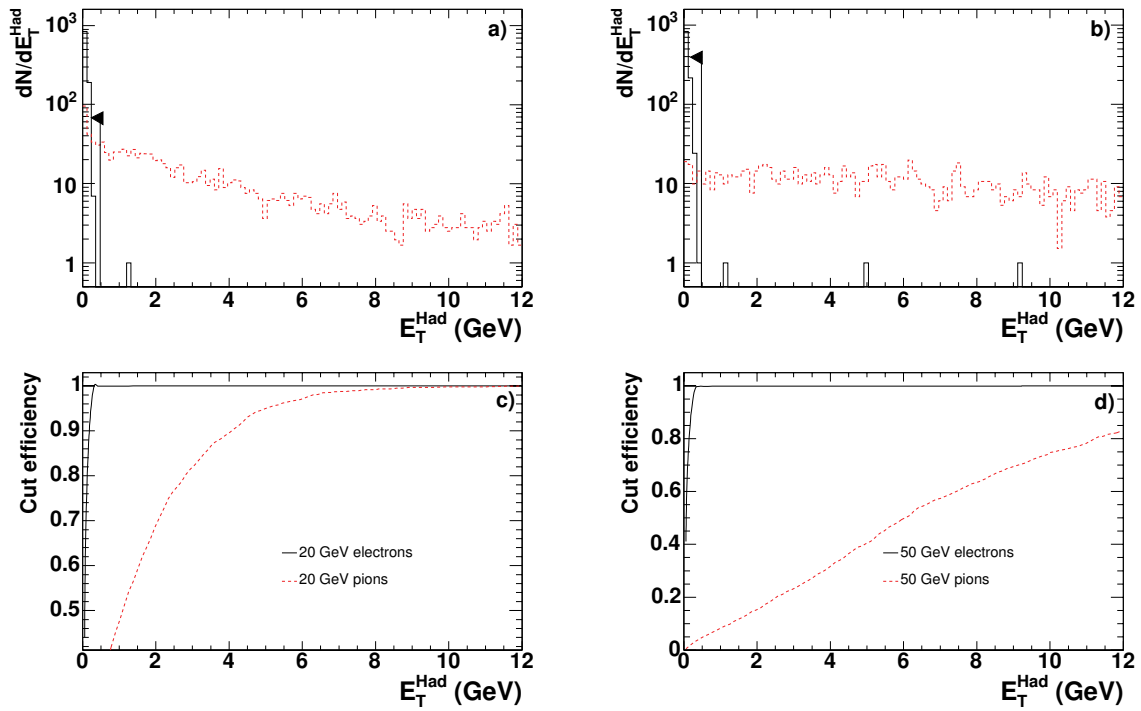
Figure 1.6: Transverse energy deposited in the first sampling of the hadronic calorimeter. Distributions are shown for 20 GeV, a), and 50 GeV, b), particles. The continuous line corresponds to electrons and the dotted one to pions. The arrow shows the selected events. Figures c) and d) show the efficiency of selecting the corresponding particles as a function of the cut in the E_T^{Had} variable, for 20 and 50 GeV respectively.
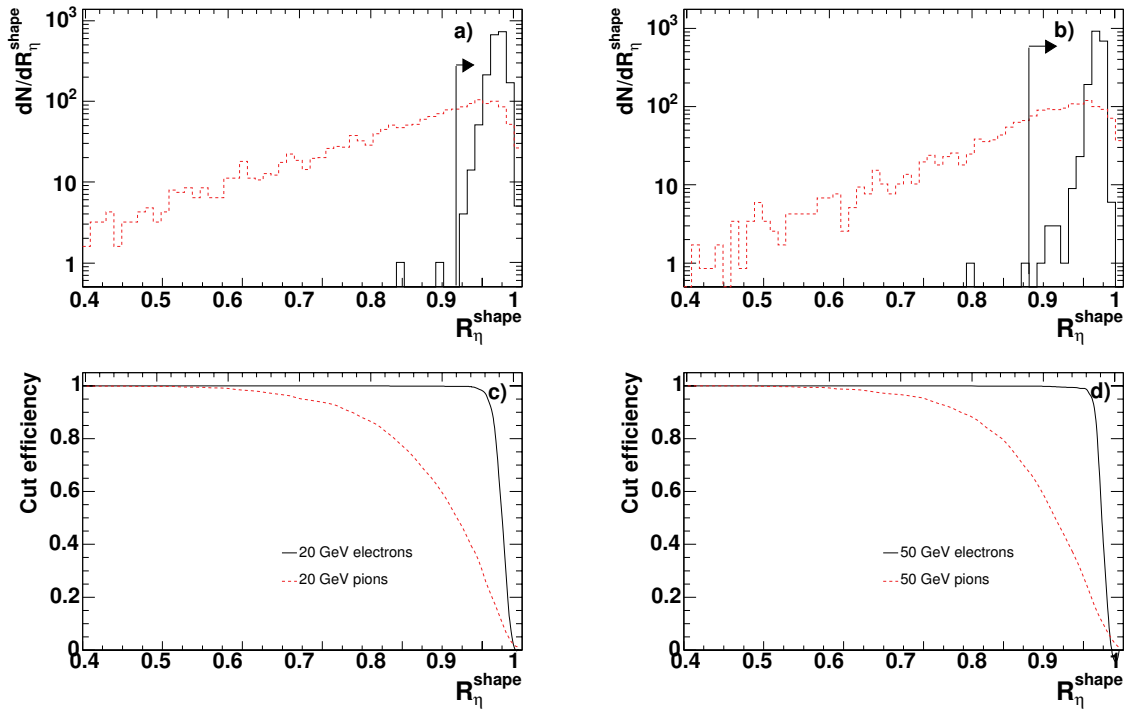
Figure 1.7: Lateral shape in the second sampling of the EM calorimeter. Distributions are shown for 20 GeV, a), and 50 GeV, b), particles. The continuous line corresponds to electrons and the dotted one to pions. The arrow shows the selected events. Figures c) and d) show the efficiency of selecting the corresponding particles as a function of the cut in the R_η^{shape} variable, for 20 and 50 GeV respectively.
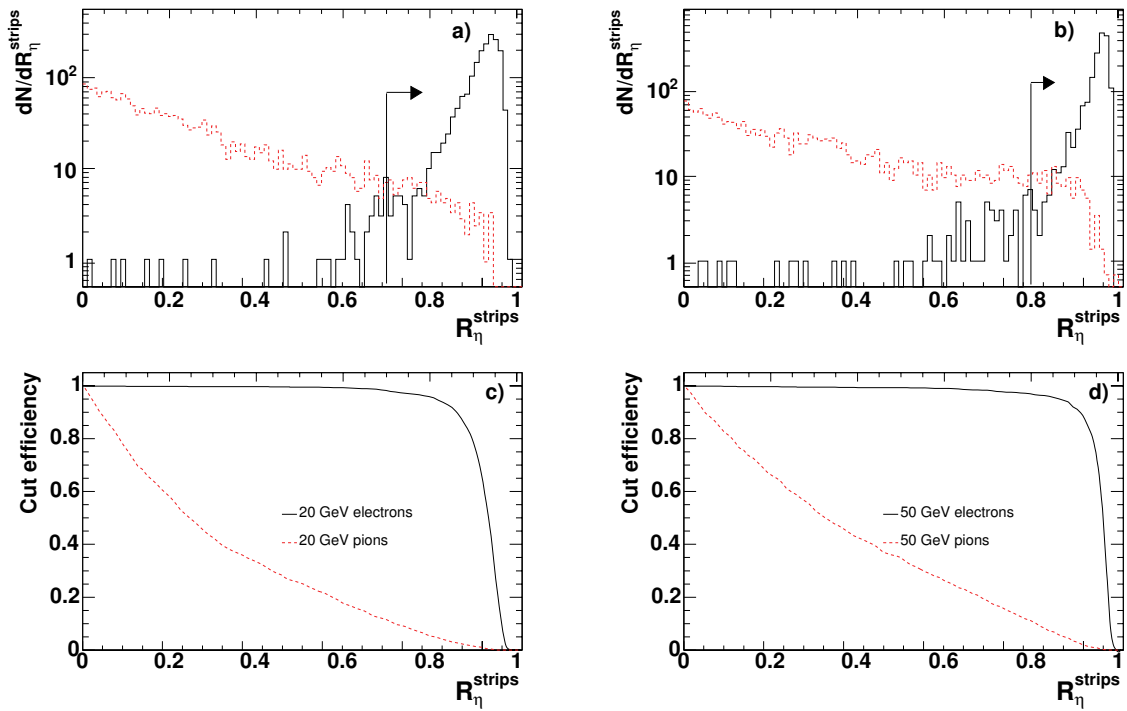
Figure 1.8: Lateral shape in the first sampling of the EM calorimeter. Distributions are shown for 20 GeV, a), and 50 GeV, b) particles. The continuous line corresponds to electrons and the dotted one to pions. The arrow shows the selected events. Figures c) and d) show the efficiency of selecting the corresponding particles as a function of the cut in the R_η^{strips} variable, for 20 and 50 GeV respectively.
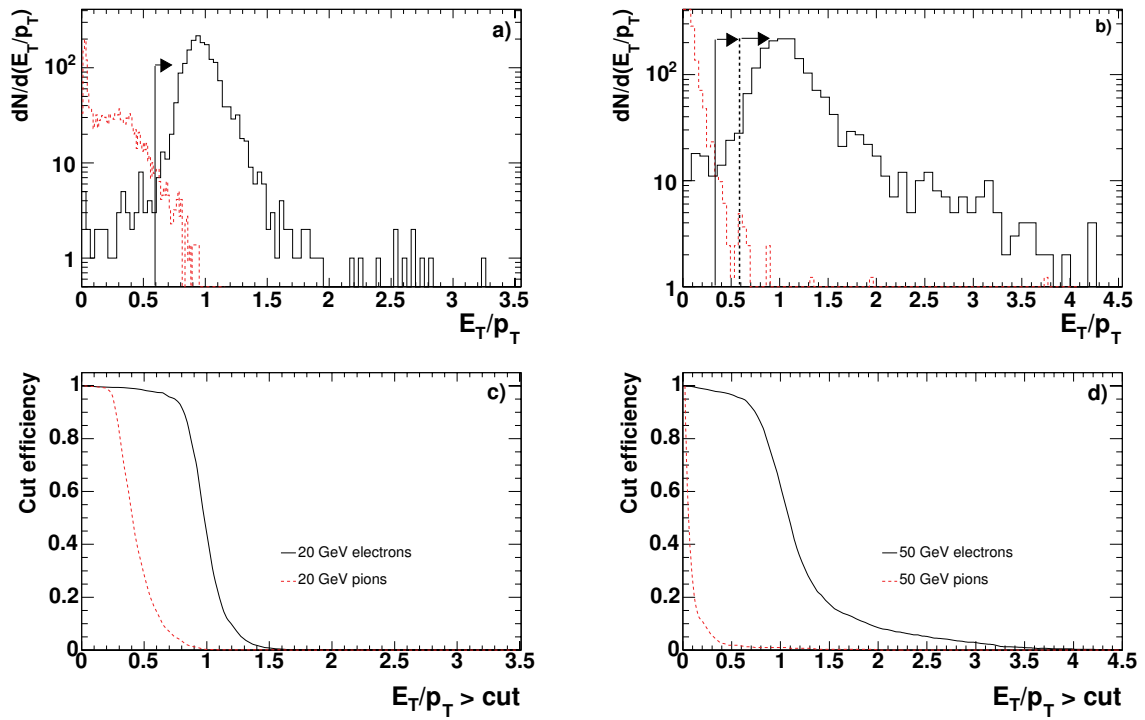
Figure 1.9: Ratio between the cluster energy and the momentum of the reconstructed track Distributions are shown for 20 GeV, a), and 50 GeV, b), particles. The continuous line corresponds to electrons and the dotted one to pions. The arrow shows the selected events. Figures c) and d) show the efficiency of selecting the corresponding particles as a function of the cut in the E_T/p_T variable, for 20 and 50 GeV respectively.

Chapter 2

The ATLAS Detector at the LHC

2.1 The Large Hadron Collider

The Large Hadron Collider (LHC) is presently under construction, and will start operation in 2007. It will be installed at CERN (European Centre for the Nuclear Research, Geneva, Switzerland) in the existing 27 km tunnel formerly used for LEP (see fig 2.1 for a schema of the CERN accelerator layout). LHC will provide 14 TeV centre-of-mass energy proton-proton (p-p) collisions, at a luminosity up to $10^{34}\,\mathrm{cm^{-2}s^{-1}}$ with a bunch crossing frequency of 40 MHz. LHC will be also capable to produce heavy ion (e.g. Pb-Pb) collisions.

Four large-scale experiments will operate at LHC: ATLAS and CMS, which are general purpose experiments with a wide physics program, LHCb, which will be devoted to the physics of B-hadrons and to the study of CP violation, and ALICE, which is a dedicated heavy-ions experiment that will study the behaviour of the nuclear matter at very high energies and densities.

The LHC physics program is broad and ambitious. The physics motivations that support the building of such an unprecedented collider machine can be briefly summarized as follows:

- Search for the Standard Model (SM) Higgs boson [1] that is predicted to be responsible for the origin of the particle masses through the mechanism of spontaneous breaking of the electro-weak symmetry.

- Look for the physics beyond the Standard Model, a model that for several reasons cannot be expected to be the ultimate theory of particle interactions [2].

- Perform precision measurements of the properties of the known particles, in order to refine the present values, and to search signals of new physics in unexpected deviations from the SM predictions [3].
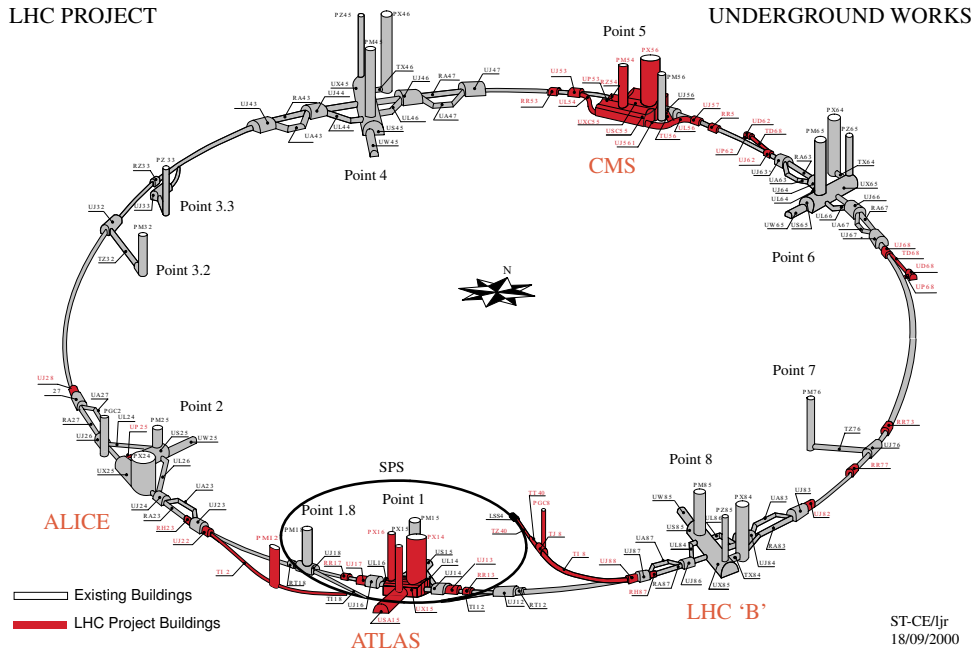
Figure 2.1: Layout of CERN LEP tunnel, including the future LHC infrastructures.

LHC parameter	Nominal value
beam energy	$7\,\mathrm{TeV}$
beam energy at injection	$450\,\mathrm{GeV}$
nominal luminosity	$10^{34}\,\mathrm{cm}^{-2}\mathrm{s}^{-1}$
luminosity life time	$10\,\mathrm{hours}$
beam life time	$22\,\mathrm{hours}$
number of bunches	2835
proton (p) per brunch	10^{11}
bunch spacing	$25\,\mathrm{ns}$
p current density	$0.54\,\mathrm{A}$
beam total energy	$334\,\mathrm{MJ}$
energy loss per tour	$6.7\,\mathrm{KeV}$

Table 2.1: Summary of the main LHC parameters

2.1.1   Proton-proton collisions characteristics

Two operational phases are foreseen for the LHC: during the first years the accelerator will provide an instantaneous luminosity of $L \simeq 10^{33}\,\mathrm{cm}^{-2}\mathrm{s}^{-1}$ ("low" luminosity phase). The nominal peak luminosity $L \simeq 10^{34}\,\mathrm{cm}^{-2}\mathrm{s}^{-1}$ is expected to be reached at a later stage ("high" luminosity phase). The nominal pp luminosity and center-of-mass energy will allow searches for new particles up to masses of $\sim 5\,\mathrm{TeV}$. Details

on the LHC machine parameters can be found in Table 2.1 [4].

In one year (1 "year" run time $\simeq 10^7$ s) of running at high luminosity LHC will provide an integrated luminosity of:

$$L = \int_{10^7 s} L dt \simeq 100 \, fb^{-1} \tag{2.1}$$

The total inelastic pp cross-section at $\sqrt{s} = 14$ TeV is $\sigma_{pp}^{tot} \sim 80$ mb. The LHC event rate R at high luminosity is then expected to be:

$$R = \sigma_{pp}^{tot} \times L = 80 \, \text{mb} \times 10^{34} \, \text{cm}^{-2}\text{s}^{-1} \simeq 10^9 \, \text{Hz} \tag{2.2}$$

These events belong to two different classes:

- "minimum bias events": they come from long-range interactions of the incoming protons, in which the momentum transfer is small ("soft" collisions). They represent the majority of the pp collisions, with their effective total cross-section being $\sigma_{m.b.}^{tot} \sim 70 \, mb$. The final state products of these interactions have small transverse momentum relative to the beam line ($< p_T > \simeq 500 \, MeV$), and therefore most of them escape down the beam pipe. On average, 25 minimum bias events will be produced in the same bunch crossing. They will be the main contributors to the pile-up phenomenon, described in section 1.1.2.

- "hard scattering events": they come from short-range interactions of the incoming protons. In these cases the head-on collisions between the partons constituting the protons are characterized by a high momentum transfer. Particles in the final state are produced at high angles with respect to the beam line (high p_T), and massive particles can be created. These are the physics events that will be recorded and studied; they are "rare" with respect to the soft interactions [5] [6] [7].

2.1.2 LHC experimental challenges

The LHC experimental conditions will be highly demanding. The LHC detectors have to face severe conditions imposed by the machine bunch crossing frequency (detector response speed), luminosity (pile-up, radiation level), and to the physics of the p-p collisions (background rejection capability):

- **Pile-up:**The LHC protons are grouped in bunches of $\sim 10^{11}$ particles, colliding at each interaction point every 25 ns. According to the interaction rate at high luminosity (equation 2.2), an average of 25 minimum bias events (soft interactions) will occur simultaneously at each bunch crossing.

These interactions will produce 700 charged particles in the detectors pseudorapidity[1] region $|\eta| < 2.5$. Each time a high p_T event is produced, ~ 25 additional soft events will overlap the interesting one (pile-up).

The Pile-up is one of the most difficult challenges for the LHC detector design. In order to minimize the pile-up impact on the physics event detection, the LHC sub-detectors use different techniques. In general their response must be fast, in order to avoid integration over more that one or two bunch crossings. This implies also a fast readout electronics. In addition, a fine granularity would minimize the probability that the pile-up particles cross the same region of the detector as the interesting object.

For the cases in which the sub-detectors response is larger than $\sim 25 - 50\, ns$, and that is the case of the ATLAS Liquid Argon Electromagnetic Calorimeter (LAr EMC), different techniques of signal shaping and reconstruction have been developed, in order to be able to treat the pile-up events as a kind of noise that superimposes on the interesting physics signal [8] [9].

- **Radiation levels:**The high flux of particles comming from the pp collisions represents an unavoidable source of radiation for the LHC detectors, that for this reason must be radiation resistant. The radiation levels will be different according to the sub-detector position with respect to the interaction point. As an example, in the ATLAS electromagnetic calorimeter , the particle flux integrated over 10 years of operations, will amount up to 10^{17} neutrons/cm^{-2} and up to 10^7 Gy of absorbed energy.

- **QCD background:**The LHC being a hadronic collider, the rate of high p_T events is dominated by QCD jet production, which is a strong process with a large cross section. On the other hand, the most interesting physics processes are rare. Because of this reason, the main LHC physics searches will be conducted looking for channels with a leptonic signature, which usually have small branching ratio (BR) [10] [11]. The detector performance must then be optimized for background rejection while keeping a good sensitivity for the detection of such rare channels.

2.2 The ATLAS experiment

The ATLAS collaboration will build a general purpose pp detector designed to exploit the full discovery potential of the LHC [11], [13], [14]. A mayor focus of interest for ATLAS is the origin of mass at the electro-weak scale. Detector optimization is therefore guided by physics issues such as the sensitivity to the largest possible Higgs mass range. Other important goals are searches for the heavy W and Z-like objects,

---

[1]The pseudorapidity is defined as $\eta = -log(tan(\theta/2))$, where θ is the polar angle referred to beam direction at the detector interaction point

for super-symmetric particles, for compositeness of the fundamental fermions, as well as the investigation of CP violation in B-decays and detailed studies of the top quark. The ability to cope well with a broad variety of possible physics processes is expected to maximize the detector's potential for the discovery of new, unexpected physics.

As the physics potential of ATLAS often needs the largest possible luminosity running at LHC, which implies large background and pile-up events, it is important to select processes with distinguishable, robust signatures that allow for high precision measurements and an efficient background rejection. Processes with e and μ leptons as well as photons in the final state can be identified clearly, and therefore, they are the natural choice in the LHC enviroment. Furthermore, to have hermetic hadronic calorimetry is also vital.

Heavy-quark systems will also be an important chapter of the LHC physics. Therefore, a precise secondary vertex determination, full reconstruction of final states with relatively low mass particles (i.e. small opening angle of its decay products.), low-p_T lepton first level trigger thresholds and track triggering capabilities are all necessary requirements for the experiment.

One can summarize the basic design considerations for ATLAS in the following points:

- very good EM calorimetry for electron and photon identification and measurements, complemented by full-coverage hadronic calorimetry for accurate jet and missing transverse energy measurements;

- high-precision muon measurements, with the capability to guarantee accurate measurements at the highest luminosity using the external muon spectrometer alone;

- efficient tracking at high luminosity for high p_T lepton momentum measurements, electron and photon identification, τ-lepton and heavy flavour identification, and full event reconstruction capability at lower luminosity;

- large acceptance in η and azimuthal coverage;

- triggering and measurements of particles at low p_T thresholds, providing high efficiencies for the physics processes of interest at LHC.

2.3 The ATLAS Detector

The overall ATLAS detector concept, dictated by the requirements listed in the previous section, is not far from the general detector layout of other collider experiments. Going outwards from the interaction point, the first layer one encounters is the inner detector enclosed within a solenoidal magnetic field and followed by the electro-magnetic and hadronic calorimeters. On the outer part of the detector there

is the muon system, equipped with an air-toroid magnet system for stand-alone momentum measurements. It defines the overall dimensions of the ATLAS detector: outer barrel chambers are at a radius of $11\,m$ and the third layer of the forward muon chambers is located $\pm21\,m$ from the interaction point. Figure 2.2 shows a schematic overview of ATLAS.

2.3.1 Inner Detector

The Inner Detector (ID) system is composed of three parts: the sillicon pixel detectors, the sillicon strip detector (SemiConductor Tracker - SCT) and the transition radiation tracker (TRT). It combines the high resolution detectors at inner radii with continuous tracking elements at outer radii. A schematic of the inner tracker can be seen in Fig. 2.3. Each of the above mentioned sub-detectors has a barrel region (up to $|\eta| \leq 1$) where detector layers are arranged on concentric cylinders around the beam axis, while in the forward region (or end-cap), detectors are mounted on disks perpendicular to the beam axis. The full ID extends over $\eta \leq 2.5$, and is enclosed within a super-conducting solenoid of $5.3\,m$ length (to be compared to the ID length of $6.7\,m$) creating a solenoidal magnetic field with a strength of $2\,T$. Since the coil is shorter than the tracking volume the field deviates significantly from uniformity ($B_Z \sim 1\,T$ at the end of the coil and $B_Z \sim 0.4\,T$ at the end of the tracker). This
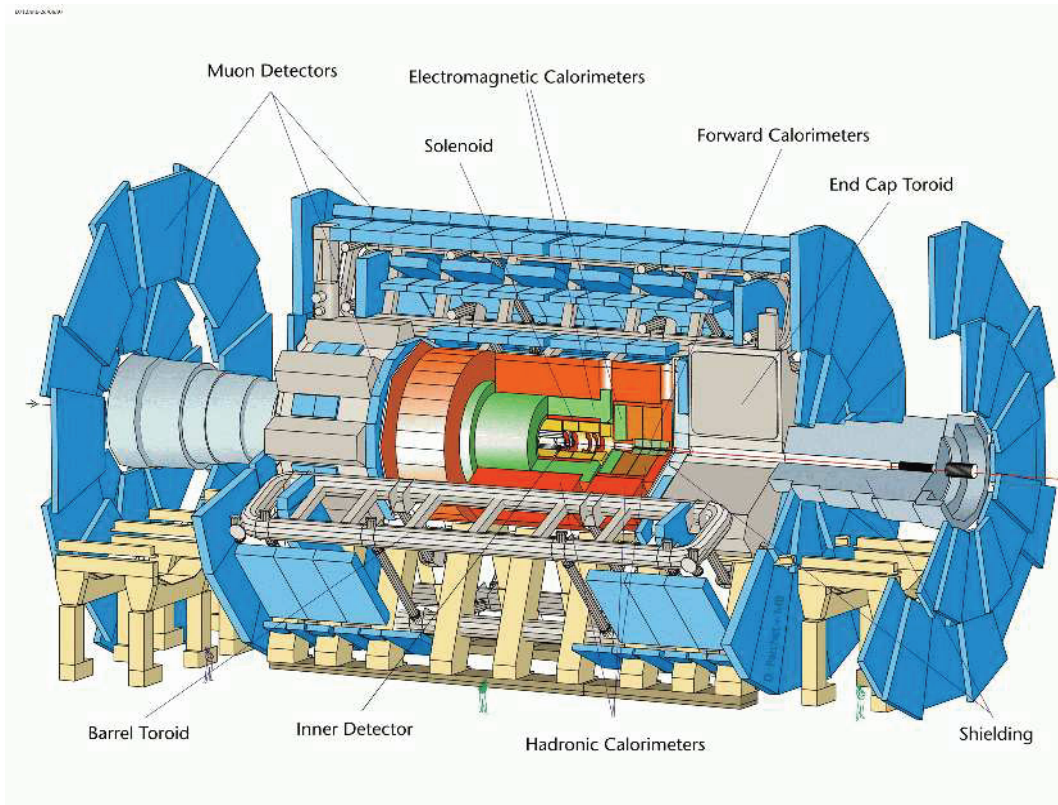
Figure 2.2: General overview of the ATLAS detector.
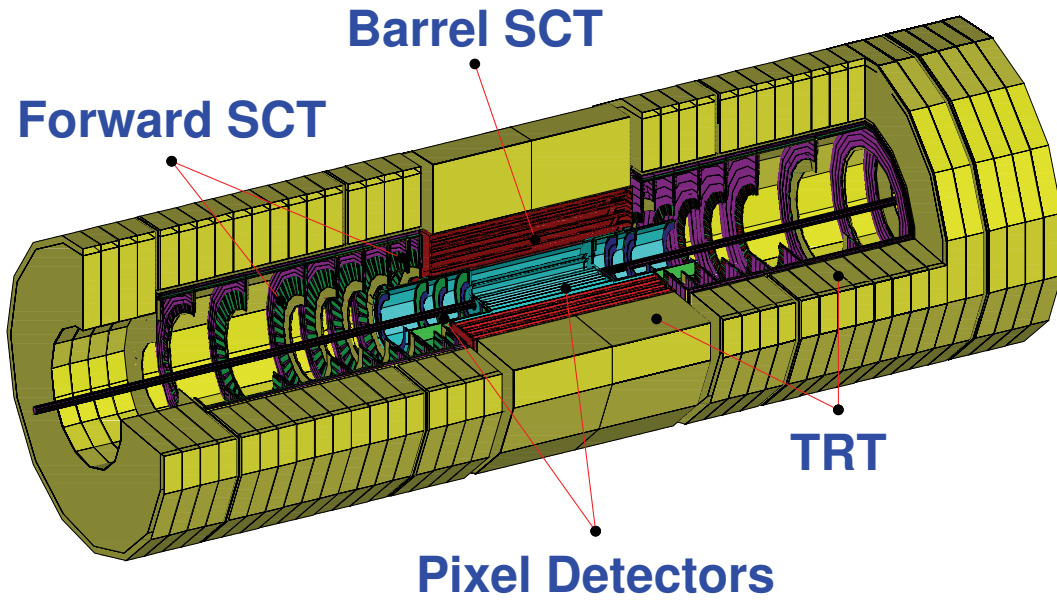
Figure 2.3: ATLAS inner detector system.

poses some technical difficulties for the pattern recognition algorithms. The detailed requirements for the ID can be found in [15].

2.3.1.1   The Pixel Detector

The pixel detector [16] is designed to provide a very high-granularity, high-precision set of measurements as close to the interaction point as possible. There are three pixel barrels (at radii 47.5 mm, 105.5 mm, and 137.5 mm) and four forward disks on each side (with z coordinates of ±490 mm, ±608 mm, ±759 mm, and ±1035 mm), giving at least three measurements of track intersection with a granularity of $\delta R_\phi \times \delta z = 50\,\mu$m $\times$ 400 μm.

Its most important role is to provide the desired vertex resolution and enable one to find secondary vertices to be used for the b and τ identification. For a complete description see [16].

2.3.1.2   The Semiconductor Tracker

The semiconductor tracker (SCT) is designed to provide four precision measurements per track in the intermediate radial range, contributing to the measurement of momentum, impact parameter and vertex position, as well as providing good pattern recognition as a result of the detector's high granularity and low occupancy. The barrel SCT has four layers at radii form 30 cm to 52 cm with an active half-length of 75.5 cm. The layers are composed of modules consisting of two pairs of silicon micro-strip detectors glued back-to-back. Each silicon detector has 768 active readout strips (80 μm pitch) to provide precision points in the R_ϕ plane and z coordinates. The end-cap SCT has nine axial wheels positioned at z coordinates

from $\pm 83.5\,\mathrm{cm}$ to $\pm 277.8\,\mathrm{cm}$. Forward modules are very similar in design but use tapered strips with one set aligned radially.

2.3.1.3 The TRT

The TRT is the outermost part of the ID. It consists of $370,000$ straws made of coated polyamide film. Their diameter is $4\,\mathrm{mm}$ and their length is in the range $40 - 150\,\mathrm{cm}$ (depending on the straw position). In the barrel region, straws are parallel to the beam pipe and are mounted on rings. They are embedded in stacks of polypropylene/polyehylene fibre radiator which produces the transition radiation (TR). The end-cap straws are placed radially and regular foils are used for the TR production. Straws are filled with a mixture of $70\%Xe + 20\%CF_4 + 10\%CO_2$. Xe allows for detection of the transition radiation, and contributes significantly to the electron identification power of ATLAS. CF_4 increases the drift velocity and CO_2 is necessary to stabilize the gas avalanche amplification. The TRT also contributes to the accuracy of the momentum measurement by providing (on average) 42 measurements in $R - \phi$ direction with a resolution of $170\,\mu\mathrm{m}$ per point.

2.3.2 Calorimetry

In common with many general-purpose particle detectors, the ATLAS detector will be equiped with electromagnetic and hadronic calorimeters. The main calorimeter tasks are:

- an accurate measurement of the energy and position of electrons and photons;

- a measurement of the energy and direction of jets;

- a measurement of the missing transverse momentum;

- particle identification;

- event selection at the first trigger level.

The operational enviroment at the LHC poses several difficulties: the large center-of-mass collision energy implies the need for a good performance over an unprecedented energy range, extending from $< 1\,\mathrm{GeV}$ up to the TeV scale; at high luminosity a signal from the soft hadronic interactions will be piling-up with the event boths in space and time. A fast detector response and fine granularity are therefore required to minimize its impact on physics performance. A detailed description of the calorimeter's performance is available in [?] [20].

The ATLAS calorimetry is segmented into six different regions: the EM barrel, the EM endcap, the tile barrel, the tile "extended barrel", the hadronic endcap and the forward calorimeter. These regions are shown in Fig. 2.4. Although the geometry varies, the EM calorimeter uses a common technology (lead-liquid argon
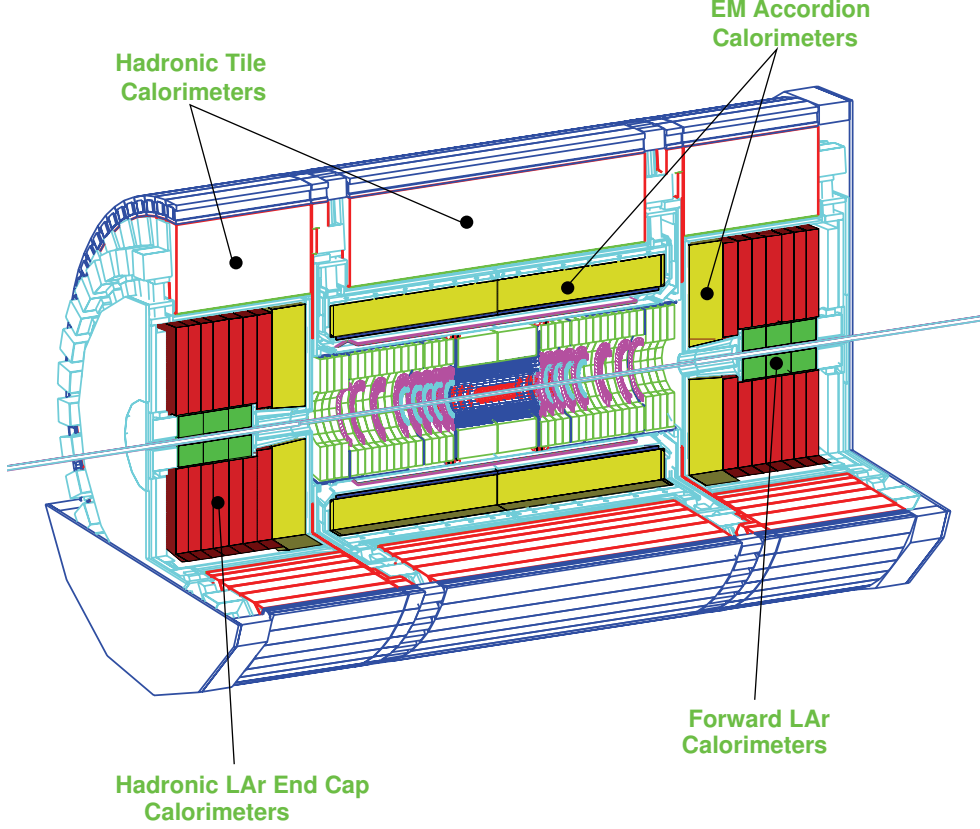
Figure 2.4: Three-dimensional view of the ATLAS calorimetry.

sampling calorimeter (LAr)) throughout. In contrast, the hadronic calorimeter uses different technologies in each of its three main rapidity regimes.

The coverage and granularity of the calorimeters are listed in table 2.2.

2.3.2.1   EM Calorimeter

The EM calorimeter is a lead-liquid-argon sandwich detector with accordion-shaped kapton electrodes and lead absorber plates over its full coverage. The lead thickness in the absorber plates has been chosen as a function of rapidity in order to optimise the calorimeter performance in terms of energy resolution. It covers the rapidity region $|\eta| < 3.2$ with total thickness of > 24 interaction lengths (X_0) in the barrel $(|\eta| < 1.475)$ and $\sim 26\,X_0$ in the end-cap $(1.375 < |\eta| < 3.2)$. The energy resolution is $\frac{\delta E}{E} = \frac{10\%}{\sqrt{E(GeV)}} \oplus 3\%$. The linearity of response is better than $0.5\,\%$ for energies up to $300\,GeV$. The Measurement of shower direction has a resolution of $\sim 50\,\mathrm{mrad}/\sqrt{E(GeV)}$.

Calorimetry system	η coverage	$\Delta\eta \times \Delta\phi$	sampling
Presampler	$\lvert\eta\rvert < 1.8$	0.025×0.1	
electromagnetic barrel	$\lvert\eta\rvert < 1.4$	0.003×0.1	(1)
		0.025×0.025	(2)
		0.05×0.035	(3)
electromagnetic end-caps	$1.4 < \lvert\eta\rvert < 3.2$	0.025×0.1	
hadronic barrels	$\lvert\eta\rvert < 1.7$	0.01×0.1	(1,2)
		0.02×0.1	(3)
hadronic end-caps	$1.5 < \lvert\eta\rvert < 2.5$	0.01×0.1	(1,2,3)
	$2.5 < \lvert\eta\rvert < 3.2$	0.02×0.2	(1,2,3)
forward calorimeter	$3.2 < \lvert\eta\rvert < 4.9$	$\sim 0.02 \times 0.2$	

Table 2.2: Summary of ATLAS calorimeters coverage and granularity.

The EM calorimeter is divided into towers pointing away from the interactionpoint and has three longitudinal samplings (Fig. 2.5). In the region $\lvert\eta\rvert < 1.8$ a presampler is installed in front of the calorimeter to correct for the energy lost in the upstream material. It is a $1.1\,\text{cm}$ thick ($5\,\text{mm}$ for $\lvert\eta\rvert > 1.5$) active LAr layer with a segmentation $(\Delta\eta \times \Delta\phi) = (0.0025 \times 0.1)$. The first sampling is $6\,X_0$ thick (including dead material and presampler) and has a granularity of $(\Delta\eta \times \Delta\phi) = (0.003 \times 0.1)$. This very high precision in η is needed for π^0/γ separation. The second sampling has squared towers of size $(\Delta\eta \times \Delta\phi) = (0.025 \times 0.025)$ and thickness of $16\,X_0$. The third sampling with thickness from 2 (central barrel) to $12\,X_0$ (end-caps) and a twice coarser granularity in η ($\Delta\eta \times \Delta\phi = 0.05 \times 0.035$) is reached only at transverse energies above $50\,\text{GeV}$, and is also used for the prediction of leakage into the hadronic calorimeter. In the region of transition from the barrel to the end-cap there is a crack in the active material ($1.4 < \lvert\eta\rvert < 1.6$). Scintillators are installed there to allow the measurement of energy lost in this region.

The distribution of material in terms of radiation lengths for both, the EM calorimeter, and the dead material in front of it, is shown in Fig. 2.6, and 2.7. For a more detailed description of this detector the reader is referred to [17].

2.3.2.2   Hadronic Calorimeter

The ATLAS hadronic calorimetry covers the range $\lvert\eta\rvert < 4.9$ using different techniques and devices as best suited for the different requirements and radiation enviroment. The main calorimeter task is the reconstruction of jets and the measurement of missing E_T. The energy resolution is $50\%/\sqrt{E} \oplus 3\%$ for $\lvert\eta\rvert < 3.2$ and $100\%/\sqrt{E} \oplus 10\%$ for $3.2 < \lvert\eta\rvert < 4.9$. The linearity of the energy measurement up to $4\,\text{TeV}$ is within 2%.

In the barrel region ($\lvert\eta\rvert < 1.5$) iron tile-scintillators are used with an overall thickness of 11 interaction lengths (X_0) and a granularity of $(\Delta\eta \times \Delta\phi) = (0.01 \times 0.1)$.
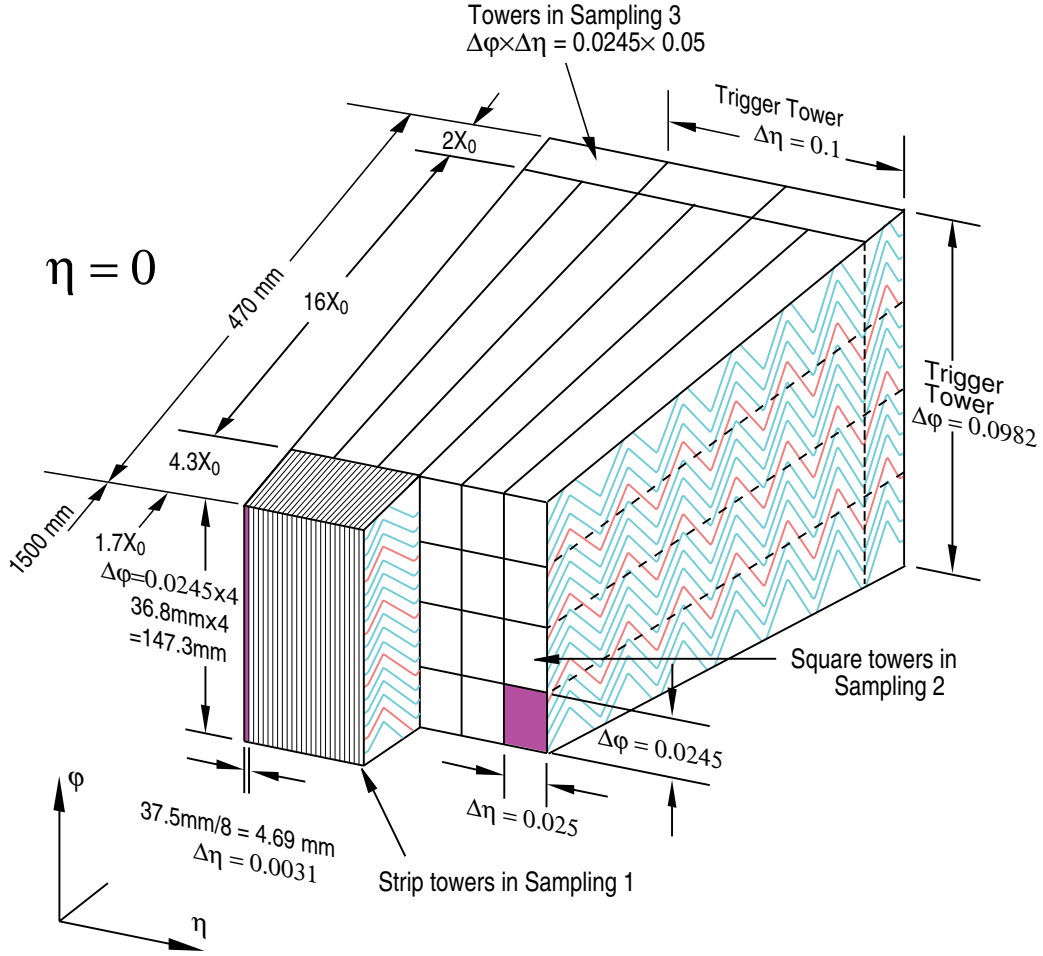
Figure 2.5: Readout granularity of the EM calorimeter.

The schematic of the tile calorimeter module is shown in Fig. 2.8.
In the end-cap and forward regions a similar technique as in the EM calorimeter (LAr accordion) is used due to the sensitivity of plastic scintillators to radiation damage. Copper is used instead of lead and the plates themselves are up to 10 times thicker in some parts. The granularity in this region is $(\Delta\eta \times \Delta\phi)$=$(0.022 \times 0.2)$ and the overall thickness is $14\,X_0$. More information can be found in [18].

2.3.3   Muon Spectrometer

High-momentum muons provide a clear and robust signature of physics at the LHC. To exploit this potential, the ATLAS collaboration has designed a high resolution muon spectrometer [19] with a stand-alone triggering and momentum measurement capability over a wide range of transverse momentum, pseudorapidity and azimuthal angle. The magnetic deflection of the muon tracks is induced by the air-core toroid magnets system (see section 1.3.4).
The muon spectrometer system is composed of two different types of detectors (Fig. 2.9): the Monitor Drift Tubes (MDT) perform a precision measurement of the tracks
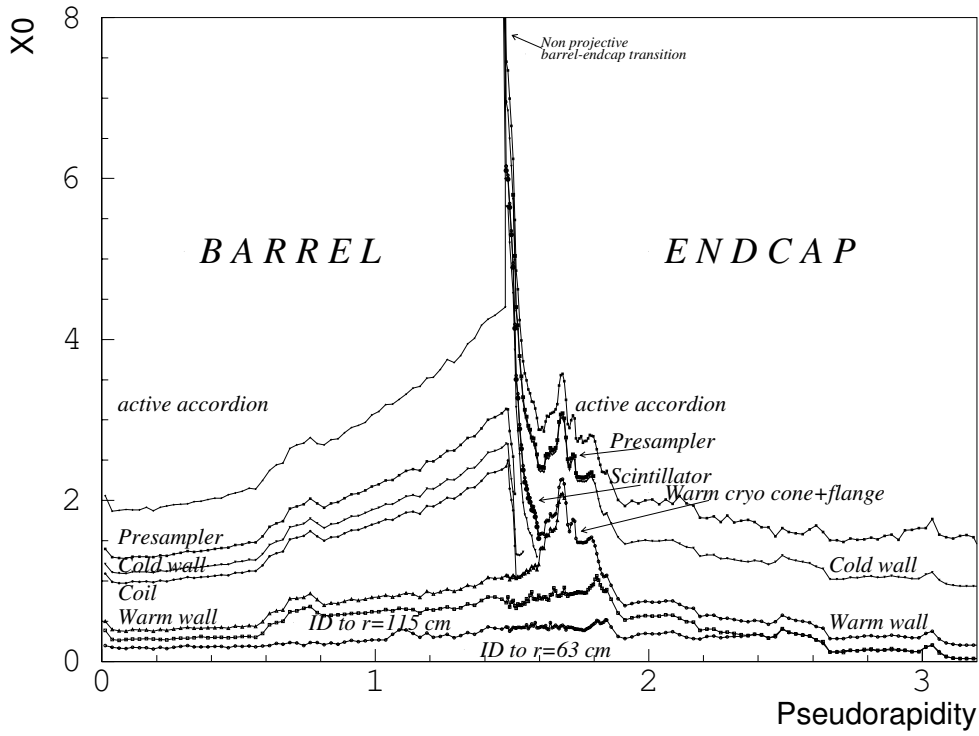
Figure 2.6: Breakdown of dead material(in X_0) up to the active EM calorimeter as a function of η.
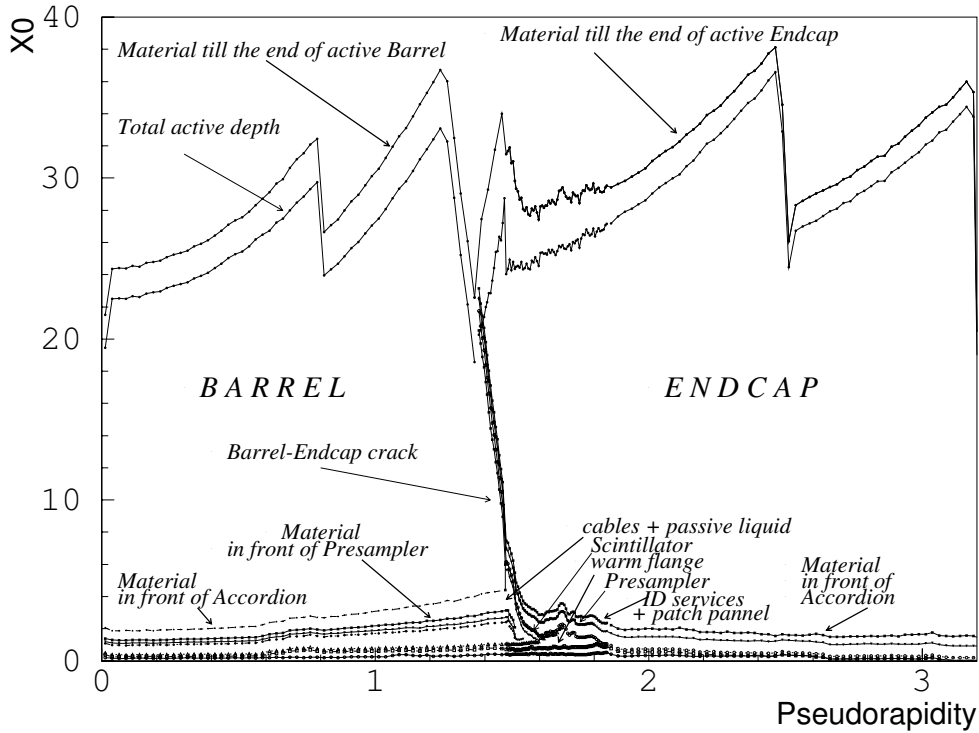
Figure 2.7: Total EM calorimeter thickness(in X_0) as a function of η.
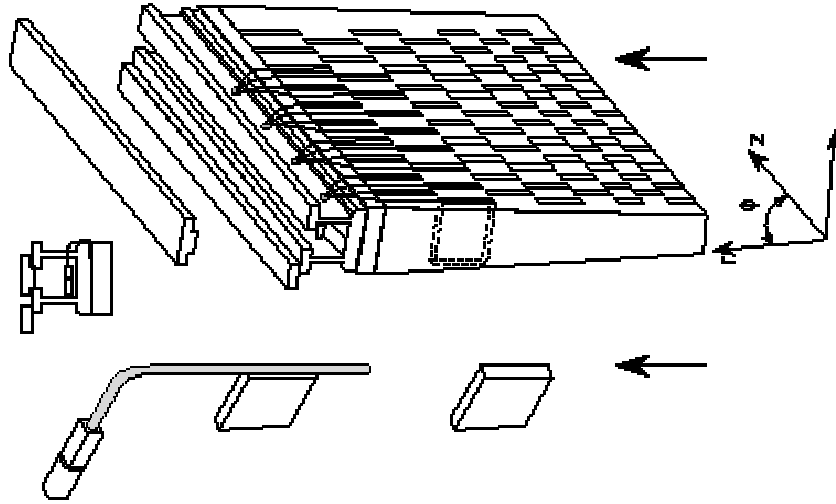
Figure 2.8: A module of the iron tile-scintillator.

coordinates in the principal direction of the magnetic field (axial) over most of the pseudorapidity range; the Cathode Strips Chambers (CSC) are used in the first station of the end-cap region and for pseudorapidity $|\eta| > 2$. This detector technique sustain the demanding rate and background conditions.

The required muon transverse momentum resolution is $\Delta p_T/p_T \simeq 1\%$ for transverse momentum $p_T > 6\,\text{GeV}/c$, and $\Delta p_T/p_T \simeq 10\%$ for transverse momentum $p_T > 1\,\text{TeV}/c$.

The expected muon identification efficiency is 90% at $p_T > 6\,\text{GeV}/c$.

The muon spectrometer is also equipped with trigger chambers; Resistive Plate Chambers (RPC) in the barrel region $\eta < 1.4$, and Thin Gap Chambers (TGC) in the end-cap regions. These chambers have a signal collection time better than the 25 ns LHC bunch spacing, and are used to trigger the acquisition of events satisfying a p_T threshold criteria.

2.3.4 Magnets System

The ATLAS detector system is provided with two different kinds of magnetic field (Fig. 2.10). A central superconducting-coil solenoid provides a 2T field to the ID in the region $|\eta| < 1.5$. It bends the charged particles that cross the tracking system, allowing the momentum measurement. The central solenoid is housed between the ID and the EM calorimeter, in the EM barrel cryostat, and its thickness in radiation length (X_0) and radial extension have been minimized to avoid degrading the EM calorimeter performance.

The muon spectrometer is equipped with a system of three large superconducting air-core toroids(one barrel, and two end-caps), that produce the magnetic deflection of the muon tracks. The large barrel toroid (20 m diameter) consists of eight coils that surround the hadronic calorimeter, and provides the magnetic bending in the region $|\eta| < 1.0$.
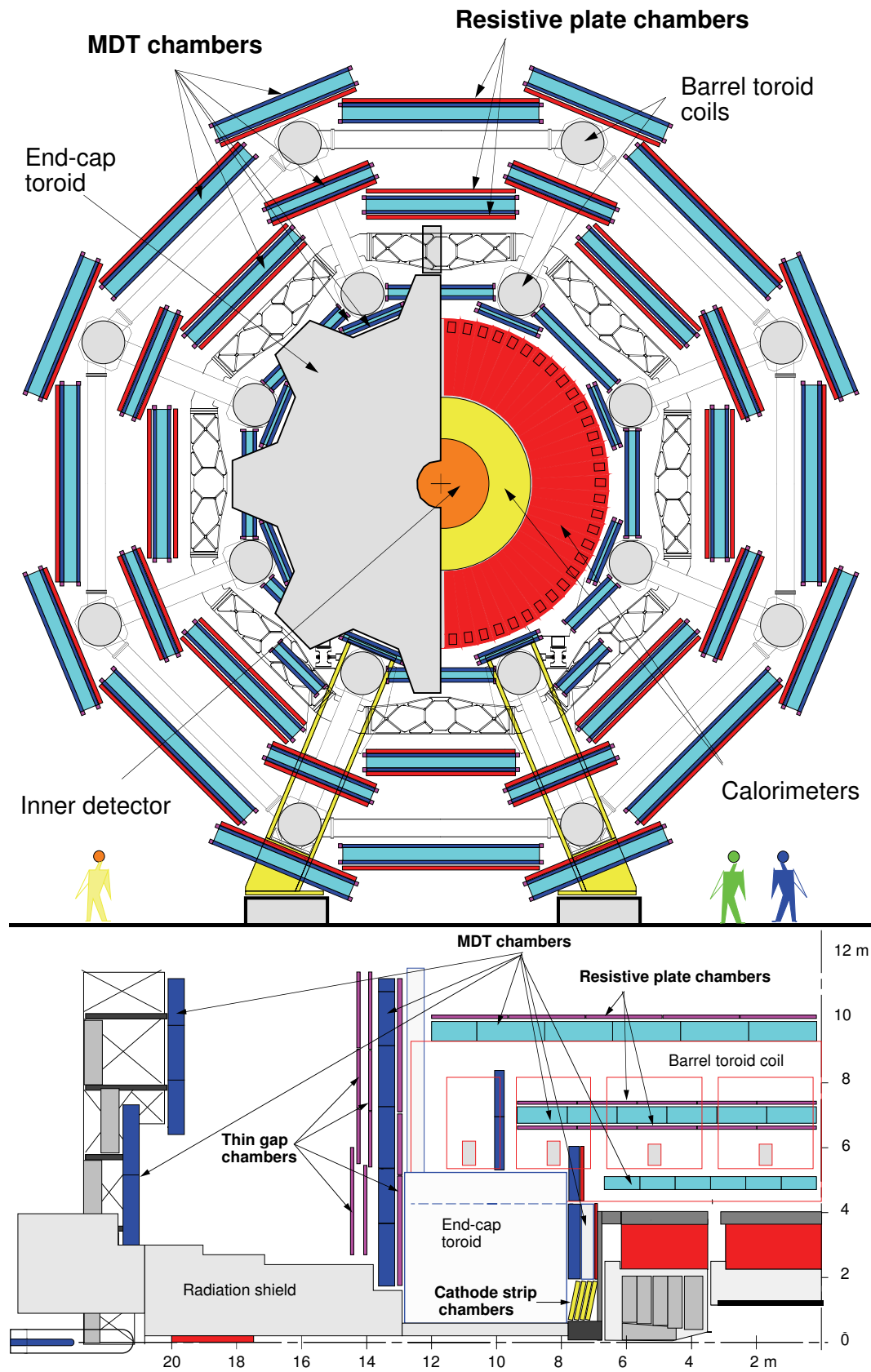
Figure 2.9: $x - y$ (top) and $r - \varphi$ (bottom) view of the ATLAS muon spectrometer.

In the $1.4 < |\eta| < 2.7$ region, the muon tracks are bent by the two smaller end-caps toroid, while in the $1.0 < |\eta| < 1.4$ range, the magnetic bending is provided by a combination of the barrel and end-caps toroid fields.
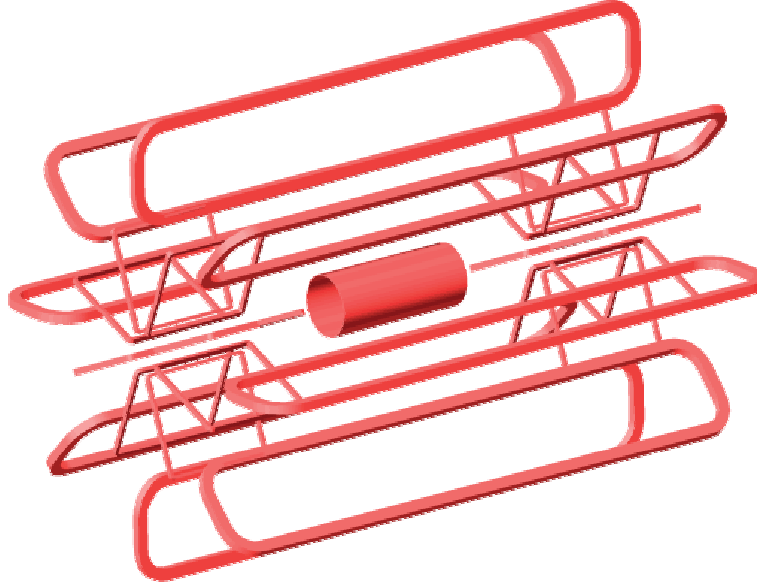
Figure 2.10: Tridimensional schematic view of the ATLAS magnet system. The central cylindrical coil of the superconducting solenoid is visible, surrounded by the air-core barrel and end-caps toroid coils.

2.4 Role of electrons in the ATLAS physics programme

As with any species of detectable particles in any experiment, its role in a particular decay channel can be twofold. Firstly, it can be part of the decay products, being its reconstruction efficiency and precision inportant parameters in order to measure the channel accurately. Secondly, it can form a part of the background, the reconstruction of which can result in effcient background rejection. In what follows an indication on the processes where electrons play a major role is given. A complete description of these processes can be found in [14].

2.4.1 Physics of the electro-weak gauge bosons

Gauge bosons and gauge boson pairs will be abundantly produced at the LHC. The large statistics and a high collision energy will allow several precision measurements to be carried out, which should improve significantly the precision achieved at present machines. Furthermore, their decay modes with electrons in the final state will be used to determine the mass scale of the EM calorimeter.

W mass

The W mass is one of the fundamental parameters of the Standard Model and is related to other parameters of the theory. Its uncertainty therefore in other measurements by introducing errors on theoretical calculations. The cross-section for the production of pp ($pp \rightarrow W + X$; $W \rightarrow l\nu$) with $l = e, \nu$ is $\sigma(W) = 30$ nb, giving approximately 300 million events in one year of data taking at the low luminosity. Half of those are electron events. The W mass measurement at hadron colliders is performed in the leptonic channels. Since the longitudinal momentum of the neutrino cannot be measured, the transverse mass m_T^W is used. The transverse momentum of the neutrino p_T^ν is obtained from the transverse momentum of the lepton p_T^l and that of the recoiling system u_T:

$$m_T^W = \sqrt{2 p_T^l p_T^\nu (1 - cos\Delta\phi)}$$
$$\vec{p}_T^\nu = -\vec{u}_T - \vec{p}_T^l$$

where $\Delta\varphi$ is the opening angle between the electron and the neutrino in the transverse plane. The distribution of the $m_T^W T$ is sensitive to the W mass which can therefore be obtained by fitting experimental distribution to the Monte-Carlo samples generated with different values of m_W.

Gauge boson pair production

The non-abelian gauge-group structure of the electro-weak interactions predicts very specific couplings between the gauge bosons. They are referred to as Triple Gauge Couplings (TGC) and Quartic Gauge Couplings (QGC). Any theory predicting physics beyond the SM can introduce deviations to these couplings. Precise measurements of the T/QGCs therefore provide not only a test of the SM but also a probe of a new physics in the gauge boson sector.

On ATLAS the TGCs will be observed in the leptonic decay modes of the W and WZ production. In both cases electrons in the final state represent one half of the expected sample.

2.4.2 B-physics

ATLAS will perform most of the B physics at the low luminosity running while some of the studies can be pursued further also at the high luminosity operation (most of it limited by the b-layer lifetime). The mean value of the B hadron transverse momentum in observable channels is 16 GeV or more. The LVL1 trigger for B physics will be an inclusive muon trigger with $p_T \geq 6$ GeV and $|\eta| < 2.4$. At LVL2 ATLAS will further trigger on the leptonic J/Ψ decays and $B_0 \rightarrow \pi^+\pi^-$. As the $J/\Psi \rightarrow ee$ decays will be one of the entry points into the B physics, the quality of the electron

reconstruction algorithms enters directly in the trigger rates. Further, it enters into the analysis of the CP violation studies where the angle β of the unitary triangle is measured via the $B_d^0 \to J/\Phi K_s^0$ channel. For B_s^0, the angle γ, the width difference $\Delta\Gamma_s$ and mixing parameter $x_s = \Delta m_s/\Gamma_s s$ will be observed via $B_s^0 \to J/\Psi\phi$.
Another important use of the $J/\Psi \to ee$ decay channel, although more technical in nature, is the calibration of the EM calorimeter at low energies.

2.4.3 Heavy quarks and leptons

Top quark physics

With the predicted production cross-section of $\sigma(t\bar{t}) = 833$ pb, the LHC will produce 8 million $t\bar{t}$ pairs per year of running at the low luminosity. An accurate measurement of m_t will improve the errors on theoretical calculations as well as help to constrain the SM Higgs boson mass. In the SM top quarks decay almost exclusively as $t \to Wb$. In 65.5% of all the events both W bosons will decay via $W \to jj$ or at least one W will decay via $W \to \tau\nu$. These events are hard to extract cleanly from the large multi-jet background and are not considered in ATLAS plans for the top physics. Instead at least one W is required to decay leptonically to either an electron or a muon. An energetic lepton with a large E_T provides a clean trigger signature and a large suppression of the multi-jet background.

Fourth generation quarks and leptons

The data from LEP and the Tevatron imply the existence of only three SM families with light neutrinos. Models with heavy neutrinos have been proposed and current experimental limits on the fourth generation quarks and leptons are $m_Q > 128$ GeV and $m_l > 80$ GeV. Fourth generation up-like quarks would predominantly decay via $u_4 \to Wb$, giving the same signature as the top quark. Again, at least one of the Ws will be required to decay leptonically. For down-like quarks the dominant decay mode would be $d_4 \to tW$. For $pp \to d_4\bar{d}_4 \to t\bar{t}W^+W^- \to W^+bW^-\bar{b}W^+W^-$ at least one of the Ws is required to decay into leptons. For heavy leptons $L \to NW$ (N is the heavy neutrino) has been studied in some detail but it is not entirely clear whether this process could be separated from the background of single and pair productions of the W and Z bosons.

2.4.4 Standard Model Higgs boson searches

The experimental observation of one or several Higgs bosons will be fundamental to a better understanding of the electro-weak symmetry breaking. Its discovery and spectroscopy is one of the main physics goals of the ATLAS experiment. The detector is designed to observe it over a mass range from 80 GeV to 1 TeV in a variety of decay channels, the choice of which is given by the signal rates and signal to back-

ground ratios in various mass regions. The main production channels of the Higgs boson at the LHC are shown in Fig. 2.11. As associated Higgs production ($Ht\bar{t}$, HW and HZ) is considered in all decay channels of interest and at least one lepton in final state is required by the trigger, efficient and accurate electron reconstruction is necessary for the analysis of the Higgs boson properties.
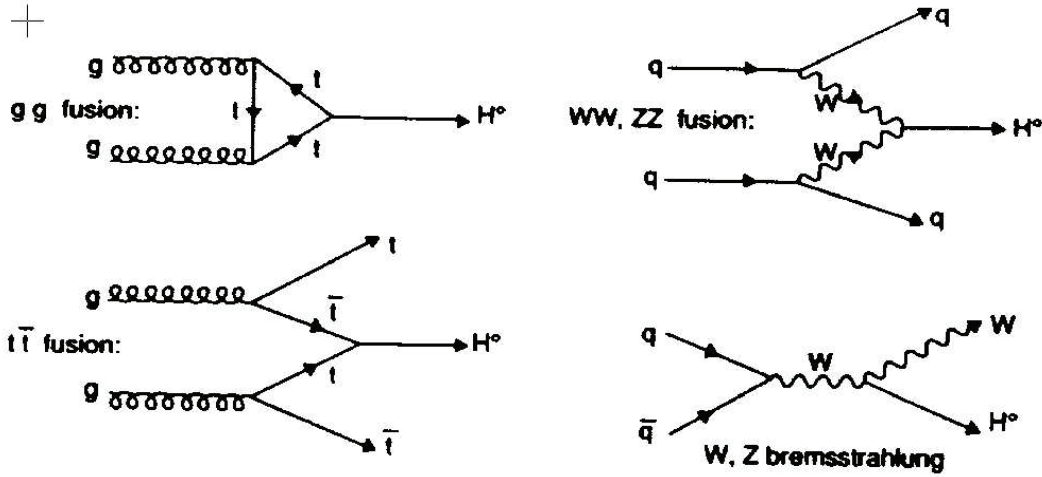
Figure 2.11: Feynmann diagrams representing major contributions to Higgs production cross-section in p-p collisions.

$H \rightarrow \gamma\gamma$

The decay mode $H \rightarrow \gamma\gamma$ is a rare decay mode, only observable over a limited Higgs boson mass range $80 < m_H < 150\,\text{GeV}$. The biggest problem for an effcient reconstruction is resonant background from $Z \rightarrow ee$ decays which has a production cross-section roughly 25 000 times larger than the signal. To reduce this background below the 10% level, a rejection of ~ 500 per electron is required by the inner detector track reconstruction.

$H \rightarrow ZZ^{(*)}$ **and** $H \rightarrow WW^{(*)}$

$H \rightarrow ZZ^* \rightarrow 4l$ provides a clean signature in the Higgs boson mass range from 120 GeV to $2m_Z$. The branching ratio increases with m_H up to $m_H \sim 150\,\text{GeV}$, where the $H \rightarrow WW$ channel begins to open up. Again, decay into leptons is favoured ($WW^{(*)} \rightarrow l\nu l\nu$) due to the abundant jet background at the LHC. In $WW^{(*)}$ it is not possible to directly reconstruct the Higgs boson mass peak. Instead one has to rely on properties of the distribution of reconstructed transverse mass [21].

In the case of $m_H > 2m_Z$ and up to 700 GeV, $H \rightarrow ZZ \rightarrow 4l$ is the most reliable channel for the discovery. For a larger m_H its width becomes the limiting factor

as the observed rates drop significantly. Only in this case the decay channels with jets in final states are also considered. The mass resolution in the decay channels including electrons is dominated by the EM calorimeter precision and therefore depends crucially on the calorimeter calibration.

Bibliography

[1] P.W. Higgs, Phys.Rev.Lett.**12**(1964)132 and Phys Rev.**145**(1966)1156;
F. Englert and R. Brout, Phys.Rev.Lett.**13**(1964)321;
G.S. Guralnik, C.R. Hagen and T.W. Kibble, Phys.Rev.Lett.**13**(1964)585.

[2] S. Weinberg, Phys Rev.**D13**(1976)974, Phys Rev.**D19**(1979)1277;
L. Susskind, Phys Rev.**D20**(1979)2619.

[3] R.Casalbuoni et al., hep-ph/9809523;
T.L. Barklow et al., hep-ph/9704217(Working group summary report from the
1996 DPF/DPB Summer Study, 'New Directions in High Energy Physics' Snow-
mass, Colorado);
R.Chivukula et al.,(in 'Electroweak Symmetry Breaking and New Physics at
the TeV Scale', World Scientific, T.Barklow,ed.,1996).

[4] The LHC project web site, *http://lhc-new-homepage.web.cern.ch/lhc-new-homepage/default-parameters.asp*

[5] J.Huston, 'LHC Guide to Parton Distribution Functions and Cross Sections',
ATLAS Internal Note ATL-PHYS-99-008(1999).

[6] H.L.Lai eta al.,preprint hep-ph/9903282(1999).

[7] A.D.Martin et al.,Eur.Phys.J.**C4**(1998)463.

[8] L.Kurchaninov, M.Levitsky, Pileup Noise Reduction with multiple samples,
LARG-NO-043(1996)

[9] L.Kurchaninov, M.Levitsky, Optimal Weighting of Signal Samples for LAr
Calorimeters, LARG-NO-044(1996)

[10] Weak Hamiltonian, CP Violation and Rare Decays, A.J. Buras, hep-
ph/9806471, to appear in the proceedings of "Probing the Standard Model
of Particle Interactions".

[11] Quark Mixing, CP Violation and Rare Decays After the Top Quark Discovery,
A.J. Buras and R. Fleischer, hep-ph/9704376, in "Heavy Flavours II", World
Scientific (1998), eds. A.J. Buras and M. Linder, p. 65-238.

[12] ATLAS Technical Proposal, 1994. CERN/LHCC/94-63.

[13] ATLAS Detector and Physics Performance Technical Design Report, 1999. CERN/LHCC/99-14.

[14] ATLAS Detector and Physics Performance Technical Design Report, 1999. CERN/LHCC/99-15.

[15] ATLAS Inner Detector Technical Design Report, 1997. CERN/LHCC/97-17.

[16] ATLAS Pixel Detector Technical Design Report, 1998. CERN/LHCC/98-13.

[17] ATLAS Liquid Argon Calorimeter Technical Design Report, 1996. CERN/LHCC/96-41.

[18] ATLAS Tile Calorimeter Technical Design Report, 1996. CERN/LHCC/96-42.

[19] ATLAS Muon Spectrometer Technical Design Report, 1997. CERN/LHCC/97-22.

[20] ATLAS Calorimeter Performance, 1996. CERN/LHCC/96-40.

[21] M. Dittmar and H. Dreiner. How to find a higgs boson with a mass between 155 GeV to 180 GeV at the LHC. *Phys. Rev.*, D55:167-172, 1997.

Chapter 3

The ATLAS Trigger/DAQ System

3.1   Introduction

The ATLAS experiment at the LHC will have to deal with the unprecedented bunch crossing rate of 40 MHz. At design luminosity, for each bunch crossing there will be on average 25 interactions, leading to an interaction rate of 10^9 Hz. It is technically not possible and not even envisageable to read out and store all these data, since most of them do not contain interesting physics events. The ATLAS experiment will therefore have an online triggering system capable of selecting interesting physics signatures, hence reducing the amount of data to be stored to approximately 100 MByte/s. While this requires an overall rejection factor of 10^7 against minimum bias processes, excellent efficiency must be retained for the rare new physics, such as Higgs boson decays. Much of the ATLAS physics programme at high luminosity can be carried out using inclusive triggers, at least at the earlier selection stages. These comprise inclusive selections of events containing high p_T muons, photons, electrons, taus, jets, as well as events with large missing transverse energy or total scalar transverse energy. In the later selection stages inclusive selections can be made of leptonic W and Z decays, making use of invariant mass information in the case of Z decays and missing transverse energy in the case of W decays. An advantage of inclusive triggers is that one may hope that they cover new, unpredicted physics.

The ATLAS trigger is a multilevel trigger system, as shown in Fig.3.1.

The LVL1 trigger is responsible for the greatest reduction in event/rate, from 40 MHz to 75 kHz. The LVL2 trigger and the event filter further reduce this rate to about 100 Hz.

The trigger algorithms at LVL1 act on reduced granularity data from a subset of the detectors (the muon trigger chambers and the calorimeters) and are implemented in very fast custom hardware processors based on Application Specific Integrated Circuits (ASICs) and Field Programmable Gate Arrays (FPGAs). The time needed to collect the data, make a LVL1 decision and distribute it, called the LVL1 latency, is $2\,\mu$s.
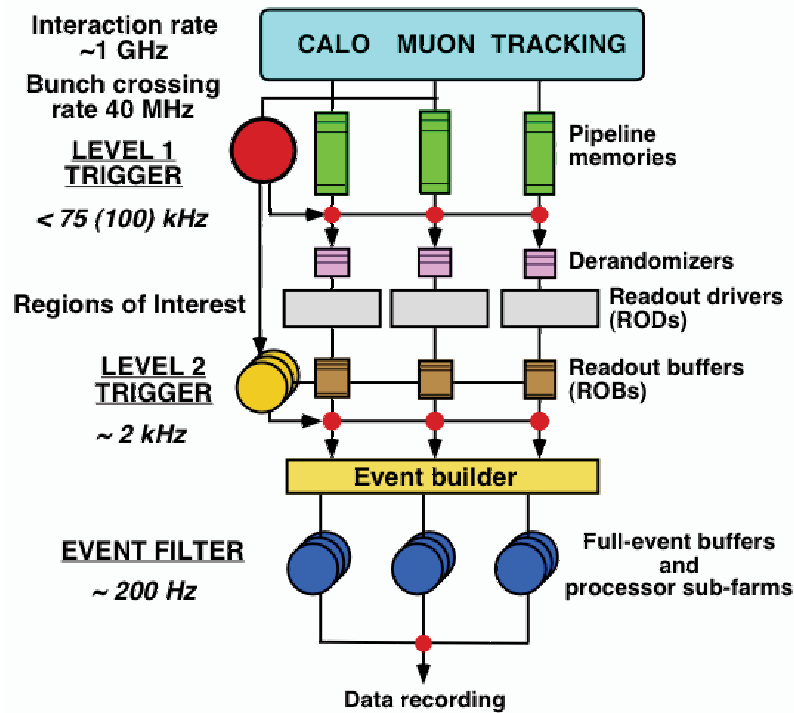
Figure 3.1: *Functional view of the ATLAS Trigger/DAQ system.*

Events selected by LVL1 are read out from the front-end electronics systems of the detectors into Read Out Drivers (RODs) and from there forwarded to Read Out Buffers (ROBs). While RODs are considered detector specific elements, the ROBs will be uniform throughout the ATLAS data acquisition system. Present estimates foresee about 1600 RODs in total. All of the data for the selected bunch crossing from all the detectors are held in the ROBs until the LVL2 trigger takes the decision to either discard the event or to accept it. In the latter case, the event is sent via the Event Building (EB) system to the Event Filter (EF). Whereas before event building each event is composed of many fragments, after event building the full formatted event is available to the EF.

The LVL2 uses full granularity, full precision data from the detectors, but examines only regions of the detector identified by the LVL1 trigger as containing interesting information, the Regions of Interest (RoIs). The EF uses the full event data together with the latest available calibration and alignment information to make the final selection of events to be recorded for offline analysis.

An important feature which has to be supported by the Data Acquisition system is the capability of running several disjunct and concurrent data taking sessions, that is, to be partitionable. The support for multiple partitions will be essential for purposes of detector debugging, calibration and testing.

3.2 The Trigger/DAQ Architecture

The Trigger/DAQ (TDAQ) system has been subdivided in four main functional elements: the Data Acquisition (DAQ), the Detector Control System (DCS),the LVL1 trigger, and the High Level Triggers (HLT) . The LVL1 trigger reduces the event rate from the bunch crossing rate to 100 kHz. The High Level Triggers (composed of the LVL2 trigger and the Event Filter) reduce the event rate which will be put to mass storage to about 200 Hz.

The DAQ is the system which deals with the movement of data from the RODs to mass storage, and with the initialization, control and monitoring of the experiment data taking. This system has been split into two systems, DataFlow and Online Software.

The Detector Control System (DCS) is the system responsible for the coherent and safe operation of the ATLAS detectors and all associated systems. It interfaces with the ATLAS subdetectors, the LHC machine and the CERN infrastructure and provides supervision and monitoring of operational parameters. The overall Trigger/DAQ architecture has been described in great detail in [1]; the LVL1 trigger in [3], and the HLT in [7]. Therefore, only a brief description of the main components is given here, emphasizing the event selection criteria mechanism at the different trigger levels, especially for the HLT part, where the electron selection performance studies represent the main contribution of this thesis research work.

3.3 The DAQ System

3.3.1 The DataFlow System

The DataFlow provides the functionality of receiving and buffering detector data from the Detector RODs, distributing events to the HLT and forwarding selected events to mass storage. It has been factorised into four subsystems: the ReadOut, the LVL2 DataFlow, the Event Builder and he the EF I/O. The ReadOut Subsystem (ROS) fulfills the task of receiving and buffering data coming from the RODs. The LVL2 DataFlow subsystem is responsible for handling the flow of events and control messages within the second level event selection system. The Event Builder collects all data fragments corresponding to the same bunch crossing from the ROS and builds a complete, formatted event. The EF I/O is responsible for passing the events assembled by the Event Builder to the Event Filter and for sending the events which survive the last selection criteria to mass storage.

3.3.2 The Online Software System

The online software system controls the overall experiment: it provides run control, configuration of the HLT and DAQ system and manages data-taking partitions.

3.4   The DCS

The task of the DCS is to facilitate the coherent and safe operation of the ATLAS detector and associated systems, and to interface with the LHC accelerator and the services of the CERN infrastructure. The requirements of the system are presented in [2].
The DCS comprises two subsystems: the Supervisory Controls And Data Acquisition (SCADA), and the Front-End Input/Output (FE I/O). The FE I/O reads out and digitizes signals from the detector hardware, implements low level control procedures and drives actuators. The SCADA system processes, displays, and archives data coming from the FE I/O and interacts with the operator.

3.5   The LVL1 Trigger

The ATLAS LVL1 trigger, whose block diagram is shown in Fig.3.2, is synchronous with the 40 MHz LHC clock, whose signal is distributed to all the system by the Timing, Trigger and Control system (TTC). The maximum output rate is limited to 100 kHz. The LVL1 trigger itself is divided into three sub-systems: the calorimeter trigger, the muon trigger and the Central Trigger Processor (CTP). Muon and calorimeter trigger sub-systems perform the initial selection based on reduced granularity data from a subset of detectors. The muon trigger uses only the trigger chambers, while the calorimeter trigger uses all of the ATLAS calorimeter, but with reduced granularity. The muon and calorimeter trigger are implemented by purpose-built hardware processors based on ASICs and FPGAs, with a fixed set of algorithms having programmable parameters. They work independently and in parallel in order to classify events in terms of particle transverse energy (E_T) and multiplicity. The features from these triggers are passed to the central trigger processor (CTP) which takes the overall decision to accept or reject the event. Then The CTP passes the decision on to the TTC system for distribution to the front-end system and detector elements. The accepted data, stored in the local pipeline memories until the decision is taken, are sent to the RODs and afterwards to the ROBs. The LVL1 trigger accepts externally generated trigger signals, enabling calibration of the trigger, and must be able to provide unique bunch-crossing identification (BCID).

3.5.1   The Calorimeter Trigger

The input of the LVL1 calorimeter trigger is made up of trigger towers with a coarse granularity of 0.1×0.1 in η and φ, giving a total of 7200 channels. The chosen granularity is a balance between rejection of background and cost and complexity of the trigger processor. The energy for each trigger tower is provided as an analog sum of the energies of the corresponding cells. There are separate set of trigger towers for EM and hadronic calorimeter. The LVL1 calorimeter trigger performs four
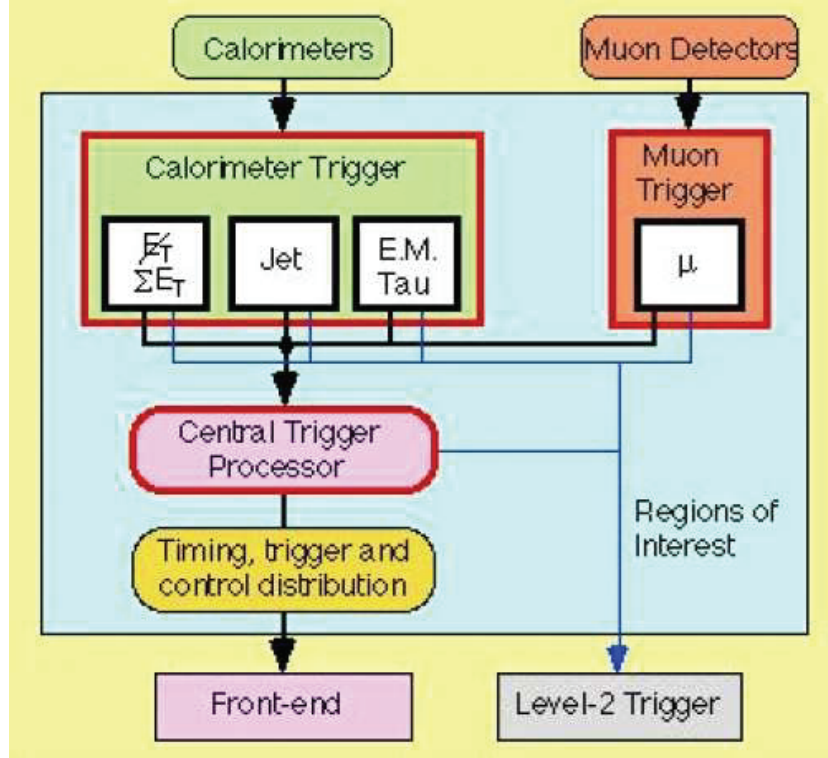
Figure 3.2: *Block diagram of the ATLAS LVL1 trigger.*

basic algorithms: an e/γ, a hadron/τ, a jet and a sum-E_T/E_T^{miss} trigger. The basic elements for the algorithm construction are shown in Fig. 3.3. Each algorithm identifies objects classified according to their transverse energy. The number of objects passing a programmable E_T-threshold is counted as multiplicity. The multiplicity of objects is then sent to the CTP for eight different thresholds, where objects are further evaluated. The coordinates (RoIs) of the identified object are sent to the LVL2 trigger.

3.5.2   The Muon Trigger

The LVL1 muon trigger is based on the measurement of muon trajectories in two or three different planes, called stations, whose location is outlined in Fig. 3.4. The stations are equipped with dedicated fast muon detectors. In the barrel these are Resistive Plate Chambers (RPC), in the end-cap Thin Gap Chambers (TGC). Each station has a chamber doublet, except for the inner end-cap station which has a triplet. The timing resolution of both kinds of detectors is sufficient to provide an unambiguous identification of the bunch crossing containing a high p_T muon candidate. Muons are bent by the magnetic field generated by the toroids and their angle of deflection depends on their momentum, the field integral along their trajectory and the Coulomb scattering in the material lying in front of the trigger planes. The energy loss fluctuation is also important for low p_T triggers. The algorithm is based on the measurement, using the three trigger station, of the reconstructed track
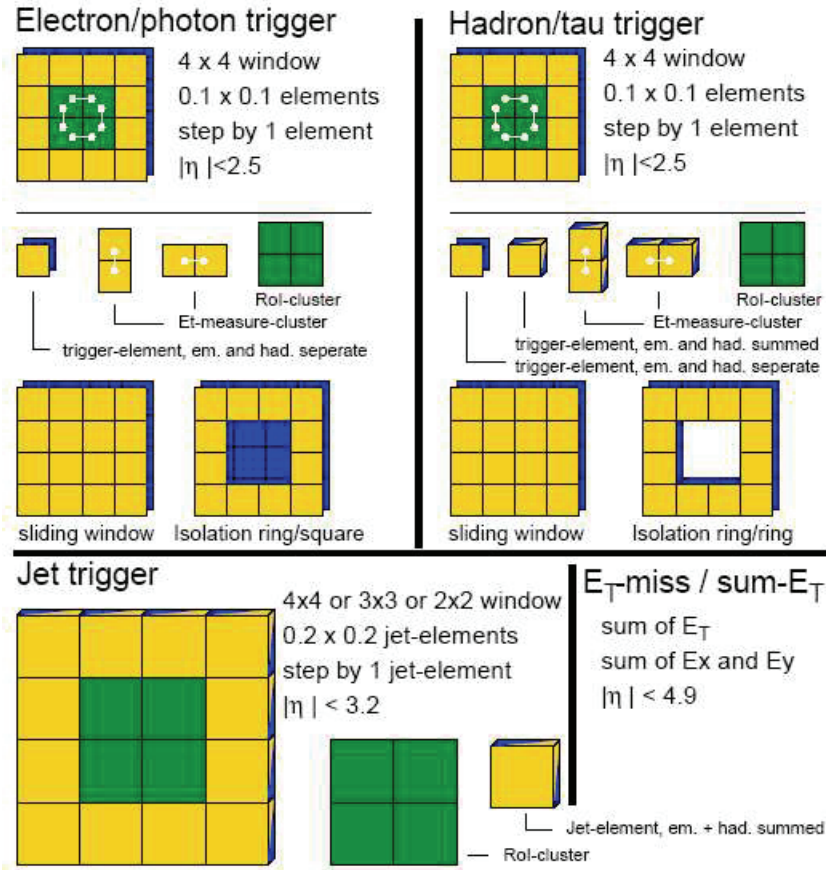
Figure 3.3: *The basic elements of the calorimeter trigger algorithms: the electron/photon trigger, the hadron/tau trigger, the jet trigger and the sum-E_T/E_T^{miss} trigger.*

residual with respect to a hypothetical infinite p_T track. The trigger plane farthest from the interaction point, in the end-cap, or nearest to the interaction point, in the barrel, is called the pivot plane. Two different lever arms from the pivot to the other two trigger planes provide two different measurements of the residuals. The two different lever arms allow trigger thresholds to cover a wide range of momenta: the shorter lever arm (the pivot and station 2) covers a lower momentum region ($p_T > 6$ GeV) and the longer one (the pivot and station 1 in the end-cap, the pivot and station 3 in the barrel) a higher momentum region ($p_T > 20$ GeV). The p_T resolution in turn is a function of the trigger detector geometry, the integral magnetic field with its inhomogeneities, the multiple Coulomb scattering in the central calorimeter and the width of the interaction region. The most important physics effect is the Coulomb scattering mainly for the low-p_T thresholds. The typical p_T resolution at trigger threshold is 30% in the barrel and 10% in the end-cap for muons of 6 GeV and 40% in the barrel and 15% in the end-cap for muons of 20 GeV.

A tight time coincidence among hits is also required to identify the bunch crossing and to reduce the trigger rate from accidental coincidences induced by the cavern background.
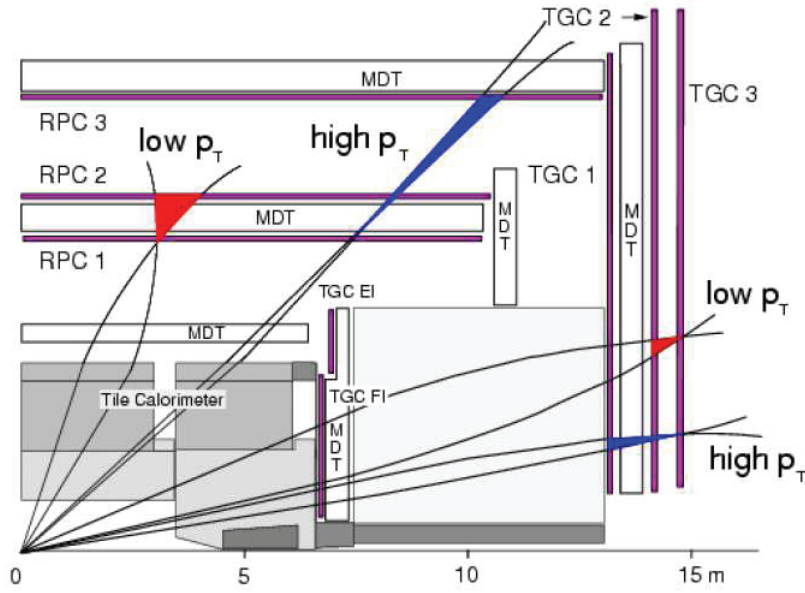
Figure 3.4: *The trigger chamber location in the muon spectrometer and the principle of the LVL1 algorithm used to identify muons. Depending on the value of the nominal p_T threshold, roads of different size are used to form coincidences between hits in different layers.*

3.5.3   The Central Trigger Processor

The central trigger processor (CTP) makes the overall decision to accept or reject the event on the basis of the multiplicities of the following local and global trigger object for various p_T thresholds:

- muon;

- electromagnetic cluster, where isolation can be required;

- narrow jets (isolated hadronic τ decays or isolated single hadrons);

- jets;

- the missing transverse energy;

- the total scalar transverse energy.

The global decision at LVL1 is made by the CTP by comparing the list of detected trigger objects to a list of required signatures, which have been derived from the physics requirements. A signature is defined in this context as a collection of objects that the event needs to be accepted. Thresholds and attributes for the trigger objects are optimized to meet the requirements of high efficiency and acceptable rate. A total of up to 96 menu items are currently foreseen for the CTP. The triggers are inclusive, and cover not only physics but also detector monitoring, which must run

continuously during physics data taking.

The CTP allows the implementation of programmed pre-scale factors which can be used to down-scale high-rate triggers. These can be used to understand and monitor thresholds and background, and to collect data for standard physics studies (e.g. QCD measurements). The CTP is also responsible for the control and generation of dead times, which have been introduced in order to:

- accommodate front-end electronics limitations (a short dead time of three bunch crossing is systematically introduced after each LVL1 accept signal)

- prevent derandomizer overflows (the CTP limits the number of LVL1 accept signals that can be generated within a given period of time)

- handle the occupancy of the ROD and ROB buffers (the CTP can be vetoed with an external signal)

3.5.4 The TTC System

The ATLAS read-out elements, such as the front-end electronics, the RODs and the ROBs need the bunch-crossing signal (BC) and the LVL1 accept signal (L1A). The TTC system allows these signals to be distributed to the read-out electronics elements. The timing signals comprise the LHC clock and the synchronization signals (Bunch Counter Reset (BCR), and the Event Counter Reset (ECR)). The trigger signals include the L1A and test and calibration triggers. The TTC system allows the timing of these signals to be adjusted.

An important feature of the TTC system is that it allows the partitioning[1] of the ATLAS detector for the purposes of detector commissioning, calibration, testing and debugging. The TTC itself is partitioned and sub-detectors can be run with the central ATLAS timing and trigger signals, or independently, with their own specific timing and trigger signals injected directly in the relevant TTC partition. The number of TTC partitions defines the number of concurrent and disjunct data taking sessions that the DAQ will have to be able of support. At present, it is foreseen to have about 40 TTC partitions.

---

[1]A partition is a subset of the experiment with the capability to acquire data independently. It can be a complete sub-detector, a part of a sub-detector or the combination of several sub-detectors (in other words, several partitions can be combined into a higher-level partition). The data-taking can be done at the level of the RODs or through the complete DAQ system. A partition requires an independent TTC system and an independent handling of the dead time.

3.6 The High Level Triggers

3.6.1 Overview

The High-level Trigger (HLT) consists of the second and third stages of event selection. It comprises three main parts: The LVL2 system, the Event Filter (EF), and the Event Selection Software (ESS). Although the algorithms used at LVL2 and the EF are different, it has been decided to use a common software architecture for the event selection code across LVL2, EF and offline studies. This facilitates the use of common infrastructure (such as detector calibration and alignment data) and simplifies offline studies and development of the HLT algorithms.

The starting point for the HLT is the LVL1 Result. It contains the LVL1 trigger type and the information about primary RoIs that caused the LVL1 accept, plus secondary RoIs not used for the LVL1 accept. Both types of RoIs are used to seed the LVL2 selection. The concept of seeded reconstruction is fundamental, particularly at LVL2. The LVL2 result provides a seed for the EF selection, thus playing a similar role for the EF as does the LVL1 result for the LVL2. It will also be possible to seed the EF directly with the LVL1 result in order to study, for example, the LVL2 performance. The EF and the LVL2 results, containing the physics signatures from the trigger menu that were satisfied and higher level reconstruction objects, will be appended to the raw event data.

The EF classification is yet to be defined in detail. Possibilities considered include special selections for calibration events and for new physics signatures, i.e. a discovery stream. The EF result can be used to assign tags to the events or even assign them to particular output streams.

Figure 3.5 shows the exchange of messages involved during an HLT process. The flow of data is as follows. Data for events accepted by the LVL1 trigger are sent from the detector front-end electronics to the ROSs, containing 1600 ROBs. In parallel, information on the location of RoIs identified by LVL1 is sent to the LVL2 Supervisor to guide the LVL2 event selection.

The LVL2 Supervisor sends the LVL1 Result to the LVL2 Processing Unit (L2PU), where the LVL2 selection is performed. Using the LVL1 Result as guidance, specialized LVL2 algorithms request a sub-set of the event data from the ROSs to perform the event selection. In this way only a few per cent of the event data needs to be transferred to the LVL2 system, thus considerably reducing the network bandwidth required. For events accepted by LVL2, details are sent to the ROS (in the LVL2 Result) to be included in the event. The L2PU send the LVL2 Decision back to the LVL2 Supervisor, which forwards them to the Event Builder. Within the Event Builder the Sub Farm Input (SFI) assembles each accepted event into a single record, including the LVL2 result. The built event is then transfered to the Event Handler where the events are distributed to Event Filter Processing Tasks (EF PT), where offline algorithms are applied guided by information from the LVL1 and LVL2 triggers to further refine the event selection. Events passing the EF are then passed
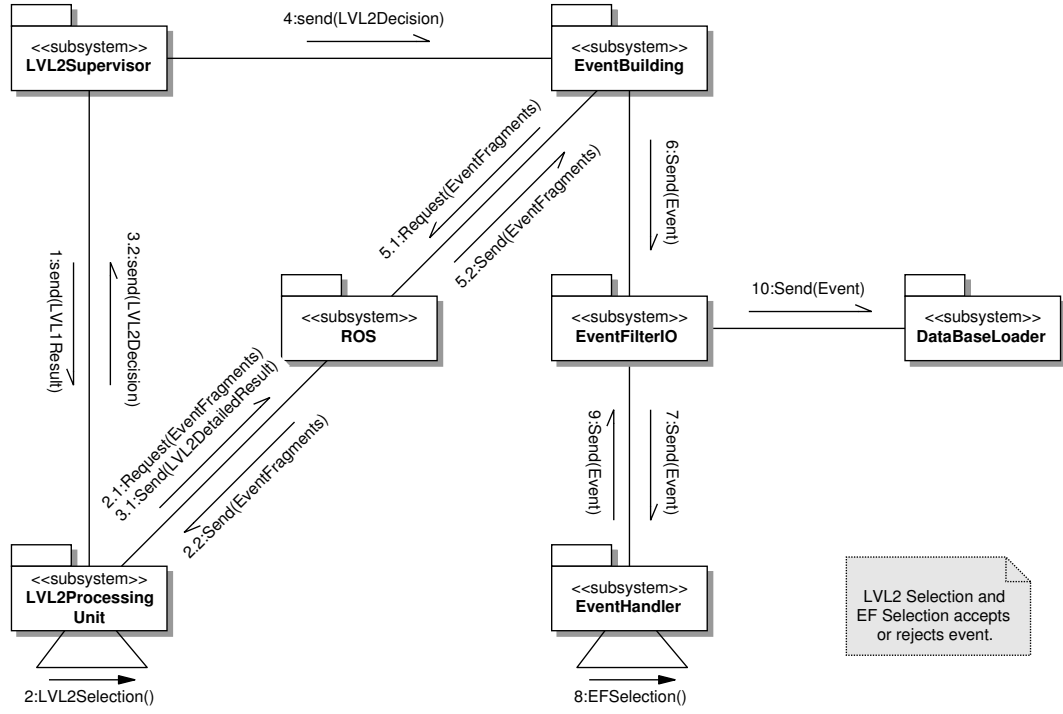
Figure 3.5: *Functional view of the ATLAS Trigger/DAQ system.*

to the Sub Farm Output (SFO) for permanent storage and offline analysis.

The architecture adopted by the ATLAS HLT community [7] increase the complexity of the system, but as a payback, the network bandwidth is significatly reduced. The next subsection will describe briefly the main features of the HLT design.

3.6.2 The LVL2 Trigger

The aim of the LVL2 trigger is to reduce the acceptance rate from 75 kHz (100 kHz maximum) to a level sustainable by the event building, in the range of 1 kHz. The architecture of LVL2, [11] [12] is based on the use of RoIs defined by the LVL1 trigger. These are regions of the detector containing features consistent with interesting physics objects, such as high-p_T muons, electromagnetic clusters (electrons/photons) and jets. With this guidance the LVL2 trigger only needs access to a small fraction of the total event data implying a corresponding reduction in the required processing power and data-moving capacity. The RoIs are complemented by general event properties such as the total scalar E_T and the E_T^{miss} vector.

The LVL2 trigger uses full data granularity, full precision data from the calorimeter and muon detectors, and also full precision data from the tracking detectors. For each RoI, the features from all the subdetectors are combined to provide better particle identification and more precise measurements than were possible at LVL1. The target average computing time for LVL2 is 10 ms. After the LVL2 trigger accepts an event, the data for that event are transferred to the EF via the event builder.

The event processing in the LVL2 trigger can be divided into three steps: the feature extraction, object building and trigger type selection. In the feature extraction, the data for one RoI from one detector are processed to extract physics-like quantities, for example track segments, or calorimeter cluster energy. The object building step takes the features for one RoI from all detectors and returns the particle parameters, for example p_T and direction, and tries to identify the particle type such as electron or photon. The trigger type selection, combines all objects from an event and compares that to the physics selection menus or trigger menus.

3.6.3 The Event Filter

The task of the EF is twofold: to reduce the final event rate to about 200 Hz, and to classify the events in different streams of interesting processes.

Event filtering is executed on fully assembled events, containing the entire detector information, and including the results of the lower level trigger. The selection is based on off-line algorithms which obviously cannot be executed earlier, either because they require correlated information from different parts of the detector or because they are too complex to be implemented on the LVL2 processors within a time compatible with the required targeted average processing time. Depending on the processing time needed by the algorithms, the processing power available, and the stability of the calibrations and beam position, one may aim at completing in the EF the reconstruction to such a degree that the subsequent analysis steps have only to perform hypothesis-dependent updates of the reconstruction. Algorithms that could be executed at this level are vertex reconstruction and track fitting, bremsstrahlung recovery for electrons, or operations that require larger RoI than that used at LVL2, such as photon conversion search or calculations requiring the complete event data (missing E_T calculation). The EF completes the classification of the events, establishes a catalogue according to trigger type events and stores accepted events in the database.

In addition to its primary task of event filtering and data reduction, the EF, being the first element in the DAQ chain having access to complete events, will also be used for calibration and monitoring studies. Many types of monitoring, including inter-detector efficiencies, physics quality assurance and trigger performance can be envisaged, as well as specialized calibration studies.

3.6.4 The Event Selection Software

The ESS is one of the main components of the HLT system, and is the responsable for the classification and selection of the events.

The tasks of the ESS are event selection and event classification. Abstract objects representing candidates such as electrons, jets, muons, etc. are reconstructed from event data by using a particular set of HLT algorithms and applying appropiate selection criteria. An event is selected if the reconstructed objects satisfy at least

one of the physics signatures given in a trigger menu. In both LVL2 and EF, events are rejected if they do not pass any of the specified selection criteria, which are designed to meet the final efficiency and rate reduction targets of the trigger system. From a physics event selection point of view there is no precise boundary between LVL2 and EF. Indeed, flexibility in setting the boundary is important to take advantage of the complementary features of these trigger stages.

A key concept within the ESS infrastructure is the Steering mechanism [8], motivated by the need to have fast and early rejection of uninteresting events in a flexible and configurable manner and by the need to deal with special trigger configurations such as the pre-scale/force accept of some events. At the core of the ESS Steering is the Steering Controler [9], which is the software component in charge of the control, and proper guidance of HLT algorithms through the different steps leading to the validation of a final signature. It is designed in a way that allows full control of the algorithm execution within the HLT processing flow with the simple modification of XML configuration files.

One of the policies established by HLT collaboration is that the ESS must also be able to run directly in the offline software enviroment of ATLAS (ATHENA [10]). The benefits from this are numerous: it facilitates the development of algorithms; allows the study of the boundary between LVL2 and Event Filter and leads to easy performance studies for physics analysis. The ESS needs therefore to comply with the control framework and services that are provided by the offline framework architecture. For this reason, ATHENA was adopted as the software framework running the ESS in both the EF, and (in a modified form due to design restrictions) the LVL2 processing units.

3.6.5 HLT Strategy

3.6.5.1 The Region of Interest Mechanism

The information gathered at LVL1, for example the geometrical position in η and φ of the tagged objects and the thresholds they passed, is sent to the Region of Interest Builder (RoIB) which combines it into a single record that is passed to Level2 Supervisors (L2SV).

This way only data contained in RoBs corresponding to detector modules inside the LVL1 RoI will be processed by the Online software and moved to the L2P, thus saving a lot of network bandwidth and processing time.

In particular, the conversion of a geometrical (η, ϕ) region into identifiers, each corresponding to a Detector Element in a sub-detector, is performed by the HLT Region Selector [5], whose operation is depicted in Fig.3.6. This tool uses information from the detector description to build fast lookup tables mapping each (η, φ) position into the sub-detector Detector Elements from which to request data.
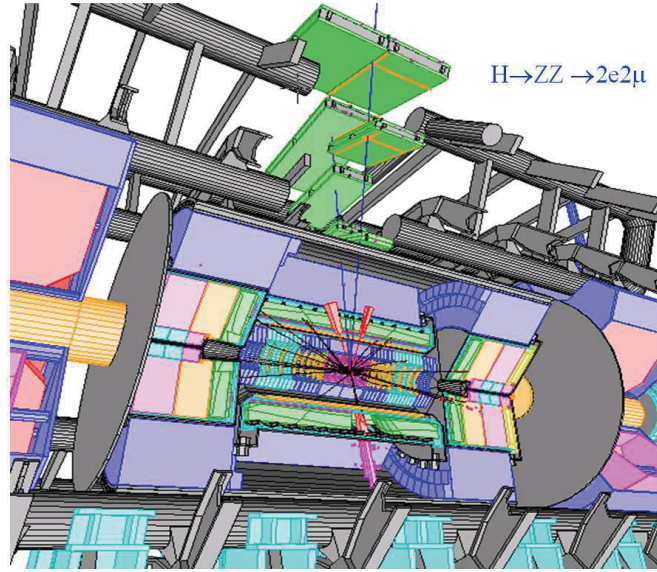
Figure 3.6: *The RoI concept. In this example, only the sub-detector data surrounding the Higss decay product are accessed by the HLT Algorithms.*

3.6.5.2   Algorithm Data Access

As discussed above, the Region-of-Interest mechanism allows for an optimized retrieve of the data necessary to perform the LVL2 decision. Another fundamental part in the design of the HLT architecture is the way in which an HLT algorithm accesses the data. Figure 3.7 shows a diagram with the main software components, and the flow of data between them.

The data is stored in collections within the Transient Data Store (TDS) [6]. These collections (C++ object-oriented objects, more suitable for the algorithms) are organized inside a container with infrastructure for easy retrieval and sorting, and are identified uniquely via an offline identifier [7].We can see from the diagram that the HLT algorithm first asks the RegionSelector tool for the list of collection identifiers associated with a particular region, that could correspond for example to an (η, ϕ) region that would come from LVL1. With the list of collection identifiers in hand, the HLT algorithm requests the associated data to the TDS. If the data is already cached within the TDS, the requested collections are returned. If the data is not cached, the TDS launches the ByteStream Converter whose goal is to fill the collections in the TDS using the data in ByteStream format. To get hold of this data, the ByteStreamConverter must request specific ROBs to the ROBDataCollector. Finally, at LVL2 there is the possibility to do some data preparation from within the ByteStreamConverter, which leads to a faster execution of the LVL2 trigger algorithms.

3.6.5.3 Physics Selection

Event selection at LHC faces a huge range in cross-section values for various processes, as shown in Fig. 3.8. The interaction rate is dominated by the inelastic part of the total cross-section with a cross-section of about 70 mb. The inclusive production of b-quarks occurs with a cross-section of about 0.6 mb, corresponding to a rate of about 6 MHz for design luminosity. It is worth noting that the cross-section for inclusive W production, including the branching ratio for the leptonic decays to an electron or a muon, leads to a rate of about 300 Hz at design luminosity. The rate of some rare signals will be much smaller, e.g. the rate for the production of a Standard Model Higgs boson with a mass of 120 GeV for the rare-decay mode into two photons will be below 0.001 Hz. The selection strategy has to ensure that such rare signals will not be missed, while at the same time reducing the output rate of the HLT to mass storage to an acceptable value.

In order to guarantee optimal acceptance to new physics within the current paradigm of particle physics, an approach based on emphasizing the use of inclusive criteria for the online selection has been taken, i.e. having signatures mostly based on single- and di-object high-p_T triggers. Here 'high-p_T' refers to objects such as charged leptons with transverse momenta above $O(10)$ GeV. The choice of the thresholds has to be made in such a way that a good overlap with the reach of the Tevatron and other colliders is guaranteed, and there is good sensitivity to new light objects, e.g. Higgs bosons. Enlarging this high-p_T selection to complement the ATLAS physics potential requires access to signatures involving more exclusive selections, such as requiring the presence of several different physics objects or the use of topological criteria.

The ATLAS trigger relies on the concept of physics 'objects' (muons, electrons, jets, etc.). Candidate objects are typically first identified and crudely reconstructed at LVL1. Processing in the HLT progressively refines the reconstruction, rejecting
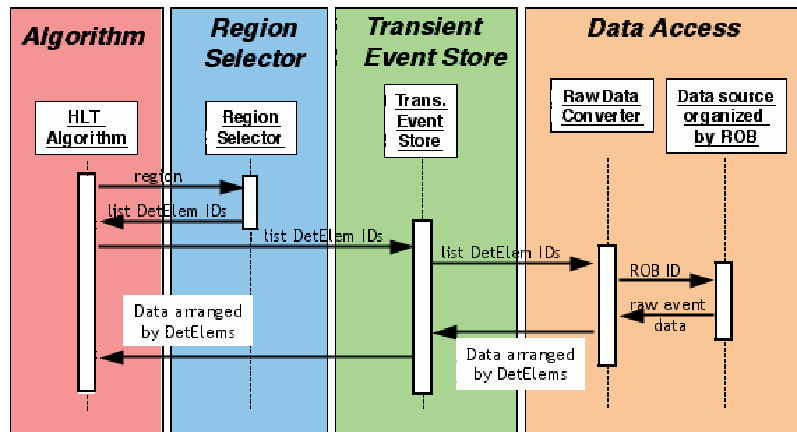
Figure 3.7: *Schematic sequence diagram of HLT algorithm data access.*
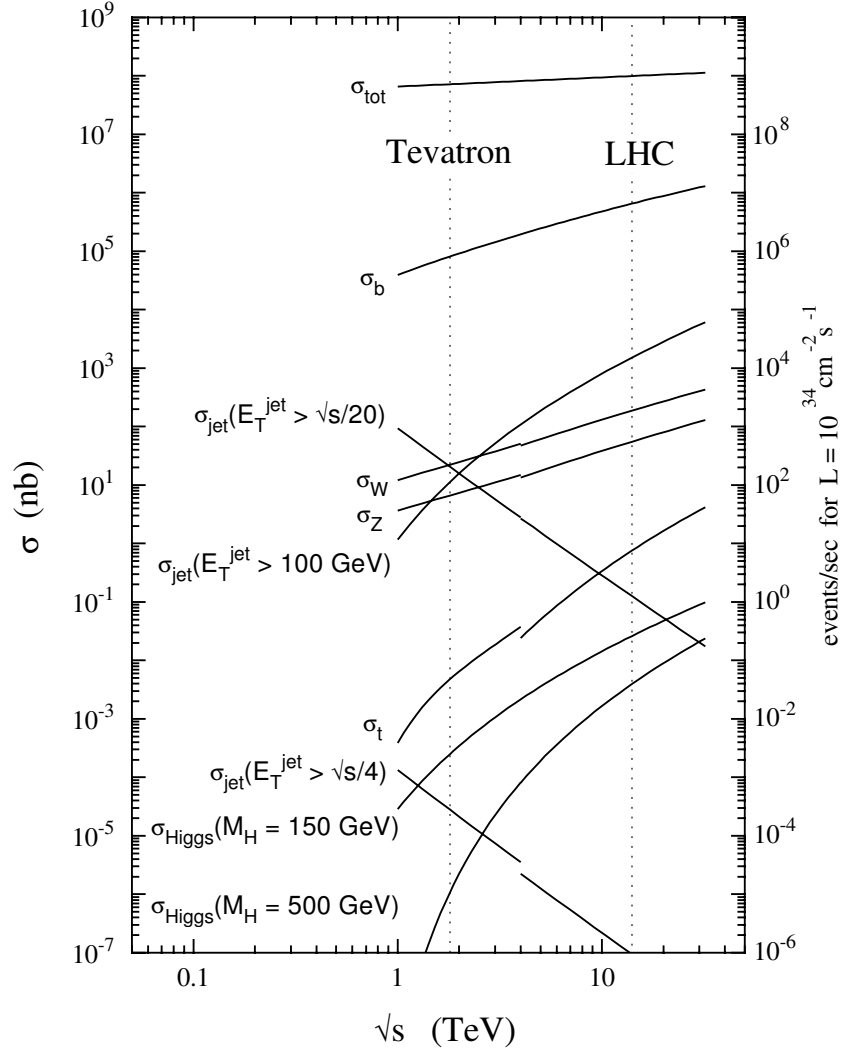
Figure 3.8: *Cross-section and rates (for a luminosity of $2 \times 10^{33}\,\mathrm{cm^{-2}s^{-1}}$) for various processes in proton (anti)proton collisions, as a function of the centre-of-mass energy.*

fake objects and improving the precision on measured parameters such as E_T. The different types of triggers envisaged for running at an initial peak luminosity of $2 \times 10^{33}\,\mathrm{cm^{-2}\,s^{-1}}$ are:

- inclusive physics triggers that form the backbone of the online selection and are chosen to guarantee the coverage of a very large fraction of the ATLAS physics programme;

- prescaled physics triggers that will extend the physics coverage for ATLAS by having, for example, inclusive selections with lower thresholds to enlarge the kinematic reach and provide samples for understanding background processes and detector performance;

- exclusive physics triggers that will also extend the physics coverage for ATLAS;

May 26, 2006

- dedicated monitor and calibration triggers not already contained in one of the above items, for improving the understanding of the performance of the ATLAS detector, based on physics events not needed otherwise for physics measurements; furthermore, specific selections might be used to monitor the machine luminosity.

In what follows, only the inclusive physics triggers will be briefly discussed. A more detailed description of the above mentioned trigger types can be found in [7].

Table 3.1 gives an overview of the major selection signatures needed to guarantee the physics coverage for the initial running at a peak luminosity of $2 \times 10^{33} \, \mathrm{cm^{-2} \, s^{-1}}$.

As can be observed, a large part of the physics programme will rely heavily on the inclusive single- and di-lepton triggers, involving electrons and muons. Besides selecting events from Standard Model processes (such as production of W and Z bosons, gauge-boson pairs, $t\bar{t}$ pairs, and the Higgs boson) they provide sensitivity to a very large variety of new physics possibilities, for example new heavy gauge bosons (W', Z'), supersymmetric particles, large extra dimensions (via the Drell-Yan di-lepton spectrum), and Higgs bosons in extensions of the Standard Model such as the MSSM. These triggers also select particle decays involving τ's where the τ decays leptonically. The inclusive single- and di-photon triggers will select a light Higgs boson via its decay $H \to \gamma\gamma$ as well as some exotic signatures (e.g. technicolour).
The coverage for supersymmetry is extended by using the jet + missing-transverse-energy signatures as well as multi-jet selections; the multi-jet selection is especially relevant in case of R-parity violation. The inclusive single- and di-jet triggers will, for example, be used in the search for new resonances decaying into two jets. Further sensitivity to supersymmetry at large values of $tan\beta$ will be provided by signatures involving a hadronic τ selection. Rare b-hadron decays and b-hadron decays involving final states with a J/Ψ are selected by a di-muon signature (requiring opposite charges) and additional invariant-mass cuts.

3.6.6 HLT Selection Working Example

The following example illustrates the working principle of the HLT event selection software: the LVL1 trigger finds two isolated electromagnetic clusters with $p_T > 20 \, \mathrm{GeV}$ each. This is a possible signature for the decay $Z \to e^+e^-$ for which the ATLAS trigger must accepts the event, if both electrons are isolated and have a minimum p_T of $30 \, \mathrm{GeV}$. The HLT validates this hypothesis in a step-by-step process. Intermediate signatures are produced as result of the algorithmic processing of a given step, and each intermediate signature is examined in order to be able to reject the hypothesis at the earliest possible moment. This procedure is managed by the HLT Steering package. The validation procedure starts from the LVL1 RoI

Selection signature	Example of physics coverage
e25i	$W \to e\nu$, $Z \to ee$, top production, $H \to WW^{(*)}/ZZ^{(*)}$, W',Z'
2e25i	$Z \to ee$, $H \to WW^{(*)}/ZZ^{(*)}$
μ20i	$W \to \mu\nu$, $Z \to \mu\mu$, top production, $H \to WW^{(*)}/ZZ^{(*)}$, W',Z'
2μ20i	$Z \to \mu\mu$, $H \to WW^{(*)}/ZZ^{(*)}$
γ60i	direct photon production, $H \to \gamma\gamma$
2γ20i	$H \to \gamma\gamma$
j400	QCD, SUSY, new resonances
2j350	QCD, SUSY, new resonances
3j165	QCD, SUSY
4j110	QCD, SUSY
τ60i	charged Higgs
μ10 + e15i	$H \to WW^{(*)}/ZZ^{(*)}$, SUSY
τ35i + xE45	$qqH(\tau\tau)$, $W \to \tau\nu$, $Z \to \tau\tau$, SUSY at large $\tan\beta$
j70 + xE70	SUSY
xE200	new phenomena
E1000	new phenomena
jE1000	new phenomena
2μ6 + $\mu^+\mu^-$ + mass cuts	rare b-hadron decays ($B \to X$) and $B \to J/\Psi(\Psi')X$

Table 3.1: *Trigger menu, showing the inclusive physics triggers. The notation for the selection signatures is in the form 'NoXXi', where 'N' is the minimum number of objects required, and 'o' indicates the type of the selection ('e' for electron, 'γ' for photon, 'μ' for muon, 'τ' for a τ hadron, 'j' for jet, 'b' for a b-tagged jet, 'xE' for missing transverse energy, 'E' for total transverse energy, and 'jE' for the total transverse energy obtained using only jets). 'XX' gives the threshold in transverse energy (in units of GeV), and 'i' indicates an isolation requirement*

May 26, 2006

information as seed, as shown in Fig. 3.9. In this example, there are two isolated electromagnetic RoIs with $p_T > 20\,\text{GeV}$ ("EM20i" in Fig. 3.9).

The HLT Steering calls an HLT algorithm ("Cluster Shape") to determine the cluster shape of the first seed. The cluster shape is found to be consistent with the electron hypothesis and the result is an electron candidate ("ecand"). The HLT Steering proceeds in the same way with the second seed and obtains a second electron candidate. These two electron candidates are considered as an intermediate signature ("ecand + ecand"). Since the event after this first step is still compatible with the $Z \rightarrow e^+e^-$ signature, the HLT Steering starts the second step of the validation procedure. In this second step, the two electron candidates provide the seeds for the algorithmic processing. The HLT Steering calls a track finding HLT algorithm ("track finding") for each of the two electron candidates. If for each of the electron candidates a track pointing to them is found, this second step results in two electrons that constitute another intermediate signature ("e + e"). Using, in the manner described above, the output of one step of the validation procedure as input to the next, the HLT Steering calls the appropriate HLT algorithms in the appropriate sequence to verify that the two electrons each have $p_T > 30\,\text{GeV}$ and are both isolated. When finally, after the fourth step, the signature "e30i + e30i" has been reached, the ATLAS trigger accepts the event as a candidate for the decay $Z \rightarrow e^+e^-$ with the desired electron characteristics. To guarantee early rejection, the
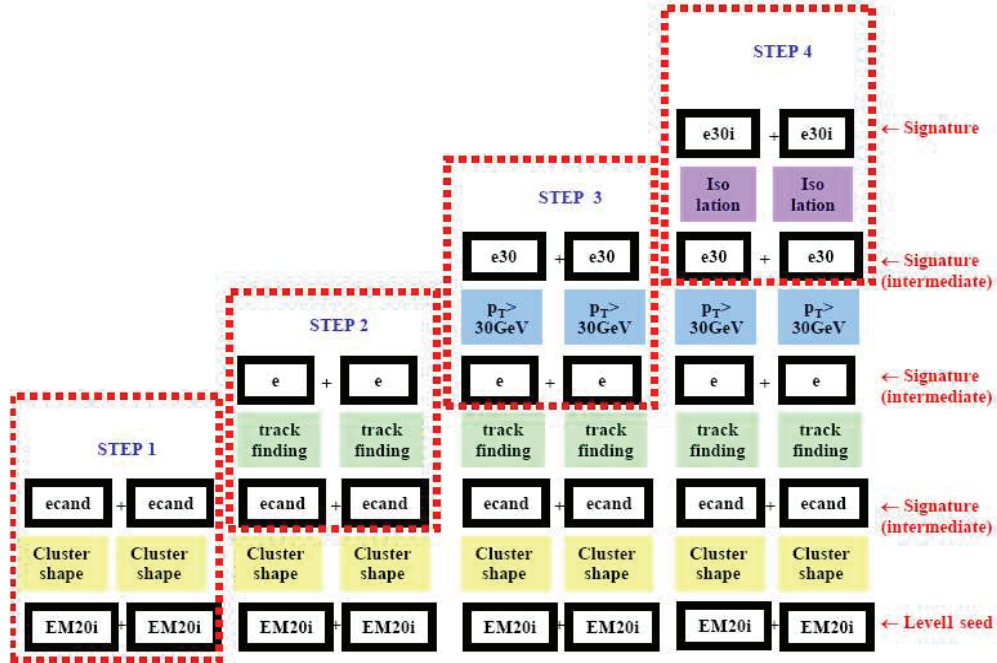
Figure 3.9: *Example illustrating the working principle of the HLT selection software. The different steps follow each other in time. Each step is shown with the complete processing chain preceding it. Hence for step 4, the full chain of processing steps is shown, with time increasing from bottom to top.*

HLT Steering can reject an event after any step during the validation procedure. If the first step in the example above had not resulted in two electron candidates with the appropriate cluster shapes, the HLT Steering would have stopped the validation of the specific Z decay signature under scrutiny without passing to step 2. Note also that the HLT processing is not organized vertically (carry out the full sequence of algorithms to arrive first at a reconstructed electron for the first RoI and only then do the same for the second) but horizontally (carry out only the reconstruction foreseen in step x for the first and then the second seed and use the output as seeds for the next step).

Bibliography

[1] ATLAS Collaboration, ATLAS High-Level Triggers, DAQ and DCS Technical Proposal, 2000. CERN/LHCC/200017

[2] H.J. Burckhart, ATLAS Detector Control System User Requirements Document, ATLAS internal note,PSS05-ATLAS-DCS-URD, 22 November 1995.

[3] ATLAS Collaboration, FirstLevel Trigger Technical Design Report, 1998. CERN/LHCC/9814

[4] ATLAS Collaboration, HighLevel Trigger Data Acquisition and Controls Technical Design Report, 2003. CERN/LHCC/2003022

[5] S. Armstrong et al., "An Implementation of Region-of-Interest Selection for ATLAS High Level Trigger and Offline Software Environments", ATLAS Internal Note, ATL-DAQ-2003-014 (2003)

[6] TheStoreGate: a Data Model for the Atlas Software Architecture, Proceedings CHEP03, LaJolla, California, March24-28, 2003.

[7] S. Goldfarb and A. Schaffer (editors), Definition of Offline Readout Identifiers for the ATLAS detector, ATLAS Internal Note ATLAS-SOFT-2001-004.

[8] The Algorithm Steering and Trigger Decision mechanism of the ATLAS High Level Trigger, Proceedings CHEP03, LaJolla, California, March24-28, 2003.

[9] M. Elsing et al., "Analysis and Conceptual Design of the HLT Selection Software", ATLAS Internal Note, ATL-DAQ-2002-013 (2002)

[10] Athena: User Guide and Tutorial, http://atlas.web.cern.ch/Atlas/GROUPS/SOFTWARE/O architecture/General/Tech.Doc/Manual/2.0.0-DRAFT/AthenaUserGuide.pdf

[11] ATLAS Collaboration, ATLAS Technical Proposal, 1994. CERN/LHCC/94-43

[12] L.Mapelli, Global architecture for the ATLAS DAQ and Trigger, ATLAS internal note, ATL-DAQ-95-022 (1995)

Chapter 4

Identification of High p_T Electrons by the HLT System of ATLAS

4.1   Introduction

The identification of isolated high transverse momentum electrons ($p_T \geq 25\,GeV/c$) is essential for physics studies at the LHC. Typical examples are the searches for decays of the Higgs boson into four electrons $H \to ZZ^{(*)} \to 4e$, with a cross section of $0.2\,fb$ for a Higgs mass of $130\,GeV/c^2$, the production of Z with decays $Z \to e^+e^-$ ($\sigma = 1.5\,nb$), or the production of W with decays $W \to e\nu$ ($\sigma = 15\,nb$). The QCD di-jet cross section being of the order of $10^{-6}\,nb$, to obtain an inclusive electron signal, a rejection factor 10^7 is required on QCD jets.

Two electron triggers are envisaged for ATLAS, the single, and the double-object electron triggers. The single-object electron trigger will typically have a threshold of $p_T = 30\,GeV$, require a LVL2 electron efficiency of $\epsilon_e \sim 90\%$ and a jet rejection of 100. This will be used, for example as an inclusive $t \to e\nu_e b$ trigger for top quark studies. The double-object electron trigger will be designed to trigger on two electrons with $p_T > 25\,GeV$, for processes such as Z and H boson decays. With two electrons in the event, the rejection requirements per fake electron are less severe, but the highest possible efficiency for real electrons is required.

Since the publication of previous electron trigger studies [1]- [4], the Monte Carlo description of the Inner Detector (ID) geometry has been significantly modified with the introduction of a more realistic material description, leading to important changes in performance. At the same time, the reconstruction software has moved to the object oriented framework Athena [5], and a new e/γ analysis framework [6] was created in order to serve as a common platform for future EM trigger performances studies.

This chapter presents a Monte Carlo study of the HLT single electron trigger performance and its rejection capability against QCD jets, using the electromagnetic and the hadronic calorimeter as well as the ID. Sections 3.2, and 3.3, gives technical details about the detector layout and datasets used in this study. The high p_T

electron trigger is detailed described in section 3.4. The validation of the LVL2 algorithms against their offline counterparts is presented in section 3.5. The HLT electron selection performance studies and results are shown in section 3.6 for low and design luminosity. Section 3.7 summarizes the results obtained and gives the final conclusions.

4.2 Luminosity Setups

All studies within ATLAS are made at two settings: one at the so-called design luminosity[1] of $10^{34}\,cm^{-2}\,s^{-1}$ and the other at low luminosity of $2 \times 10^{33}\,cm^{-2}\,s^{-1}$. At low luminosity there is an average of five interactions per bunch crossing. At design luminosity an average of 23 interactions is expected. In order to simulate this situation, minimum bias events were added to the event using the pile-up method documented in reference [11]. The number of minimum bias events is selected randomly using a Poisson distribution with an average of 23. In both settings, simulated electronic noise is added to the calorimeter without using a threshold. These two luminosities have to be understood as common settings to study the behavior of ATLAS. In the real experiment, the luminosities will change during a fill of the LHC. After a new fill of the LHC, the luminosity will be around the design luminosity and then drop for several hours to or even below the low luminosity setting. This implies, of course, that different parameter settings than those used in this study may have to be adopted.

4.3 Detector Layout and Data Samples

In this study a more up-to-date detector layout, referred to as the Data Challenge 1 (DC1) layout is used compared with earlier studies [8], [9]. Details on the changes are summarized in [1]. The main changes are the material distribution in the inner detector and a shift of the calorimeter end-caps by $4\,cm$. The inner detector now contains more material compared with the older layout, as can be observed in Fig.4.1.

Towards the end-cap, bremsstrahlung becomes even more pronounced, because electrons have to pass more material before arriving in the calorimeters. The material increase near the beam pipe is potentially more harmful because hard bremsstrahlung occurring in this region cannot be recovered. In the past the magnetic field in the inner detector cavity had been simulated to be $2\,T$ in the whole inner detector. In the simulations of the ATLAS detector used for the present study, the correct field map has been used. The magnetic field decreases from $B = 2\,T$ at $\eta \approx 0$ to $B \approx 1\,T$ at the end of the solenoid and to $B \approx 0.4\,T$ at $\eta \approx 2.5$. In the calorimeters the end-cap is moved outward by $4\,cm$ to leave more space to bring out

---

[1]In some publications the design luminosity is called high luminosity.
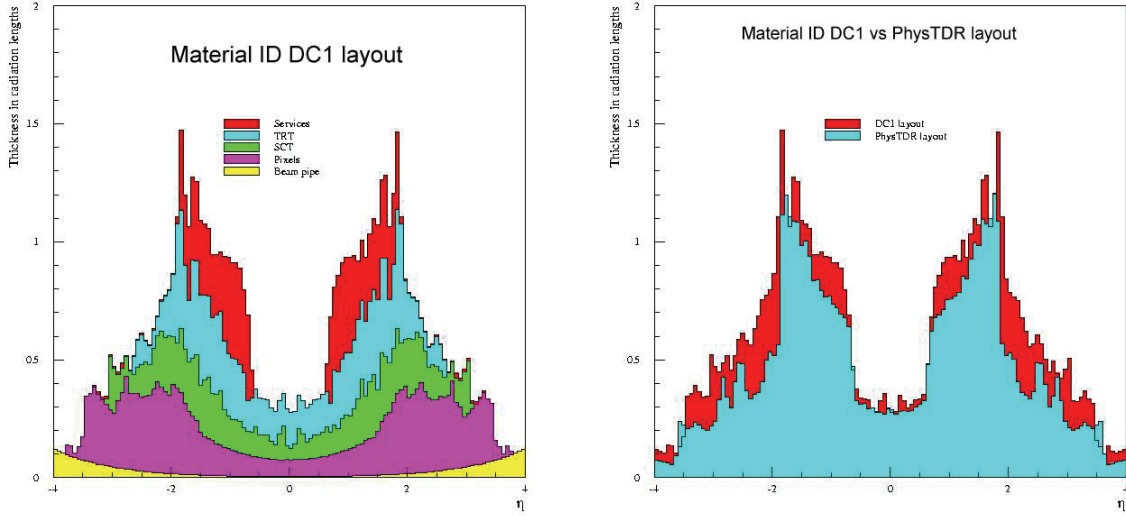
Figure 4.1: *Material distribution for the DC1 layout and comparison with the previous layout of the number of radiation lengths in the inner detector as a function of rapidity.*

cables in the crack between barrel and end-cap cryostat. This will mainly affect the shower shape variables which tend to be slightly broader than in the past.

Monte Carlo events are generated for DC1 with Pythia 6.203 [12] under the Athena framework and stored in Root format [13]. Monte Carlo events were simulated in the ATLAS detector with GEANT 3 [14].The input was the event kinematics from Root-format files and the output were the detector hits and digits in ZEBRA-format files. These DC1 data were reconstructed using Athena release 6.0.4. The electronic noise in the electromagnetic calorimeter is included. Pile-up is added to study these events for the low luminosity and design luminosity scenarios. The number of pile-up events per bunch crossing follows a Poisson distribution with an average of 4.6 (23) at low (design) luminosity.

To evaluate the performance of the electron identification algorithm, single electrons with pseudo-rapidity $|\eta| < 2.5$ and $E_T = 25\ (30)\ GeV$ at low (design) luminosity were generated. To evaluate the rejection factors, QCD dijet events, including initial and final state gluon radiation, are used. On parton level each jet is required to have a transverse momentum $p_T \geq 17\ (25)\ GeV/c$ and a rapidity within ± 2.7. Detailed information on the samples are given in Table 4.1.

In addition to QCD di-jet events, other physics processes such as prompt photon events or intermediate W/Z boson production were added (see Table 4.2). Events which would not pass the LVL1 are immediately rejected: at least one region of size $\Delta\eta \times \Delta\phi = 0.12 \times 0.12$ must be found, in which the summed transverse energy of all stable particles except muons and neutrinos is at least $17\ GeV$. Only 8.33% (10.20%) of all generated events at low (design) luminosity were accepted and then fully simulated. Hard Pythia processes cross-section (mb)

Data	luminosity	E_T	dataset	number of events
single electrons	low	$= 25$	002026	5000
dijets	low	≥ 17	002000	13750000
single electrons	design	$= 30$	002021	10000
dijets	design	≥ 25	002001	4416150

Table 4.1: *Data samples used, the nominal luminosity, the E_T threshold, the dataset number for DC1 production as well as the number of events is shown.*

Hard Process	Pythia processes	cross-section (mb)
$f_i f_j \rightarrow f_i f_j$	11	
$f_i \bar{f}_i \rightarrow f_j \bar{f}_j$	12	
$f_i \bar{f}_i \rightarrow gg$	13	
$f_i g \rightarrow f_i g$	28	1.5
$gg \rightarrow f_j \bar{f}_j$	53	
$gg \rightarrow gg$	68	
$f_i \bar{f}_i \rightarrow g\gamma$	14	3.0×10^{-4}
$f_i g \rightarrow f_i \gamma$	29	
$f_i \bar{f}_i \rightarrow Z^*/\gamma^*$	1	4.4×10^{-4}
$f_i \bar{f}_i \rightarrow W^\pm$	2	1.4×10^{-4}
$f_i \bar{f}_i \rightarrow t\bar{t}$	81	4.8×10^{-7}
$gg \rightarrow t\bar{t}$	82	

Table 4.2: *Cross sections of physics events simulated in di-jet sample 002000.*

4.4 Electron Trigger Selection

In order to garantee optimal acceptance to new physics within the current paradigm of particle physics, the ATLAS community has opted for an approach based on emphasizing the use of inclusive criteria for the on-line event selection, i.e. having signatures mostly based on single- and di-object high p_T triggers. In the case of electrons, high p_T translates on a transverse momentum above $O(15)\,GeV$. The choice of thresholds has to be made, if possible, in such a way that a good overlap with the reach of the Tevatron and other colliders is guaranteed, and there is good sensitivity to new light objects(e.g. Higgs bosons) while keeping the total output event rate down to $O(100)\,Hz$. Starting from the LVL1 result, the HLT electron identification is performed using a standard technique; electromagnetic clusters are selected, based on the transverse energy deposition in the calorimeters and shower-shape quantities that distinguish them from jets. Electron candidates are then selected by associating the e.m. clusters with a track in the Inner Detector.

Though not a part of the HLT system, it was considered appropriate to start this section with a brief description of the LVL1 algorithm for the selection of EM can-

didates, followed by an overview of the selection criteria used at the different HLT levels.

4.4.1 LEVEL 1 Electron Trigger Selection

The LVL1 calorimeter electron (and photon) trigger algorithm for the identification of EM candidates is well described in [15]; more details and a discussion of their hardware implementation can be found in [16].

The LVL1 algorithm works on matrices in $\eta \times \phi$, which store the E_T per trigger tower separately for EM and hadronic calorimeters with a typical granularity $\Delta\eta \times \Delta\phi = 0.1 \times 0.1$. Truncating the digitized values for the tower energies to eight bits effectively applies a $1\,GeV$ threshold to each trigger tower. The LVL1 electron trigger algorithm is based on a window of 4×4 towers in the electromagnetic and hadronic calorimeters in the region $|\eta| < 2.5$, and consists of four elements (see Figure 4.2):
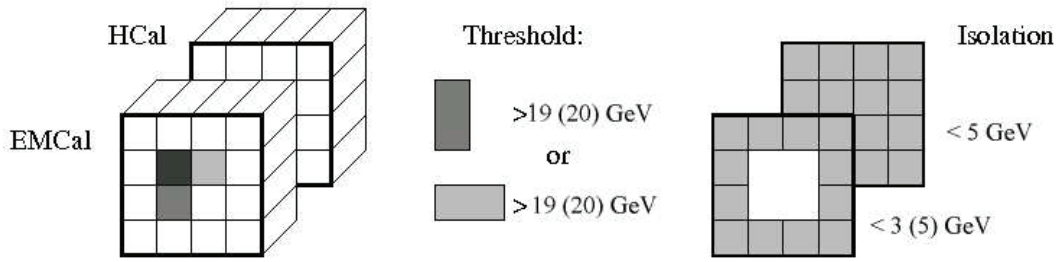
Figure 4.2: *Principle of LVL1 calorimeter electron trigger. The thresholds for low (design) luminosity are shown.*

- a 2×2-tower EM cluster used to identify the position of candidate RoIs (local ET maximum);

- a 2×1 or 1×2-tower e.m. cluster used to measure the E_T of e.m. showers. There are four such regions within the RoI cluster, and the most energetic of these is used;

- a ring of 12 electromagnetic towers surrounding the clusters which is used for isolation tests in the EM calorimeter;

- the 16 hadronic towers behind the electromagnetic clusters and isolation ring which are used for isolation tests in the hadronic calorimeters.

The window slides in steps of one trigger tower in both the η and ϕ directions. The LVL1 selections, which were used for this study, are listed in Table 4.3.

For each LVL1 trigger, RoI information is transmitted to the LVL2 trigger giving the (η, ϕ) position and E_T range of identified objects. Due to the choice of the local E_T maximum and the step size of 0.1, the RoI position is provided with a resolution of $\Delta\eta \times \Delta\phi \sim 0.1 \times 0.1$.

	Low Luminosity	Design Luminosity
E_T	$> 19\,GeV$	$> 20\,GeV$
EM ring isolation	$< 3\,GeV$	$< 5\,GeV$
Hadronic ring isolation	$< 2\,GeV$	$< 3\,GeV$
Hadronic core isolation	$< 2\,GeV$	$< 2\,GeV$

Table 4.3: List of trigger thresholds applied at LVL1 to select EM candidates: The EM cluster transverse energy, the EM and hadronic transverse isolation energy

4.4.2 LEVEL 2 Electron Trigger Selection

The Level 2 (LVL2) trigger provides the next stage of event selection after the hardware-based LVL1 trigger. It uses geometry information (η, and φ) of the trigger object identified by the LVL1 Region of Interest (RoI) to seed the validation and enhancement of the LVL1 trigger using selected full granularity event data.

4.4.2.1 LVL2 Algorithms

This section gives a brief overview of the main LVL2 algorithms used for the identification of electrons. The following list is non-exhaustive and includes only the algorithms that, by the time this work was done, were in a more advanced state of development. A complete overview of all the LVL2 electron trigger algorithms available can be found in [7].

- T2Calo: T2Calo [17] is a clustering algorithm for electromagnetic EM showers, seeded by the LVL1 EM trigger RoI positions. This algorithm can select isolated EM objects from jets using the cluster E_T and shower-shape quantities. The first step in T2Calo is to refine the LVL1 position from the cell with highest energy in the second sampling of the EM calorimeter. This position (η_1, ϕ_1) is later refined in the second sampling by calculating the energy-weighted-average position (η_c, ϕ_c) in a window of 3×7 cells (in $\eta \times \phi$) centered around (η_1, ϕ_1), using as weights the energy in the second sampling.

- IDScan: IDSCAN is a track reconstruction package for LVL2 [7][39]. It takes as input Space Points found in the Pixel and SCT Detectors. A series of sub algorithms (ZFinder, HitFilter, GroupCleaner, TrackFitter) then processes these and outputs Tracks and the Space Points associated with them.
The ZFinder determines the z-position of the primary interaction vertex. The algorithm puts all hits into narrow ϕ-bins and extrapolates pairs of hits in each bin back to the beam line, at a point z of closest approach, storing the value of z in a separate histogram. It takes as the z-position of the vertex, the histogram pair with most entries.
The HitFilter finds groups of hits compatible with track signature from the z

position found by ZFinder. It puts all hits into a histogram binned in η and ϕ. It then finds clusters of hits within this histogram. It creates a group of hits if such a cluster has hits in more than a minimum number of layers.

The group of hits found by HitFilter is used by GroupCleaner which splits groups into Tracks and removes noise hits from groups. Each triplet of hits forms a potential track for which p_T, ϕ_0, and d_0 are calculated. It forms groups of triplets with similar parameters, applying quality cuts. It accepts a track candidate if a group contains enough hits.

Finally, the TrackFitter verifies track candidates and finds the track parameters by using a standard Kalman-filter-type fitting algorithm adapted from SCTKalman [19]. It returns a list of SpacePoints on the Track, the Track parameters, and an error matrix.

4.4.2.2 LVL2 Calorimeter-based Electron Selection

The following variables are found to be most efficient in preserving the signal while efficiently rejecting the background. Care was taken to use quantities that are approximately independent of each other. Though the shape parameters are correlated for the signal because of the well defined shape of an EM shower, the correlations are much smaller for the background, where fluctuations are large.

– Transverse Energy in the EM Calorimeter: Owing to the energy dependence of the QCD background, a cut on E_T provides the best rejection against LVL1 triggered jets for a given high p_T signal process. The transverse energy E_T is calculated by using the EM calorimeter over 3×7 cells in η and ϕ. The E_T distributions are shown in Fig. 4.3 for $E_T = 25\,GeV$ ($30\,GeV$) electrons and jets at low (design) luminosity after the LVL1 trigger and before any other cuts. As can be observed, the number of background events is much reduced at lower E_T because the jet sample was generated with $p_T^{parton} > 17\,GeV$ and because the LVL1 energy thresholds reject low-energy jets.

– Transverse Energy in the Hadronic Calorimeter Electrons typically deposit very little of their energy in the hadronic calorimeter. For Level 1 EM triggered jets, however, about 5% of the energy is deposited there, and therefore this quantity can be used to tag jets, as can be seen in Fig 4.4. The EM energy that leaks from genuine e/γ clusters into the hadronic calorimeter increases with the incident e/γ energy; for low energy it is not significant when compared with the contributions from noise and pile-up. To be efficient for e/γ clusters at high E_T, however, the hadronic isolation requirement must be taken into account. In that sense, the energy dependence has been implemented as a series of E_T thresholds (see Table 4.4).

– Lateral Shape in the Second Sampling Electron showers have on average a lateral size of one Molière radius, whereas the lateral size of showers initiated
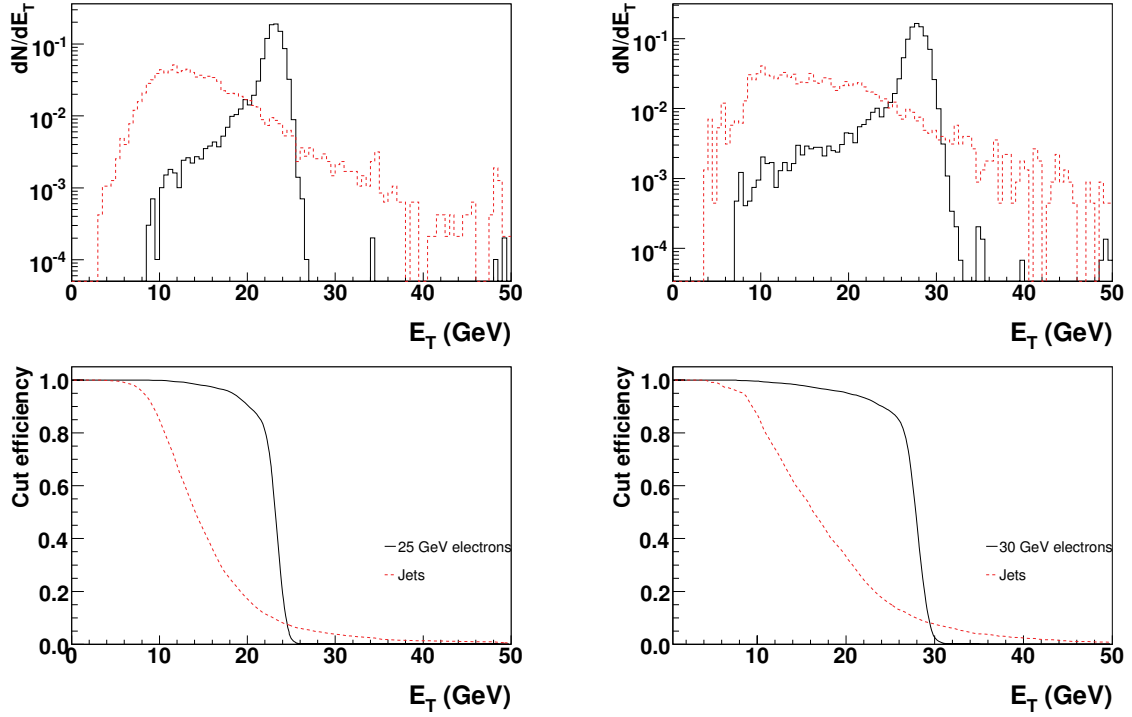
Figure 4.3: *Transverse energy E_T distribution for QCD di-jets (dotted line) and single electrons (solid line) at low (left column), and design right column luminosity after the LVL1 trigger. The lowest plot shows the signal and background efficiency as a function of the LVL2 trigger E_T threshold.*

by jets is dominated by fragmentation and the hadronic interaction length. Most of the energy of EM showers(typically more than 70%) is deposited in the second sampling of the EM calorimeter. This sampling is therefore also relatively less affected by noise and pile-up. Thus, in order to distinguish between e/γ clusters and jets, the quantity $R_\eta^{shape} = E_{3\times7}/E_{7\times7}$, the ratio of the cell energies contained in a $\Delta\eta \times \Delta\phi = 3 \times 7$ cell window to that in a 7×7 cell window was calculated in the second sampling of the EM calorimeter. As for E_T, a wider window in $\Delta\Phi$ allows for electron radiation, so that most of its energy is well-contained. The ratio R_η^{shape} is typically larger than 0.9 for EM clusters, as shown for $25\,GeV$ ($30\,GeV$) electrons and jets at low (design) luminosity in fig 4.5.

– Lateral Shape in the First Sampling After applying the cuts in the hadronic calorimeter and the second sampling of the EM calorimeter, only jets with very little hadronic activity and narrow showers in the calorimeter remain. These 'electromagnetic' jets frequently consist of single or multiple π^0s or η's decaying to two photons. In order to reject these jets the very fine granularity of the first sampling of the EM calorimeter can be exploited by looking for substructures and by analyzing the shower shape. To that effect, the quantity $R_\eta^{strips} = \frac{E_1-E_2}{E_1+E_2}$, the fractional difference in energy between the first sampling
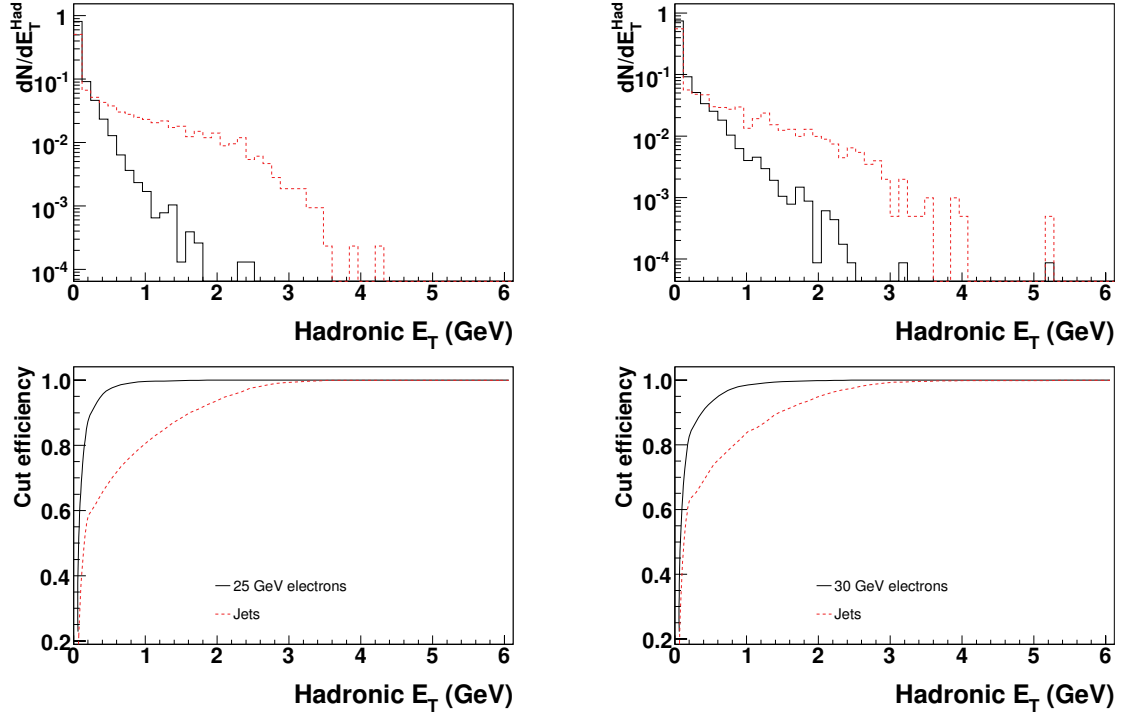
Figure 4.4: Transverse energy distribution in the hadronic calorimeter for QCD di-jets (dotted line) and single electrons (solid line) at low (left column), and design right column luminosity after the LVL1 trigger. The lowest plot shows the signal and background efficiency as a function of the LVL2 trigger E_T threshold.

cell with the maximum energy, E_1, and the second maximum energy, E_2, in the first sampling of the electromagnetic calorimeter is calculated. Figures 4.6 show this quantity for $25\,GeV$ ($30\,GeV$) electrons and jets at low (design) luminosity.The selection using this lateral shape quantity is a powerful tool to reject photons that originated from π^0s or η's.

E_T (GeV)	E_T^{Had} (GeV)		R_η^{shape}	R_η^{strips}
>	<	<	>	>
	if $25 < E_T \le 60\,GeV$	if $E_T > 60\,GeV$		
Low Luminosity				
22.5	1.0	2.0	0.9	0.72
Design Luminosity				
22.5	2.2	4.0	0.9	0.75

Table 4.4: *Cuts applied in the LVL2 calorimeter variables as a function of η. The crack region in the EM calorimeter between $1.37 < |\eta| < 1.52$ was excluded from the analysis. This values are for $25\,GeV$ ($30\,GeV$) electrons at low (design) luminosity.*
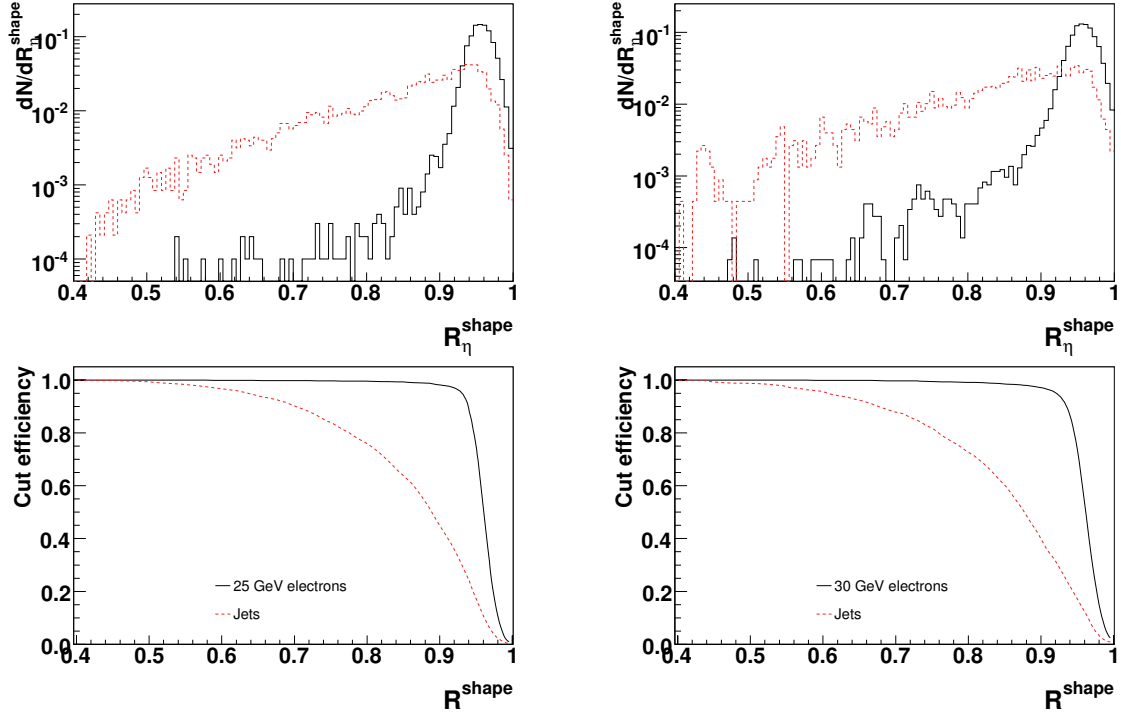
Figure 4.5: *Distribution of R_η^{shape} for QCD di-jets (dotted line) and single electrons (solid line) at low (left column), and design right column luminosity after the LVL1 trigger. The lowest plot shows the signal and background efficiency as a function of the LVL2 trigger E_T threshold.*

4.4.2.3 LVL2 Tracking and Track-Calo Matching Electron Selection

After the calorimeter based cuts, the remaining background is typically dominated by photon conversions and low multiplicity jets containing high-p_T π^0 mesons. A cut applied to the track transverse momentum p_T can be used then to reduce the number of candidates whilst maintaining good efficiency, since for these events, the p_T distribution is peaked toward low values.

Track to cluster matching cuts are used to discriminate RoI where the the EM cluster is due to an electron or converted photon, from those in which the cluster is due to a γ or a charged or neutral hadron. The following variables are used in this study:

– **$\Delta\eta$, and $\Delta\Phi$:** The difference in pseudo-rapidity and ϕ angle between the cluster position and the position of the extrapolated track from the SCT+pixel system offer additional discrimination against jets, since in these events, the calorimeter cluster is often due to the energy deposition from a photon or from more than one particle and hence does not match well in position with the parameters of any inner detector track. Figure 4.7 shows the $\Delta\eta$, and $\Delta\Phi$ distributions for electrons and QCD-dijets. As can be observed, the $\Delta\phi$ distribution is significantly narrower for electrons than for tracks in jet events.
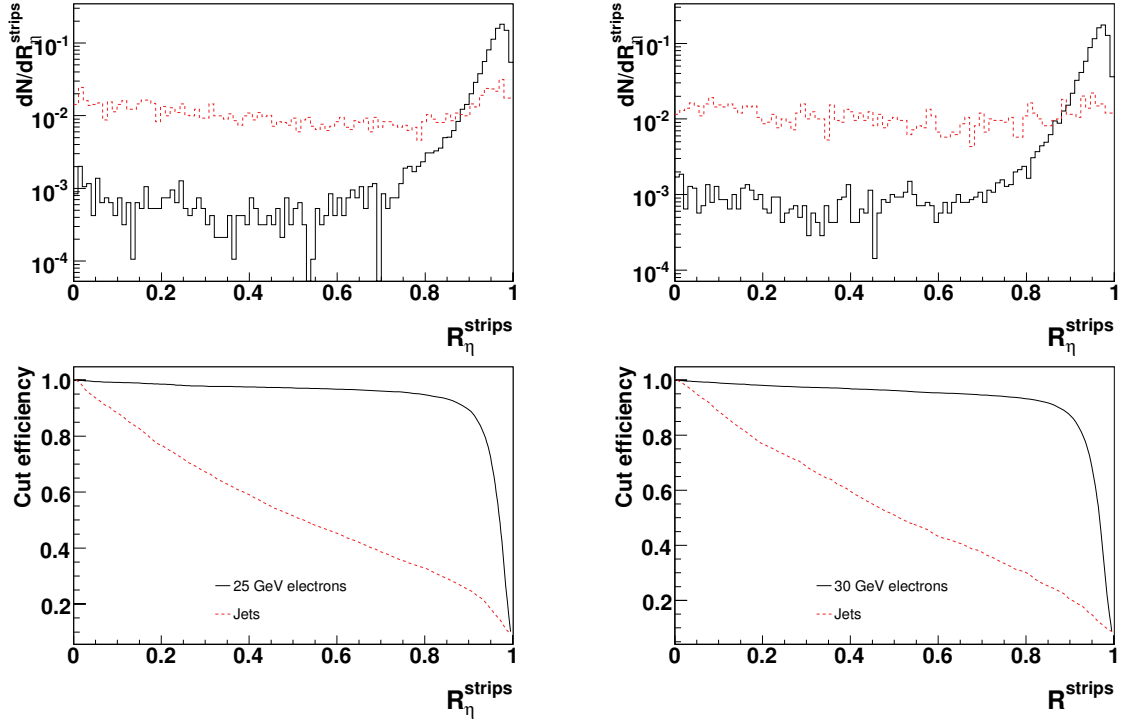
Figure 4.6: *Distribution of R_η^{strips} for QCD di-jets (dotted line) and single electrons (solid line) at low (left column), and design right column luminosity after the LVL1 trigger. The lowest plot shows the signal and background efficiency as a function of the LVL2 trigger E_T threshold.*

- $\boldsymbol{E_T/p_T}$ Further discrimination of electrons from jets can be obtained by comparing the transverse energy of the EM cluster, E_T, with the p_T of the inner detector track. The effect of Bremsstrahlung is to reduce the p_T of the particle and consequently the measured p_T. The EM cluster on the other hand frequently contains contributions from both the electron and the Bremsstrahlung photons, and therefore it measures more closely the initial E_T of the particle. As a result, the distribution of E_T/p_T has a tail toward high values. Despite the effects of Bremsstrahlung, there are proportionally more events in the tail of the E_T/p_T distribution for jets and thus a cut to reject high values of this quantity provides extra discrimination against jets. E_T/p_T distributions for both $25\,GeV$ $(30\,GeV)$ electrons, and di-jet events are shown in Figure 4.10.

4.4.3 Event Filter Electron Trigger Selection

In the Event Filter (EF), electrons are selected with a strategy very similar to that for LVL2, using information from the calorimeters and the Inner Detector. The main differences with respect to LVL2 arise from the availability of calibration data and the possibility to use more sophisticated reconstruction algorithms with access to the detector data for the full event. This results in sharper thresholds and better background rejection. In order to avoid biases introduced by using different
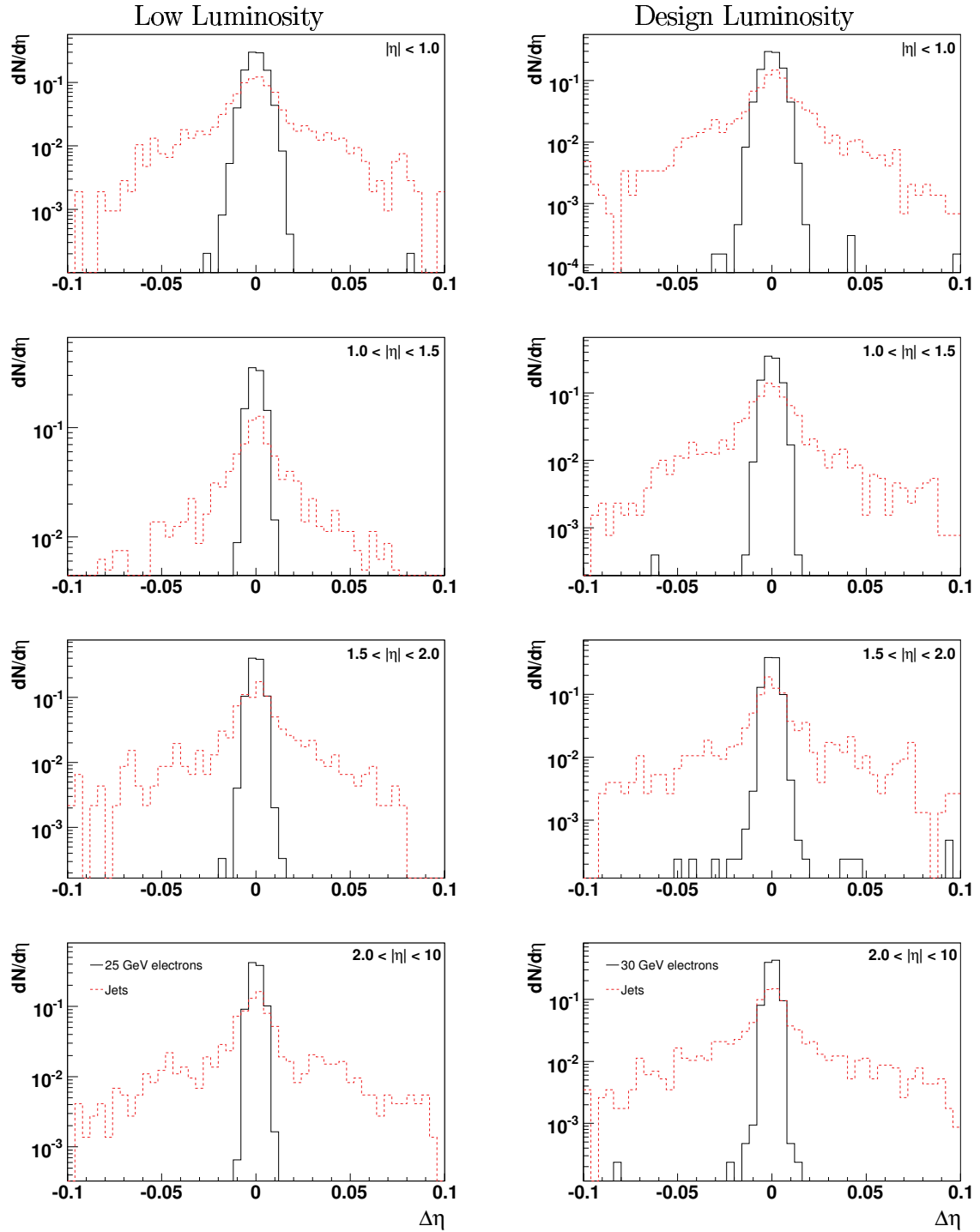
Figure 4.7: *LVL2 distribution of $\Delta\eta$ between the extrapolated track and the calorimeter cluster position for 4 different $|\eta|$ regions at low luminosity (left column), single $p_T = 25\,GeV$ electrons (solid line), and jet events (dotted line), and at design luminosity (right column) single $p_T = 30\,GeV$ electrons (solid line), and jet events (dotted line).*
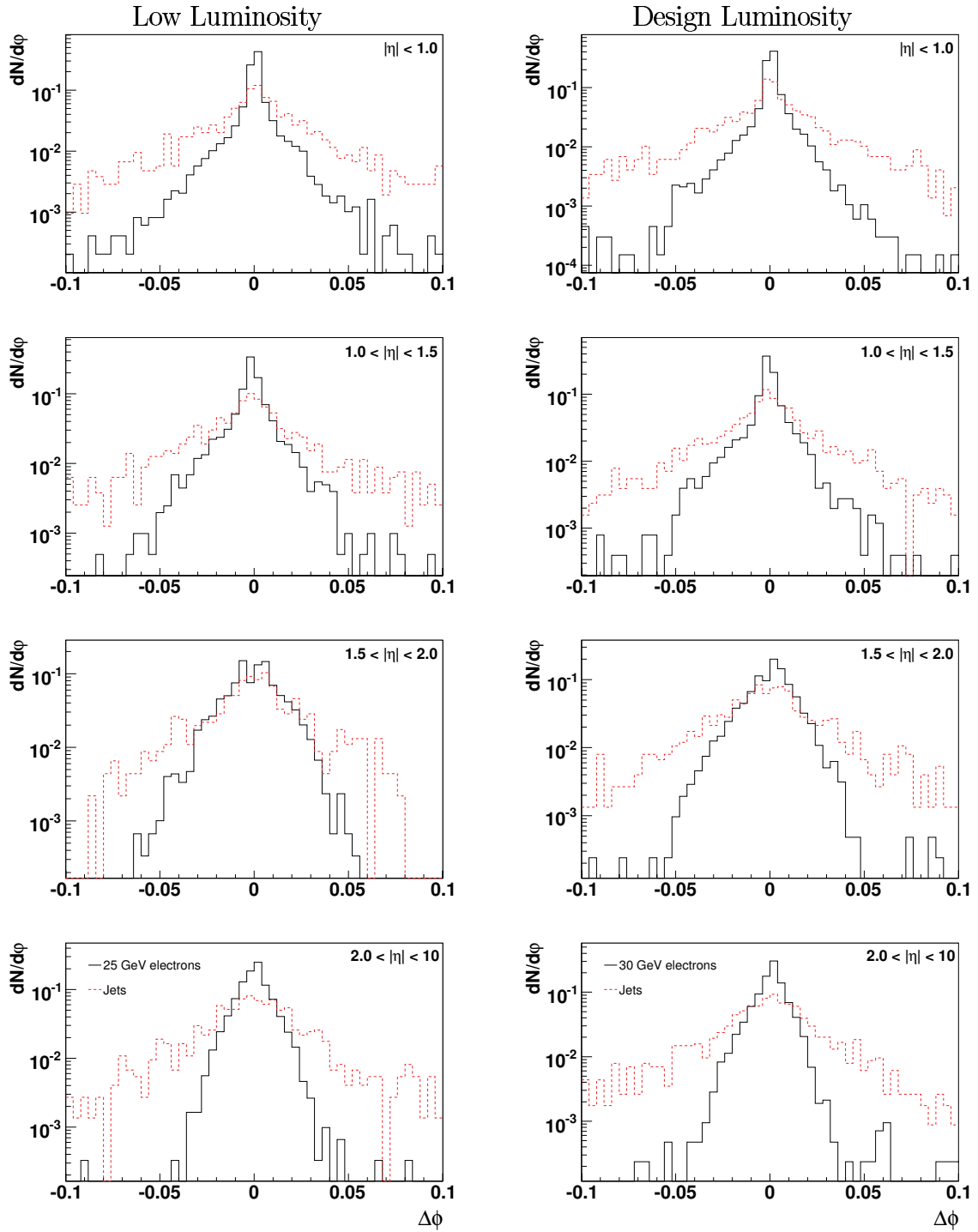
Figure 4.8: *LVL2 distribution of $\Delta\phi$ between the extrapolated track and the calorimeter cluster position for 4 different $|\eta|$ regions at low luminosity (left column), single $p_T = 25\,GeV$ electrons (solid line), and jet events (dotted line), and at design luminosity (right column) single $p_T = 30\,GeV$ electrons (solid line), and jet events (dotted line).*

reconstruction algorithms for online and offline selection, the EF will select events using as far as possible the offline reconstruction algorithms.

The present study uses the currently available ATLAS offline reconstruction software
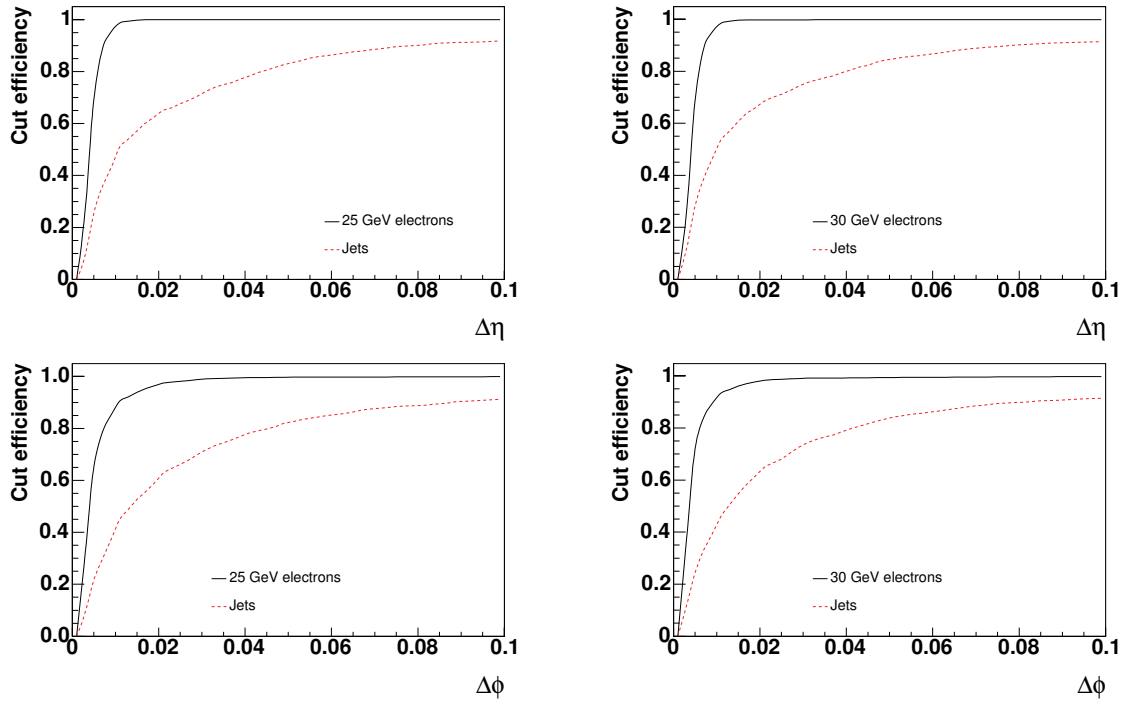
Figure 4.9: *Signal (solid line) and background efficiency (dotted line) as a function of the $|\Delta\eta|$ (upper row) and $\Delta\phi$ cut values (bottom row) between the extrapolated precision track and the calorimeter cluster position, for low luminosity (left column) and design luminosity (right column) after the LVL1 trigger. Distributions are for events in the central region $|\eta| < 1.0$.*

	$\Delta\eta$	$\Delta\phi$	E_T/p_T	
	$<$	$<$	$>$	$<$
Low Luminosity				
$0 < |\eta| \leq 1.0$	0.007	0.035	0.2	3.0
$1.0 < |\eta| \leq 1.52$	0.06	0.035	0.2	3.0
$1.52 < |\eta| \leq 2.0$	0.05	0.030	0.2	3.0
$2.0 < |\eta| \leq 10.0$	0.05	0.025	0.2	3.5
Design Luminosity				
$0.0 < |\eta| \leq 1.0$	0.05	0.05	0.2	4.0
$1.0 < |\eta| \leq 1.52$	0.05	0.05	0.2	4.0
$1.52 < |\eta| \leq 2.0$	0.05	0.05	0.2	5.0
$2.0 < |\eta| \leq 10.0$	0.05	0.05	0.2	7.0

Table 4.5: *Cuts applied in the LVL2 ID/calorimetric matching variables as a function of η. The crack region in the EM calorimeter between $1.37 < |\eta| < 1.52$ was excluded from the analysis. This values are for $25\,GeV$ ($30\,GeV$) electrons at low (design) luminosity.*

(see Section 13.3.4) as a prototype of the future EF code. The criteria used to identify electrons and photons need to be softer in the EF than in the offline in
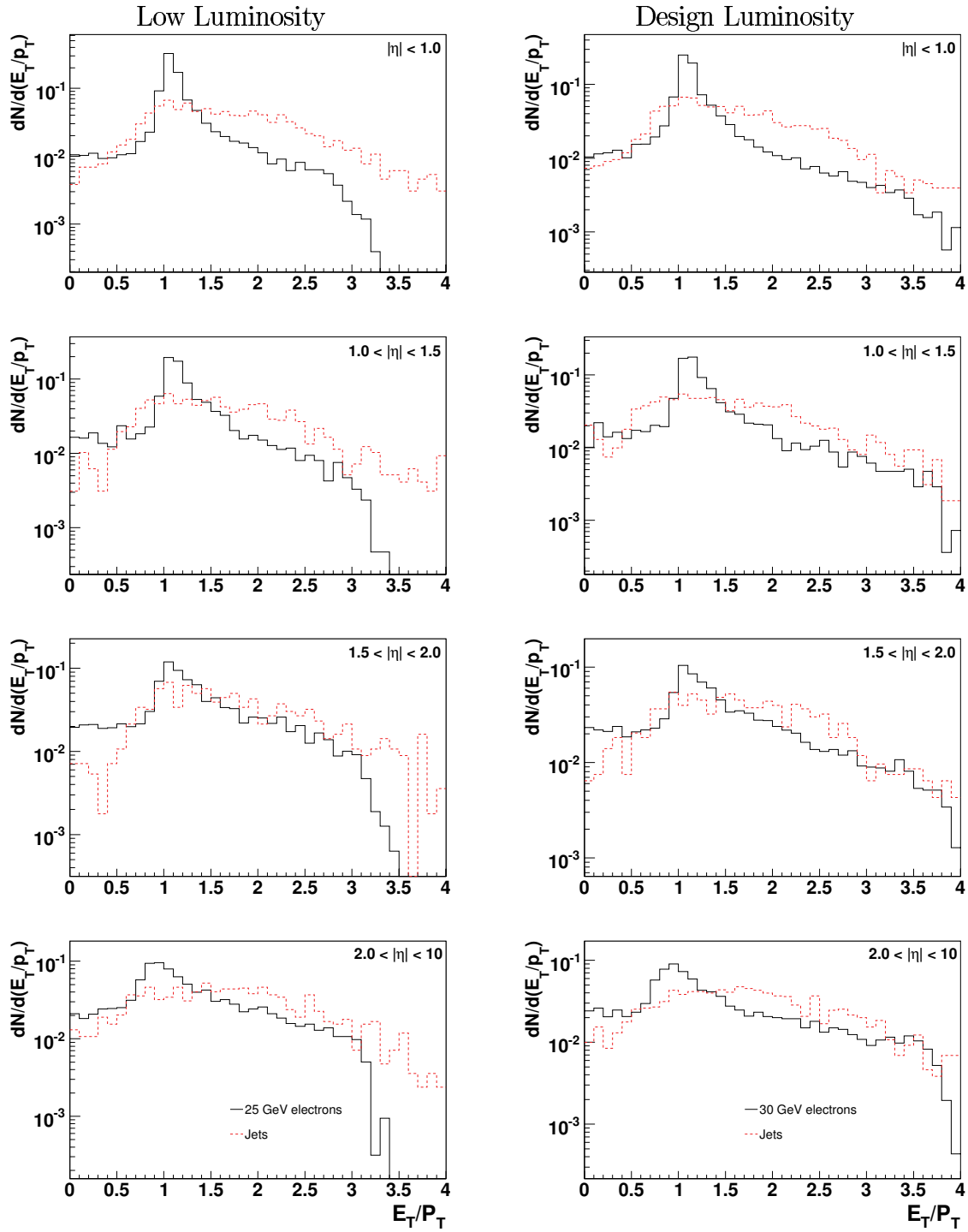
Figure 4.10: *LVL2 distribution of the ratio E_T of the calorimeter cluster to the p_T of the track reconstructed in the ID for 4 different $|\eta|$ regions at low luminosity (left column), single $p_T = 25\,GeV$ electrons (solid line), and jet events (dotted line), and at design luminosity (right column) single $p_T = 30\,GeV$ electrons (solid line), and jet events (dotted line).*

order not to lose events prematurely. In previous EF studies (see Refs. [21] and [22]) the electron selections used the same cuts as in the offline selection, but did
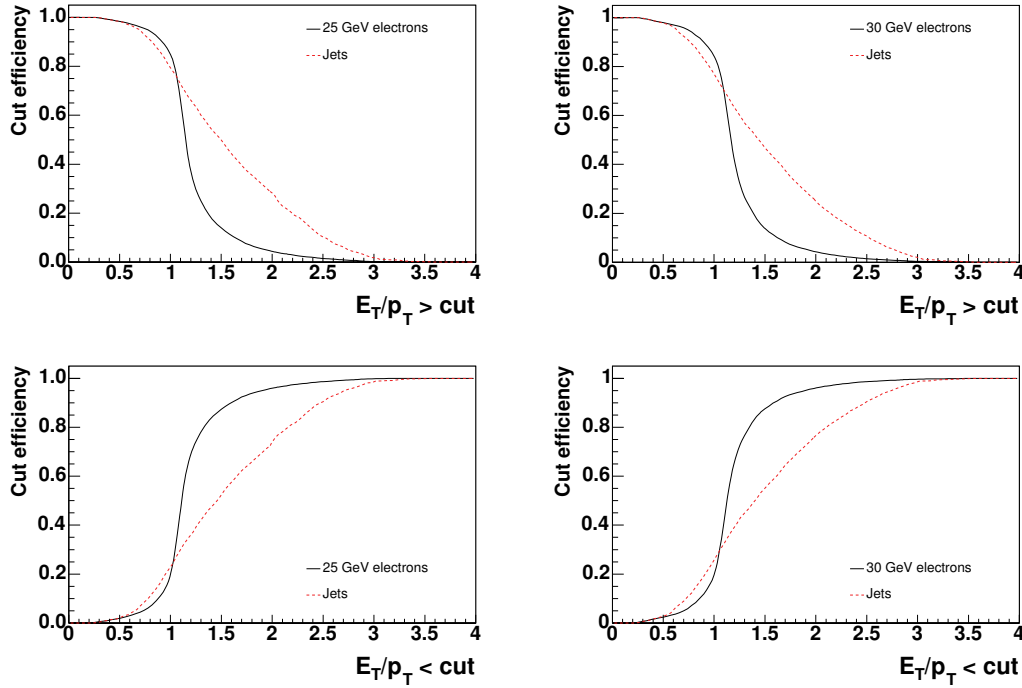
Figure 4.11: *Signal (solid line) and background efficiency (dotted line) as a function of the cut value to reject low E_T/p_T values (upper row) and high E_T/p_T values (bottom row), for low luminosity (left column) and design luminosity (right column) after the LVL1 trigger. Distributions are for events in the central region $|\eta| < 1.0$.*

not use 'critical' criteria, as for example, a track veto for non-converted photons. In addition, The TRT information is used to improve the final identification of electrons, therefore a more realistic EF electron selection has been used for the study presented here.

4.4.3.1 Event Filter Algorithms

The baseline option for the selection at the EF stage is to adopt algorithms from the offline suite. This will allow the on-line selection to easily benefit from the improvements stemming from offline analysis and to avoid duplication of efforts. In the following, a brief description of the algorithms used for this study is given.

- xKalman++: xKalman++ is a package for global pattern recognition and track fitting in the Inner Detector for charged tracks with transverse momentum above $0.5\,GeV$. A more detailed description of this algorithm is available in [20].
  The algorithm starts the track reconstruction either in the TRT, using a histogram method, or in the Pixel and SCT detector layers using a segment search.
  The TRT reconstruction method outputs a set of possible track-candidate trajectories defined as an initial helix with a set of parameters and a covariance

matrix. As a second step the helix is then used to define a track road through the precision layers, where all the measured clusters are collected. xKalman++ attempts to find all possible helix trajectories within the initial road and with a sufficient number of clusters.

The other method, where track finding starts in the Pixels or SCT, outputs a set of Space Points as an initial trajectory estimate. In the next step, the Space Points serve as input for the Kalman filter-smoother formalism that will add the information from the remaining precision layers. Each reconstructed Track is then extrapolated into the TRT, where a narrow road can be defined around the extrapolation result. All TRT Clusters together with the drift-time hits found within this road are then included for the final track-finding and track-fitting steps.

There are three seeding mechanisms available in the offline environment: the reconstruction of the full event; the reconstruction of a region-of-interest; and EM calorimeter seeding. In the HLT environment, used as an EF algorithm, xKalman++ will be seeded by the LVL2 result.

After the pattern-recognition and Track-fitting steps, xKalman++ stores the final track candidates with the following information:

- fit procedure used;

- helix parameters and their covariance matrix at the end-points of the filter procedure in the precision layers (point on the trajectory closest to the vertex) and in the TRT (point on the trajectory closest to calorimeter);

- total χ^2 resulting from final fit procedure;

- transverse momentum p_T of the reconstructed tracks;

- list of all hits on track from all sub-detectors;

- total number of precision hits Np;

- total number of TRT straw hits N_s, empty straws crossed N_e, and of drift-time hits N_t.

- EgammaRec: EgammaRec is an algorithm designed to calculate quantities that can be used to separate electrons and photons from jets. To do so, EM cluster and tracking information are used.

  In the electromagnetic calorimeter electrons are narrow objects, while jets tend to have a broader profile. Hence, shower shapes variables can be used to reject jets. This is handled by the EMShowerBuilder which calls a set of algorithms that calculates them using information from the first and second samplings of the electromagnetic calorimeter, as well as the first sampling of the hadronic calorimeter.

  Cluster and track information are combined in the EMTrackMatchBuilder. For a given cluster all tracks are examined in a window around the cluster

position. In case more than one track is found, the one with the highest p_T is retained. If the E/p ratio is within a specific range, the track match is successful. In the subsequent particle-identification step the information provided by egammaRec can be used. In case of an electron hypothesis, jets can be rejected by analysis of the EM shower shape, tight track-quality cuts, E/p matching, and the position match in η and ϕ directions between the Cluster and the Track.

4.4.3.2 Event Filter Calorimeter-based Electron Selection

Due to the similarities between some of the electron selection criteria used at LVL2 and the EF level, special emphasis will be put only in those variables which have not been previously defined.

– Transverse Energy in the EM Calorimeter: Significant discrimination between electrons and jets can be achieved by the LVL2 calorimeter trigger. Subsequently, the EF calorimeter algorithms can refine the cuts applied at previous levels as well as making additional ones.
For this study, only EM clusters with $E_T > 22$ (27) GeV at low (design) luminosity were considered. These values correspond to the E_T threshold cut of the single-object electron trigger, which are chosen to be efficient for 25 (30) GeV electrons.

– Leakage in the Hadronic Calorimeter: Electromagnetic showers deposit a small amount of energy in the hadronic calorimeter, typically less than 2% for electrons, either due to their low energy, as in this study, or because of the presence of the cryostat wall for more energetic electrons. The hadronic leakage is defined as the ratio of the transverse energy reconstructed in the first compartment of the hadronic calorimeter in a window $\Delta\eta \times \Delta\phi = 0.2 \times 0.2$ to the transverse energy reconstructed in the electromagnetic calorimeter. This ratio is shown in Figure 4.12 for electrons and jets at low and design luminosity.

– Use of the Second Sampling of the EM Calorimeter: Electrons deposit most of their energy in a $\Delta\eta \times \Delta\phi = 3 \times 7$ window (in unit of cells), whereas the energy deposit profile of EM showers initiated by jets is usually wider. This feature can be exploited in order to separate electrons from jets. The following variables are used:

  – The lateral shower shape R_{shape} (already employed at LVL2), is given by the ratio of the energy reconstructed in a 3×7 cluster by the energy in a 7×7 cluster.

  – The lateral width ω_η^2, calculated in a window of 3×5 cells using the energy weighted sum over all cells, which depends on the energy impact
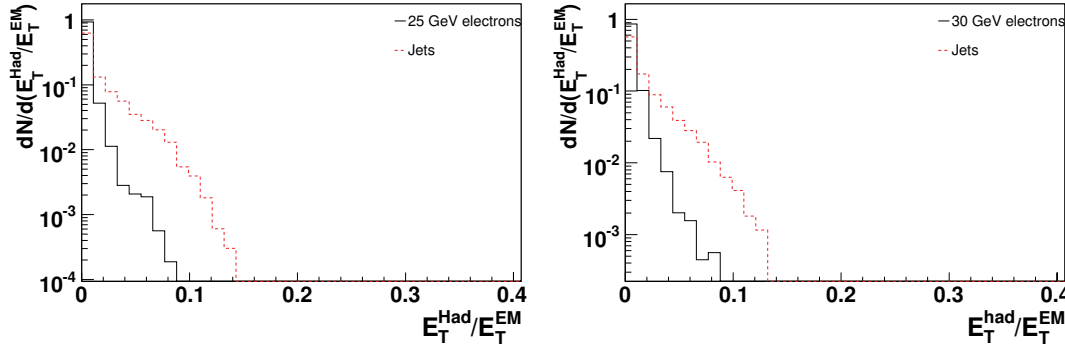
Figure 4.12: *Ratio of the transverse energy reconstructed in the first sampling of the hadronic calorimeter to the transverse energy in the EM calorimeter. The distributions are shown for low (left) and design (right) luminosity, and only the LVL1 trigger was applied beforehand.*

point inside the cell:

$$\omega_\eta^2 = \sqrt{\frac{\sum E_c \times \eta^2}{\sum E_c} - \left(\frac{\sum E_c \times \eta}{\sum E_c}\right)^2} \tag{4.1}$$
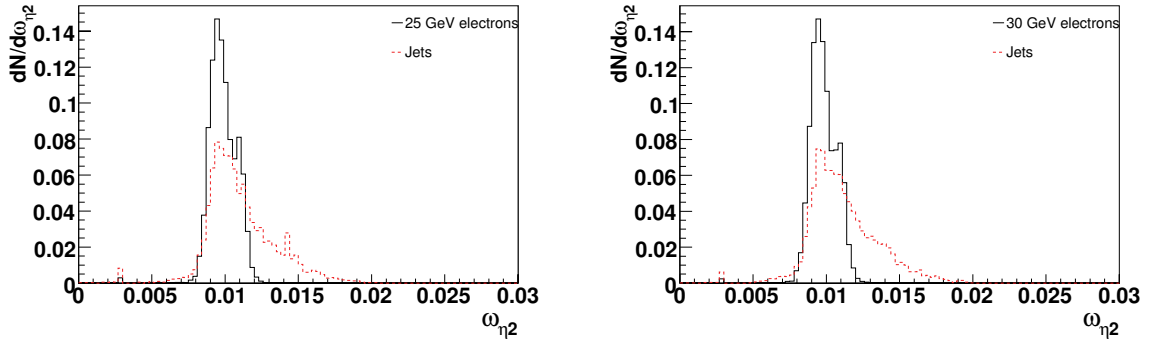
Figure 4.13: *Lateral width in the second sampling. Distributions are shown for low (left), and design (right luminosities).*

– Use of the First Sampling of the EM Calorimeter: Cuts applied on the variables used in the hadronic calorimeter and the second sampling of the electromagnetic calorimeters reject jets with high energetic pions and wide shower; jets with single or multiple γ, π^0 etc., are now the main contribution which can fake the electrons. The first compartment with its very fine granularity in rapidity can be used to detect substructures within a shower and thus isolated π^0's and γ's can be discriminated against efficiently. The lateral shower shape in the strips is exploited when a minimal amount of energy (0.5%) is reconstructed in the strips and for $|\eta| < 2.35$, where the strips granularity is fine enough. For all first compartment criteria, two cells in ϕ are summed.

Jets with π^0 decays are found to have often two maxima. The shower is studied in a window $\Delta\eta \times \Delta\phi = 0.125 \times 0.2$ (cf. Fig. 4) around the hottest cell to look for a second maximum. If more than two maxima are found the second highest maximum is chosen. Two variables are used (see Figure 4.14):

- the difference $\Delta E = E_{max2} - E_{min}$ of the energy associated with the second maximum E_{max2} and the energy reconstructed in the strip with the minimal value between the first and second maximum E_{min}.

- $\Delta E_{max2} = E_{max2}/(1 + 9(5) \times 10^{-3}E_T)$, with E_T the transverse energy of the cluster in the electromagnetic calorimeter and the constant value $9(5)$ refers to low (design) luminosity. To ensure not to be sensitive to fluctuations, the value of the second maximal energy deposit has to be greater than a threshold which depends linearly on the transverse energy.
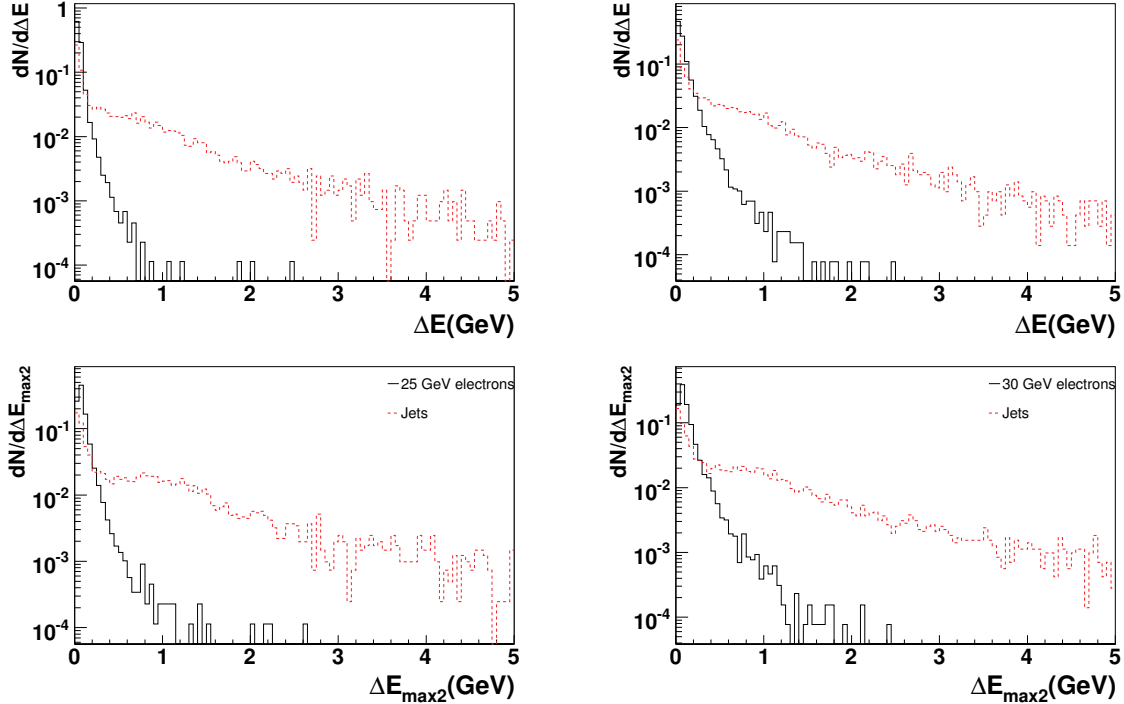
Figure 4.14: *Difference ΔE of the energy of the second maximum E_{max2} and the energy reconstructed in the strip with the minimal value between the first and second maximum (E_{min}) for low (left) and design (right) luminosity. ΔE_{max2} for low (left) and design (right) luminosity . The distributions are shown for jets (dotted lines) and electrons (solid line). Only the LVL1 trigger is applied beforehand.*

The total shower width is determined in a window $\Delta\eta \times \Delta\phi = 0.0625 \times 0.2$, corresponding typically to 40 strips in η. It is calculated using the following variable:

- $\omega_{tot1} = \sqrt{\sum E_i \times (i - i_{max})^2 / \sum E_i}$: where i is the strip number and

May 26, 2006

i_max the strip number of the first local maximum. This width is shown for electrons and jets at low and design luminosity in Fig.4.15.

After these cuts only very narrow showers with one reconstructed maximum remain. The two following variables are used for a fine study of the shower shape:

- F_{side} giving the shower shape in the shower core is shown in Fig.4.15. It is calculated with the following expression: $F_{side} = [E(\pm 3) - E(\pm 1)] = E(\pm 1)$, where $E(\pm n)$ is the energy in $\pm n$ strips around the strip with highest energy.

- The shower width using three strips around the one with the maximal energy deposit, given by the expression $\omega_{3strips} = \sqrt{\sum E_i \times (i - i_{max})^2 / \sum E_i}$, where i is the number of the strip and i_{max} the strip number of the most energetic one. This variable can help for some particular η bins.

Figure 4.16 shows the average values of the calorimeter-based discriminating variables used for electron/jet separation as a function of the pseudo-rapidity η. Since these variables are pseudo-rapidity dependent, the threshold values were tuned in several intervals. These subdivision is motivated by the varying granularities, lead thickness and material in front of the electromagnetic calorimeter. The first two bins, (0;0.8) and (0.8;1.52), cover the barrel of the electromagnetic calorimeter.

The crack in the calorimeters between $1.37 < |\eta| < 1.52$ is excluded from the analysis. In the end-caps, the intervals are (1.52;1.8), (1.8;2.0), and (2.0;2.5), essentially determined by the varying granularity in the first sampling. The quantities calculated using the first compartment can be used only in the regions $|\eta| < 1.37$ and $1.52 < |\eta| < 2.35$ since outside these regions the granularity is (too) coarse. The cuts on the variables were tuned to obtain an efficiency of about 95%, independent of the pseudo-rapidity η, with respect to the LVL2.

Table 4.6 shows the thresholds of the EF cuts applied at the calorimeter level for low and design luminosity.

4.4.3.3 Event Filter Tracking and Track-Calo Matching Electron Selection

After the calorimeter cuts, the contamination of the inclusive signal from charged hadrons is greatly reduced. The remaining background is dominated by photon conversion and low multiplicity jets containing High p_T π^0 mesons. It can be reduced further by requiring the presence of a good quality track pointing to an electromagnetic cluster with a good energy-momentum match. Cluster and track information are combined in the EMTrackMatchBuilder of the egammaRec algorithm. Only tracks (reconstructed with xKalman++), and with $p_T > 5\,GeV/c$ were kept. An angular matching is done in a window $\Delta\eta = \pm 0.05$, $\Delta\phi = \pm 0.1$ between the selected
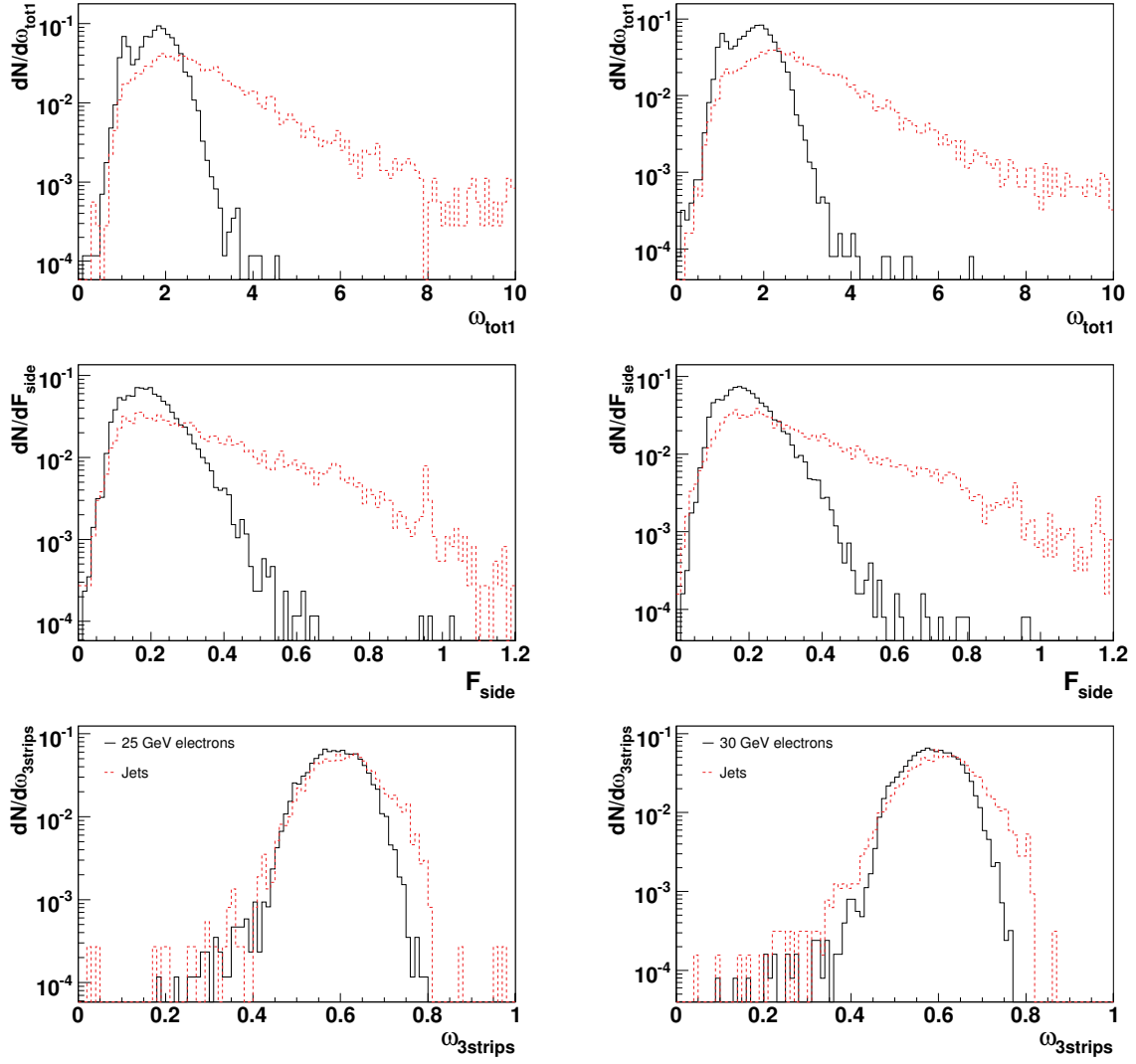
Figure 4.15: *EF discriminating variables in the first EM calorimeter sampling. Distributions are shown for low (left column), and high (right column) luminosity.*

electromagnetic clusters and the position of the track extrapolated to the calorimeter. In case more than one track is found, the one with the highest p_T was retained. If the E/p ratio is less than 4, the track matching is successful. In the subsequent particle identification step the information provided by egammaRec can be used. The following set of track quality cuts were then applied equally for both low and design luminosity:

- at least seven precision hits (Pixel+SCT);

- at least one hits in the pixels, one of which being in the b-layer;

- a transverse impact parameter $|A_0| < 0.2\,cm$.

The jet rejection can be significantly improved by ensuring consistency between the EM calorimeter and the ID information. First, the angular matching between
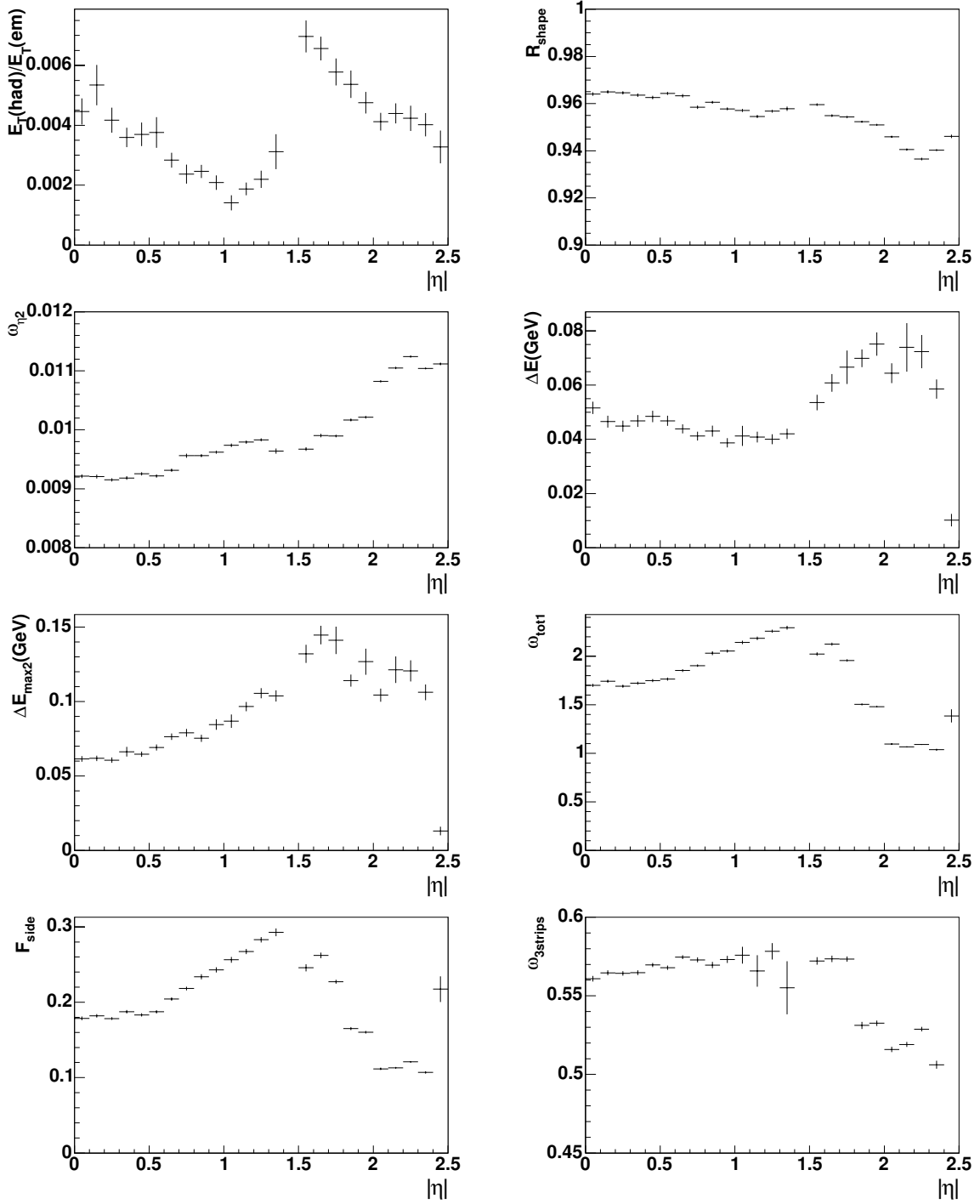
Figure 4.16: *Distribution of the mean of each EF calorimetric discriminating variable as a function of the pseudo-rapidity $|\eta|$ for single electrons at $E_T = 25\,GeV$ and low luminosity.*

the track and the electromagnetic cluster is checked (Figure 4.17):

- $\Delta\eta = |\eta_{clusters}^{strips} - \eta_{ID}|$, where $\eta_{clusters}^{strips}$ is computed in the first sampling of the EM calorimeter, where the granularity is very fine, and η_{ID} is the pseudo-rapidity of the track extrapolated to the calorimeter;

May 26, 2006

	Hadr	R_{shape}	ω_η^2	ΔE_{max2}	ΔE	$\omega 3strips$	ω_{tot1}	F_{side}
	$<$	$>$	$<$	$<$	$<$	$<$	$<$	$<$
	Low Luminosity							
$0 < \lvert\eta\rvert \le 0.8$	0.025	0.915	0.012	0.4	0.15	0.75	2.7	0.35
$0.8 < \lvert\eta\rvert \le 1.52$	0.025	0.91	0.012	0.5	0.15	0.75	3.5	0.6
$1.52 < \lvert\eta\rvert \le 1.8$	0.03	0.89	0.012	0.9	0.35	0.80	3.5	0.68
$1.8 < \lvert\eta\rvert \le 2.0$	0.02	0.92	0.0115	0.9	0.20	0.70	2.0	0.3
$2.0 < \lvert\eta\rvert \le 2.5$	0.015	0.91	0.0125	0.3	0.6	0.60	1.4	0.2
	Design Luminosity							
$0 < \lvert\eta\rvert \le 0.8$	0.055	0.89	0.011	0.65	0.2	0.75	2.8	0.35
$0.8 < \lvert\eta\rvert \le 1.52$	0.060	0.89	0.012	0.8	0.2	0.75	3.5	0.6
$1.52 < \lvert\eta\rvert \le 1.8$	0.065	0.87	0.013	1.1	0.45	0.80	3.2	0.58
$1.8 < \lvert\eta\rvert \le 2.0$	0.085	0.92	0.0115	1.1	0.70	0.70	2.1	0.3
$2.0 < \lvert\eta\rvert \le 2.5$	0.07	0.91	0.0125	1.1	0.8	0.60	1.4	0.22

Table 4.6: *Cuts applied in the EF calorimetric variables at low and design luminosity. The crack region in the EM calorimeter between $1.37 < \lvert\eta\rvert < 1.52$ was excluded from the analysis.*

 – $\Delta\phi = \lvert\phi_{clusters}^{middle} - \phi_{ID}\rvert$, where $\phi_{clusters}^{middle}$ is computed in the second compartment of the EM calorimeter and ϕ_{ID} is the azimuth of the track extrapolated to the calorimeter;

Subsequently, the energy E measured in the electromagnetic calorimeter is compared to the momentum p measured in the Inner Detector (see Figure 4.18). In the case of an electron, the momentum should match the energy. Still, large tails at low and high values of the ratio can be seen. These are due to conversion electrons as well as soft bremsstrahlung.

4.4.3.4 Use of Transition Radiation in the TRT Information

A further reduction of the charged hadron contamination is obtained by rejecting tracks having a low fraction of high-threshold Transition Radiation TR hits. Figure 4.18 shows the ratio N_{TR}/N_{straw} between the number of high threshold hits NTR and the total number of TRT hits N_{straw} . The thresholds applied at the TRT level for this study were defined in p_T and η bins, and are shown in Table . They were tuned to obtain $\sim 90\%$ electron efficiency at low and design luminosity on tracks which pass the LVL1 and track quality cuts.

 Table 4.7 shows the thresholds applied on these quantities for the different pseudo-rapidity η ranges.
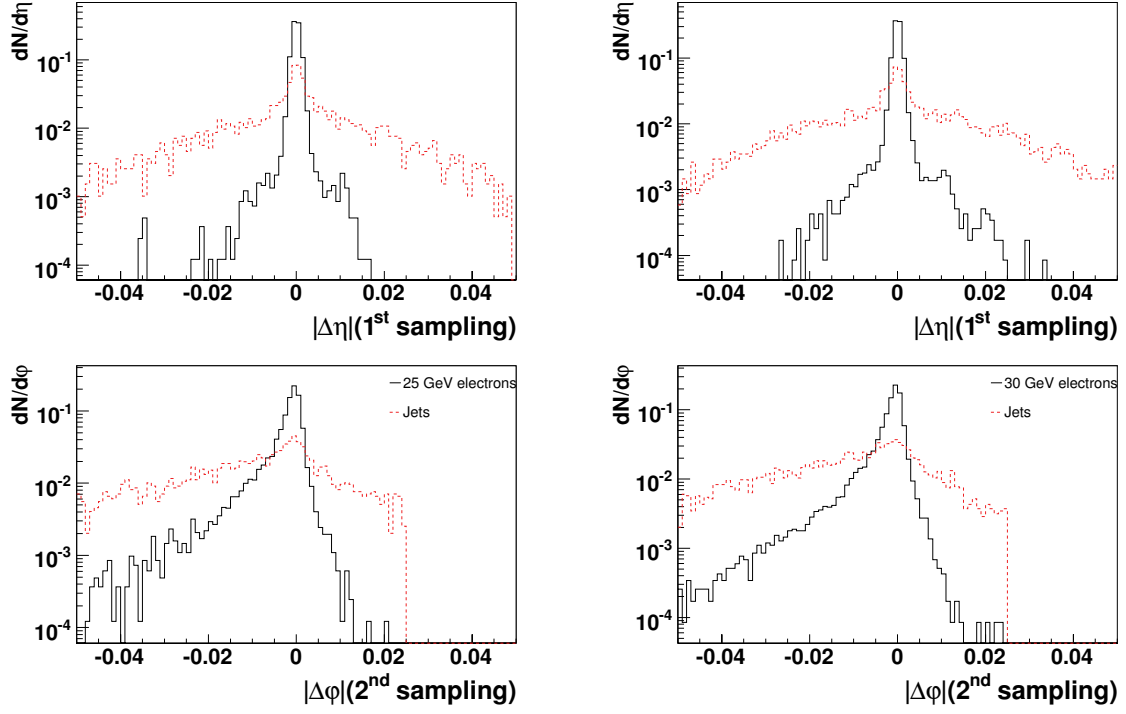
Figure 4.17: *EF angular matching between charged tracks extrapolated to the EM calorimeter and EM clusters in pseudo-rapidity (η) and azimuth (φ). Distributions are shown for $25\,GeV$ electrons and jets at low luminosity (left column), and $30\,GeV$ electrons and jets at design luminosity. Only the LVL1 trigger was applied before hand.*

| | $\Delta\eta$ | $\Delta\phi$ | E/p | | N_{TR}/N_{str} |
	<	<	>	<	>
			Low Luminosity		
$0 < |\eta| \le 1.0$	0.01	0.02	0.8	2.5	0.10
$1.0 < |\eta| \le 1.52$	0.01	0.02	0.8	2.5	0.10
$1.52 < |\eta| \le 2.0$	0.01	0.02	0.8	2.7	0.10
$2.0 < |\eta| \le 10.0$	0.01	0.02	0.8	2.7	0.10
			Design Luminosity		
$0.0 < |\eta| \le 1.0$	0.015	0.02	0.7	1.7	0.10
$1.0 < |\eta| \le 1.52$	0.015	0.02	0.7	1.7	0.10
$1.52 < |\eta| \le 2.0$	0.015	0.02	0.7	2.6	0.10
$2.0 < |\eta| \le 10.0$	0.015	0.02	0.7	2.6	0.10

Table 4.7: *Cuts applied in the EF ID/calorimetric matching variables at low and design luminosity as a function of η. The crack region in the EM calorimeter between $1.37 < |\eta| < 1.52$ was excluded from the analysis.*
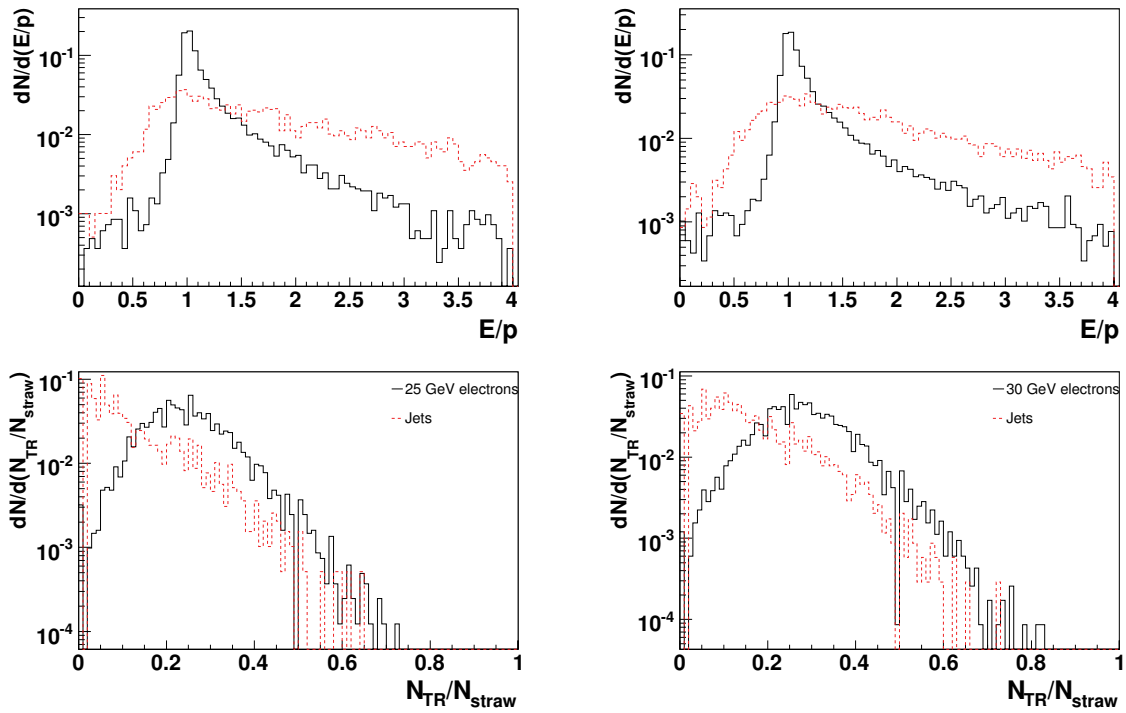
Figure 4.18: *Top: EF Ratio E/p between the energy of the EM clusters to momentum of reconstructed charged tracks for low (left), and design (right) luminosity. Bottom: EF ratio N_{TR}/N_{straw} for low (left), and design (right) luminosity. Distributions are shown for $25\,GeV$ $(30\,GeV)$ electrons at low (design) luminosity. Only the LVL1 trigger was applied before hand.*

4.5 Physics Validation of the LVL2 Trigger Code

4.5.1 T2Calo

The T2Calo algorithm running within the HLT software, has been validated with the offline EM cluster reconstruction software. In order to study possible differences, the quantities calculated with T2Calo have been compared with those obtained from the offline in an event-by-event basis, using the same data files.

Using $25\,GeV$ electrons, Figure 4.19 compares reconstructed EM cluster quantities at LVL2 and the offline for the four variables used in the rejection at LVL2: lateral shape in sampling 2 (R_{shape}), strip energy ratio of sampling 1 (R_{strip}), total EM E_T , and hadronic energy. The agreement is good except for the total EM E_T, for which the on-line reconstruction underestimates the energy. This is due to the fact that the offline currently uses better calibration constants and cluster corrections.
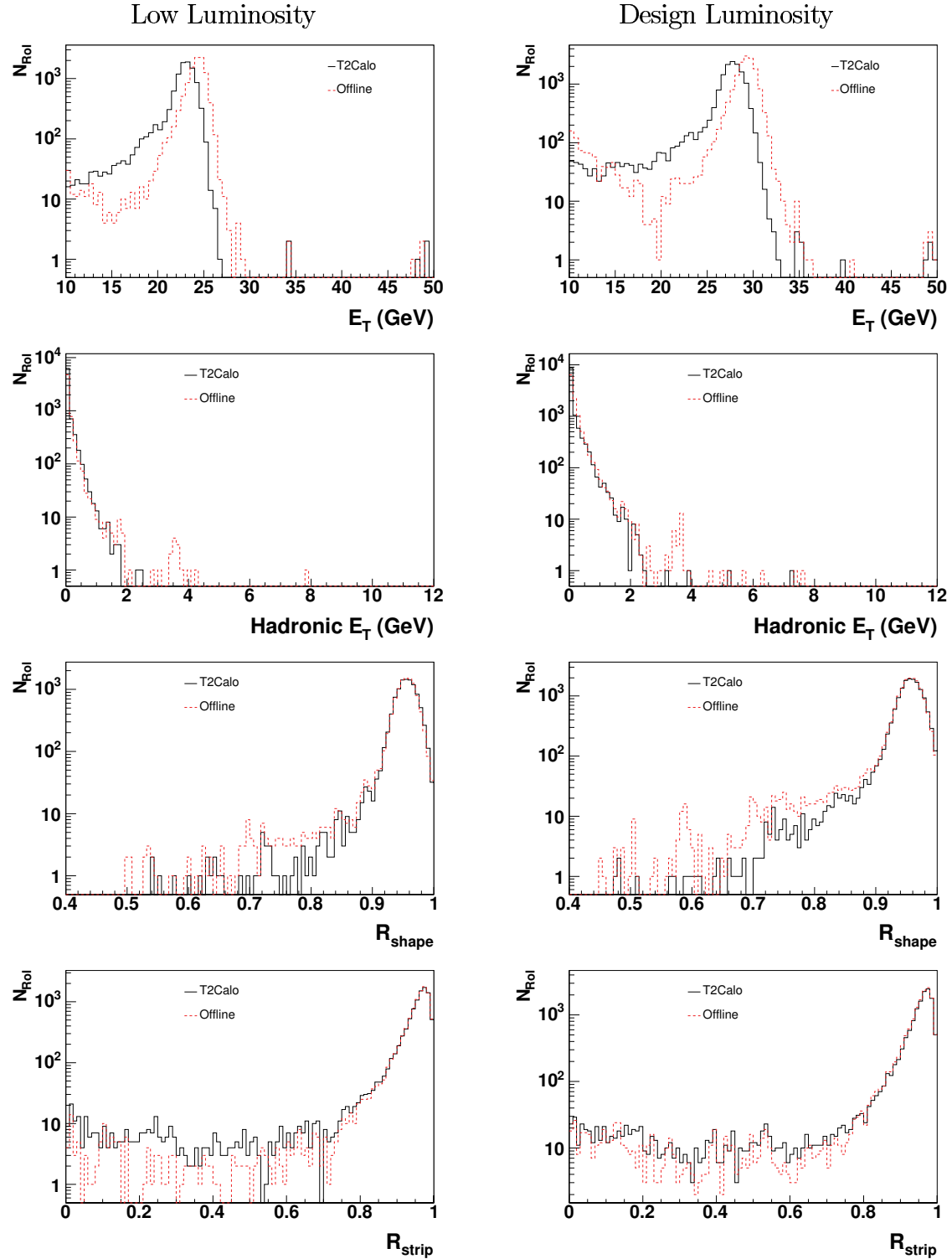
Figure 4.19: *Comparison of the different calorimeter variables used for electron jet rejection at LVL2 for T2Calo and the offline for low luminosity (left column) and design luminosity (right column). The samples used were single electrons with $E_T = 25\,GeV$ ($E_T = 25\,GeV$) at low (design) luminosity.*

Figure 4.20 presents the difference between the η and ϕ values reconstructed with T2Calo and those obtained with the offline clustering algorithm (egammaRec). The difference can be explained by the cluster corrections applied in the offline for both η and ϕ. In the offline, s-shape corrections are applied for the measured η values, and the ϕ direction is also corrected for an offset [8].
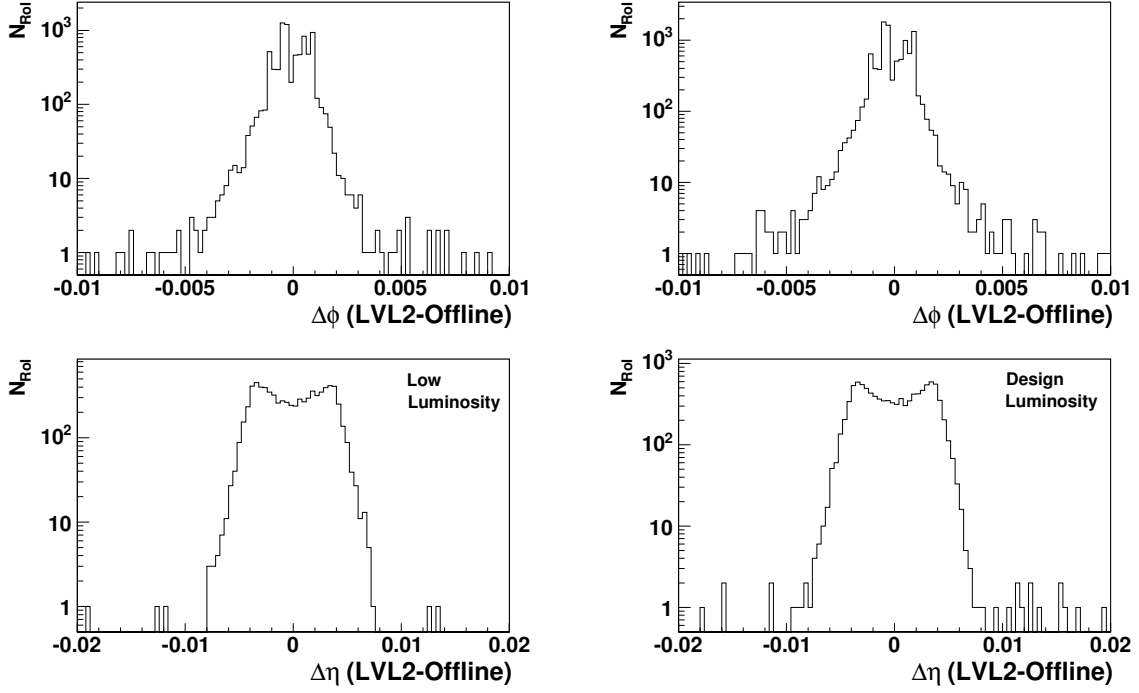
Figure 4.20: *Difference in η and ϕ between the reconstructed cluster values at LVL2 and in the offline for low luminosity (left column) and design luminosity.*

4.5.2 IDscan

Validation of the offline and on-line versions of IDscan has been carried out with respect to the xKalman full reconstruction package. Only events where xKalman is able to reconstruct tracks satisfying the following criteria are considered:

- $\Delta r = \sqrt{(\eta - \eta_{true})^2 + (\phi - \phi_{true})^2} < 0.1$

- $Z_0 - Z_{0true} < 0.2$

- $\left| \frac{p_T - p_{True}}{p_{True}} \right| < 0.5$

IDSCAN and xKalman reconstruct more than one track in most events. A single track is selected from each event using matching to the truth η and ϕ values for the electron candidate. For events where the xKalman track satisfied the above criteria, the same criteria are applied to the IDscan track. The latest validation results are summarized in Table 4.8, these were obtained from 2500 low/high luminosity events.

	Low Luminosity	Design Luminosity
Online	92.3%	83.3%
Offline	95.6%	93.3%

Table 4.8: *IDscan track efficiencies for offline and online versions. Both low luminosity (using $E_T = 25\,GeV$ electrons), and design luminosity (using $E_T = 30\,GeV$ electrons) scenarios were studied.*

The drop in efficiency at low and high luminosity for the Online algorithm is under investigation. Plots for the p_T, η, ϕ, Z_0 and d_0 distributions for high luminosity are presented in Figure 4.21. These highlight problems with the η and Z_0 resolutions at high luminosity for the online version.

4.6 Electron Selection Performance

After defining the LVL2 and EF electron trigger quantities, the next step is to evaluate the trigger performance in terms of efficiency and background rate. The HLT electron trigger consist of a series of trigger menus (see Table 1.1) requiring typically one or two trigger objects per event. In this section, only the physics performance of the single high p_T electron trigger is reviewed using the datasets described in Section 1.3. The trigger efficiency is specified as a percentage of reconstructed electrons to the total number of generated on a given step.

4.6.1 Optimization of Selections

The strategy followed in optimizing the HLT electron trigger selections is to obtain high efficiency and a good background rejection, while keeping the selection criteria relatively simple.

The optimal selection cuts for the LVL2 trigger quantities were found by a procedure which scans the allowed multidimensional parameter space and finds, for each efficiency, the set of cuts which the lowest background rate. The method is illustrated in Figure 4.22: The parameter space is scanned in equal probability bins for reasonable values of the selections; Figure 4.22 shows the efficiency for signal and the background rate corresponding to each parameter set at low luminosity. The left edge of the collection of points corresponds to the parameter sets with highest efficiency and lowest background (i.e. each point on the curve represents a set of selections , which gives the best performance).
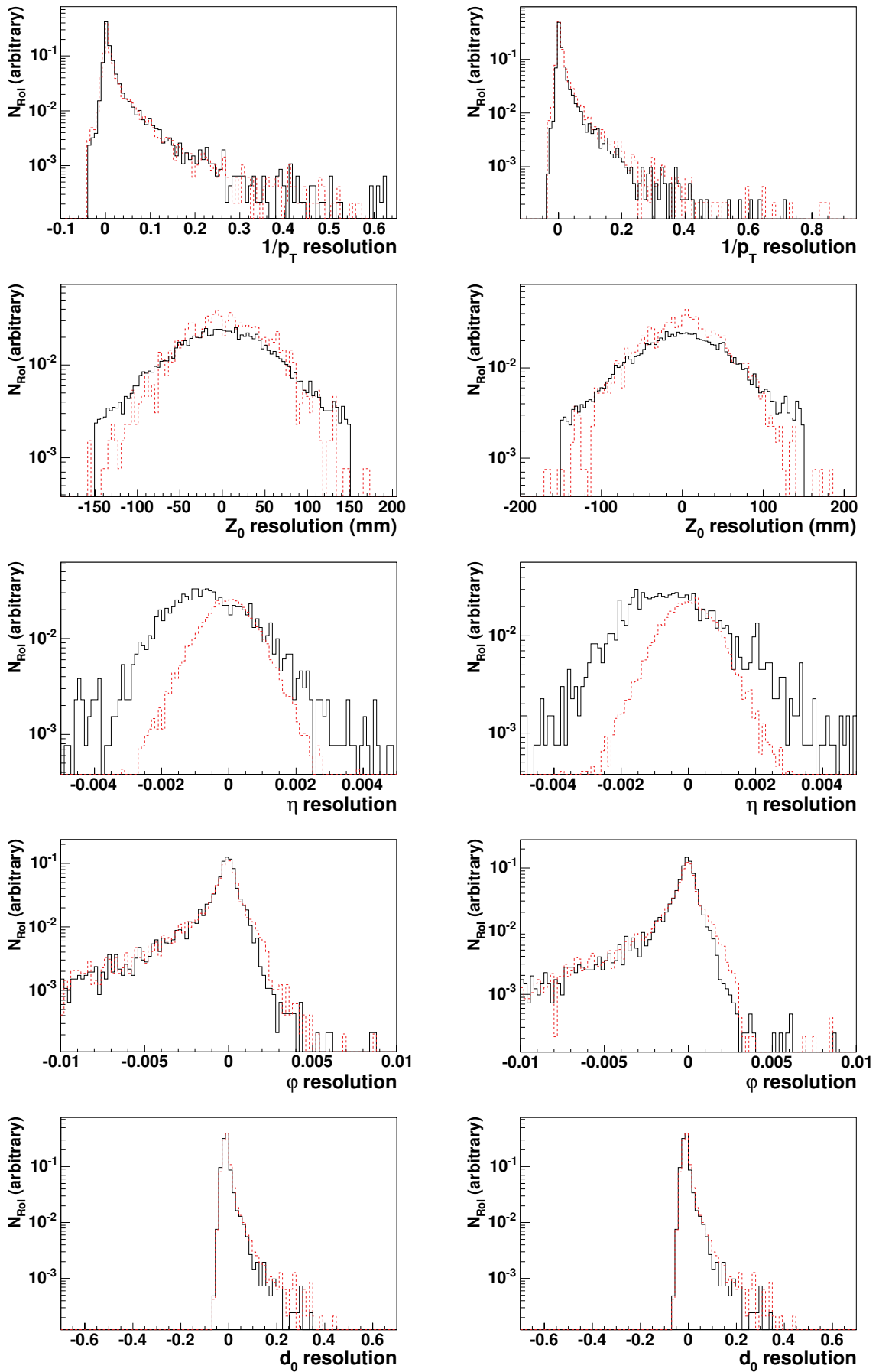
Figure 4.21: *Comparison of different track reconstruction parameters between IDScan (solid lines) and xKalman (dotted lines) for $E_T = 25\,GeV$ single electrons at low luminosity (left column), and $E_T = 30\,GeV$ single electrons at design luminosity (right column).*
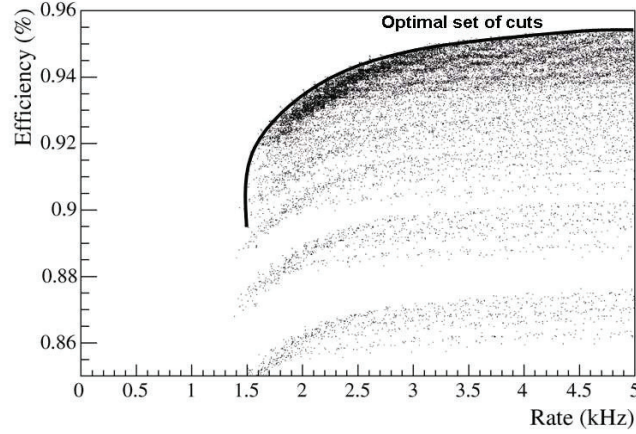
Figure 4.22: *The optimization procedure finds the best efficiency possible for a given rate by scanning the multidimensional space of all the cuts combinations. This example shows the efficiency and rate for the LVL2 calorimeter cuts scanned in 30 equal probability bins*

4.6.2   Overall Performance

The currently achieved performance of single-object electron trigger at low and design luminosities is given in Table 4.9 as a function of the main steps in the LVL2-EF trigger chain. The trigger steps are factorized by detector to show the break-down after each major selection step. After each of these steps the trigger will fail with a yes/no decision and only if the object pass this decision successfully the next step will be carried out. It should be noted that correlations exist between the different steps, and work is in progress to further optimize the selections.

The overall reduction in rate achieved at low (design) luminosity by LVL2 is 90(100) for a loss of efficiency of 13%(10%) with respect to LVL1[2]. The additional rate reduction provided by the EF is a factor of 5(4) for a further efficiency loss of 10%(9%). This results are consistent with the ones obtained in previous studies [1]- [4], and show that HLT selection is very powerful. One known problem, as was shown in section 1.6, arises from the LVL2 tracking algorithm. At low luminosity, in around 3% of the events IdScan does not reconstruct a track, which is, however, reconstructed using the offline track reconstruction. This problem gets even worst at design luminosity, with 10% of the events not reconstructed by IdScan. These "missing track" events are due to a problem in the online space-points and are equally distributed in $\eta - \phi$ space. For the efficiencies presented here, all the events with at least one track found by xKalman (offline equivalent of IDScan), but with zero tracks reconstructed on-line were not considered in the analysis.

---

[2]The efficiencies and rates are given with respect to a LVL1 output efficiency of 95% and a LVL1 rate for EM clusters of $12\,kHz(14\,kHz)$.

Trigger Step	Low Luminosity		Design Luminosity	
	Efficiency (%)	Rate (Hz)	Efficiency (%)	Rate (Hz)
LVL2 Calo	95.9 ± 0.3	2114 ± 48	97.4 ± 0.3	3408 ± 62
LVL2 Tracking	88.0 ± 0.5	529 ± 24	92.0 ± 0.3	780 ± 30
LVL2 Matching	86.6 ± 0.6	137 ± 12	90.6 ± 0.4	420 ± 16
EF Calo	84.4 ± 0.6	56 ± 8	90.5 ± 0.5	340 ± 15
EF Tracking	82.4 ± 0.6	46 ± 8	84.8 ± 0.6	279 ± 13
EF Matching	79.0 ± 0.7	30 ± 5	78.2 ± 0.6	176 ± 11

Table 4.9: *Performance of the single electron HLT trigger at low (design luminosity). The results are presented in a single sequence. The efficiencies are given for single electrons of $p_T = 25\,GeV$ (30 GeV) over the full rapidity range $|\eta| < 2.5$, and excluding the barrel/end-cap overlap region. The efficiencies and rates are given with respect to a LVL1 output efficiency of 95% and a LVL1 rate for EM clusters of 12kHz (16kHz). Some problems in the LVL2 tracking code as discussed in the text result in a drop in efficiency of around 3% (10%). Events with at least one track found by xKalman (offline equivalent of IDScan), but with zero tracks reconstructed on-line, were not considered for the analysis.*

As a first cross-check for the low luminosity scenario, the electron efficiencies have been extracted using fully simulated $W \to e\nu$ events at low luminosity. The efficiencies obtained were $(90.6 \pm 0.9\%)$ after LVL2 and $(79.8 \pm 1.2\%)$ after EF, and have been obtained using events for which the electron has a $p_T > 25\,GeV$ at generator level. These values are slightly higher than the ones given in table 4.9 for single electrons of $E_T = 25\,GeV$. This is expected since the efficiency is better for electrons with p_T well above the threshold value as shown in Figure 4.23.
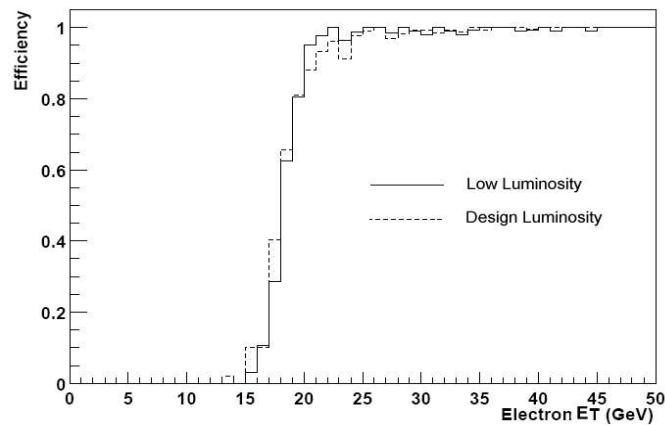
Figure 4.23: *Single electron trigger efficiency as a function of the electron transverse energy E_T, using a 17 GeV threshold for different luminosity scenarios.*

4.7 Conclusions and Outlook

In this chapter the performance of the electron triggers has been analyzed for low (design) luminosity, and using a more up to date detector description and a more realistic tuning of the MC generators. A final LVL2 rate of $137\pm12\,Hz(420\pm16\,Hz)$ for an electron efficiency of $86.6\pm0.6(90.6\pm0.6)$ for the e25i(e30i) trigger has been found. At the EF, a rate of $30\pm5\,Hz$ $(176\pm11\,Hz)$ and an electron efficiency of $79.0\pm0.7(78.2\pm0.7)$ have been obtained. These results are comparable to the rate estimates obtained in earlier studies. As a cross-check, the efficiency to select $W\rightarrow e\nu$ events for which the electron has a $p_T>25\,GeV$ at generator level is $(90.6\pm0.9\%)$ after LVL2 and $(79.8\pm1.2\%)$ after EF. These results show the new HLTSSW and the selection algorithms are working satisfactory. However, additional studies are ongoing with the latest offline software releases.

Bibliography

[1] ATLAS collaboration, High Level Triggers, DAQ and DCS Technical Proposal, CERN/LHCC/2000-17, (2000).

[2] R. Mommsen, A. Radu, M. Wielers,"Performance studies for electron and photon selection at the event filter", ATLAS internal note, ATL-DAQ-2000-007 (2000).

[3] R. Mommsen, "Electron trigger performance studies for the event filter", ATLAS internal note, ATL-DAQ-2001-004 (2001)

[4] J. Baines et al., "First study of the LVL2-EF boundary in the high-pT e/gamma high-level- trigger", ATLAS internal note, ATL-DAQ-2000-045 (2000)

[5] http://atlas.web.cern.ch/Atlas/GROUPS/SOFTWARE/OO/domains/Reconstruction/inAtl

[6] Díaz-Gómez, M; Wildauer, A; Moyse, E J W; Pérez-Réale, V; Padilla, C, The e/γ Analysis Framework, ATLAS Communications, ATL-COM-DAQ-2004-010 (2004).

[7] ATLAS Collaboration, HighLevel Trigger Data Acquisition and Controls Technical Design Report, 2003. CERN/LHCC/2003022

[8] ATLAS collaboration, Calorimeter Technical Design Report, CERN/LHCC/96-41, ATLAS TDR 2, (1996).

[9] ATLAS collaboration, Inner Detector Technical Design Report, CERN/LHCC/97-17, ATLAS TDR 5, (1997).

[10] ATLAS DC1 Task Force, 'ATLAS DATA Challenge 1', http://atlasinfo.cern.ch/Atlas/GROUPS/SOFTWARE/DC/DC1/Data_Challenge1_030425.p (2003).

[11] Stefan Simion, Pile-up Simulation for ATLAS Calorimeters, http://home.cern.ch/s/simions/www/pileup/pileup.ps, 19 Jun 1998.

[12] T. Sjöstrand, Comp. Phys. Comm. 82 (1994) 74; T. Sjöstrand, 'Pythia 6.206 Manual', LU TP 01-02 [hep-ph/0108264], (2002).

[13] R. Brun et al., http://root.cern.ch

[14] Application Software Group, CERN program library long writeup W5013.

[15] Eisenhandler, EF, ATLAS Level-1 Calorimeter Trigger Algorithms, ATL-DAQ-2004-011 (2004).

[16] ATLAS level-1 trigger technical design report, CERN/LHCC 98-14, ATLAS TDR-15, June 1998.

[17] M.P. Casado, S. Gonzlez, and T. Shears, TrigT2Calo package, http://atlas-sw.cern.ch/cgi-bin/cvsweb.cgi/offline/Trigger/TrigAlgorithms/ TrigT2Calo/

[18] H. Drevermann and N. Konstantinidis, Determination of the z position of primary interactions in ATLAS," ATL-DAQ-2002-014 (2002).

[19] For more information on SCTKalman see P. Billoir and S. Qian, Nucl. Instr. Meths., A294 (1990) 219; P. Billoir and S. Qian, Nucl. Instr. Meths., A295 (1990) 492; I. Gaines, T. Huehn, and S. Qian, in Proceedings of CHEP1997 (Berlin); I. Gaines and S. Qian, in Proceedings of CHEP1998 (Chicago); I. Gaines, S. Gonzalez and S. Qian, in Proceedings of CHEP2000 (Padova); D. Candlin, R. Candlin and S. Qian, in Proceedings of CHEP2001 (Beijing); J. Baines, et al. ATL-DAQ-2000-031.

[20] I. Gavrilenko, Description of Global Pattern Recognition Program (xKalman), ATLAS Internal Note, ATLAS-INDET-97-165 (1997) http://maupiti.lbl.gov/atlas/xkal/xkalmanpp/index.en.html.

[21] R.K. Mommsen, A. Radu and M. Wielers, Performance Studies for Electron and Photon Selection at the Event Filter, ATLAS Internal Note, ATL-DAQ-2000-007 (2000).

[22] R.K. Mommsen, Electron Trigger Performance Studies for the Event Filter, ATLAS Internal Note, ATL-DAQ-2001-004 (2001).

Chapter 5

Monitoring the HLT High-p_T Electron Trigger using the $Z \rightarrow e^+e^-$ physics channel

5.1 Introduction

The ability to trigger on isolated high p_T electrons is of vital importance to many areas of physics at the LHC, as discussed in Chapter 3. As the trigger efficiency will be a key parameter in several physics analyses, it is important to have several independent methods of estimating it, depending as little as possible on the Monte Carlo description of the detector and running conditions, as this is necessarily incomplete. Indeed, for the energies and interaction rates expected at the LHC, the background components and more generally the underlying interaction physics are only approximatively known. Therefore uncertainties up to a factor of 5 [7] can be expected in the Monte Carlo predictions. Furthermore, the HLT event selection is a complex online proccess, which is itself integrated in the ATLAS DAQ system, where many factors could act as a potential source of inefficiencies (network related problems, hardware failures, buffer overflows, etc.).

An accurate and realistic measurement of the HLT electron trigger efficiencies must therefore take these degrading factors into consideration.

Another requirement is to have a clean sample of unbiased electrons. This diagnostic sample should in principle be selected with soft identification requirements, thus minimizing the introduction of biases. Samples of electrons from W and Z events are in principle perfect candidates, since the electrons then have all the characteristics (e.g. the underlying event or multiple interaction effects) which might affect the efficiencies that need to be measured. Despite its large production rate($\sim 10\,\mathrm{Hz}$ for a peak luminosity of $2 \times 10^{33}\,cm^{-2}\,s^{-1}$), an efficiency measurement from a sample of W electrons is quite difficult, since the reconstruction of the W invariant mass is impossible due to the presence of a neutrino. Without a clean mass peak with a good signal to background ratio, one is constrained to use tight electron identifica-

tion criteria just to define the diagnostic sample, thus introducing bias and possible correlation effects.

$Z \to e^+e^-$ events are much better suited for this task. Their production rate at LHC will be large($\sim 1\,\mathrm{Hz}$ for a peak luminosity of $2 \times 10^{33}\,cm^{-2}\,s^{-1}$), and they will produce rather clean and well measurable signatures containing isolated electrons. By requiring the reconstructed dielectron invariant mass to be close to M_Z, and by imposing a tight electron identification criteria on one of the electrons, one obtains a clean sample of unbiased electrons with a small background component.

In this chapter, a method to to determine the HLT electron trigger efficiency using $Z \to e^+e^-$ events plus online tagged information is described. This approach has the additional advantage that possible online sources of degradation are also taken into account.

5.2 Detector Layout and Data Samples

In this study the DC1 detector layout was used. A detailed description of the geometry and granularities of the different subdetectors can be found in [1]. Monte Carlo events were generated with PYTHIA 6.203, and reconstructed using ATHENA release 6.0.4. A total of 10000 $Z \to e^+e^-$ were produced at low luminosity with a cross-section of $1.515\,pb$. At the generator level, electrons were required to be in the pseudorapidity range $|\eta| < 6.0$.

The robustness of the method against the background contamination to the $Z \to e^+e^-$ channel was studied with a sample of QCD di-jet events. The full simulation of di-jets, although a necessary step to test in a realistic manner the robustness of the method described later on in this chapter, also represents a major challenge; the high jet rejection rate(10^5, see chapter 3) expected for the HLT single inclusive electron trigger configuration, together with the condition of having at least two electron candidates passing the offline selection criteria, requires a very large sample (several thousands) of events passing the LVL1 trigger, in order to have a significant number of entries within the $Z \to e^+e^-$ mass window range. Due to computer time considerations, the following techniques were employed to speed up the process:

1. The Monte Carlo event generator PYTHIA 6.2 was set up to produce two-jet events, with the final state partons from the hard scattering having $p_T > 17\,GeV$, and being constrained to the rapidity region $|\eta| < 2.7$.

2. A pre-filter was applied at the particle level to remove events which had no chance of producing a level 1 trigger

A total of 250000 di-jet events were generated this way, and then put through the full detector simulation.

May 26, 2006

5.3 Geometric and Kinematic Acceptance

In order to estimate the $Z \to e^+e^-$ production rate needed for this study, one needs to know what fraction of the events produced can be reconstructed. Electrons might escape detection if they enter an uninstrumented region of the detector, or can be neglected if they do not satisfy certain kinematical constrains. Since one has no way of counting the number of events which are undetected, the geometric and kinematic acceptances are calculated using Monte Carlo information. The overall detector acceptance was defined as the fraction of generated events that pass the following reconstruction level cuts:

1. The $p_T^{electron}$ must be greater than $25\,GeV$. This is the minimum value adopted for the high p_T electron inclusive trigger definition.

2. The pseudorapidity η must be in the range $|\eta| < 2.5$. Beyond this limit, electromagnetic calorimeter signals will not be processed by the Level 1 logic.
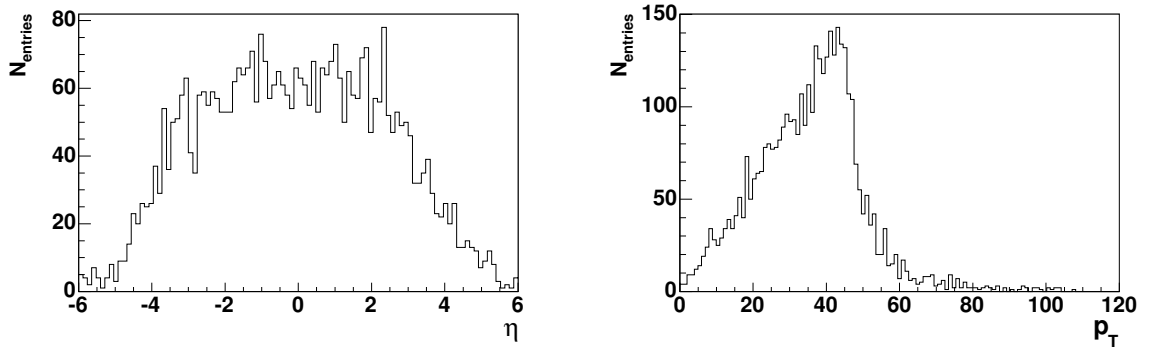
Figure 5.1: *Generated η, and p_T distributions for all generated Zee electrons.*

Figure 5.1 shows the pseudorapidity η and p_T distributions for the generated electrons comming from the Z decay. For the $Z \to e^+e^-$ sample, two EM candidates are required to pass these cuts, and in addition, their reconstructed invariant mass must lie within the $70 < M_{ee} < 110\,GeV/c^2$ window. Figure 5.2 shows the invariant mass distributions of the Z generated sample, and the reconstructed one. Note that the detector fidutial constraints are implicitly contained in the reconstructed sample (i.e. an electron hitting a non-instrumented region will not be reconstructed).

The geometrical acceptance of ATLAS for $Z \to e^+e^-$ events generated by PYTHIA was found to be $22.23 \pm 0.06\%$, where the uncertainty is the statistical error of the Monte Carlo simulation sample. The systematic error contribution was not considered.
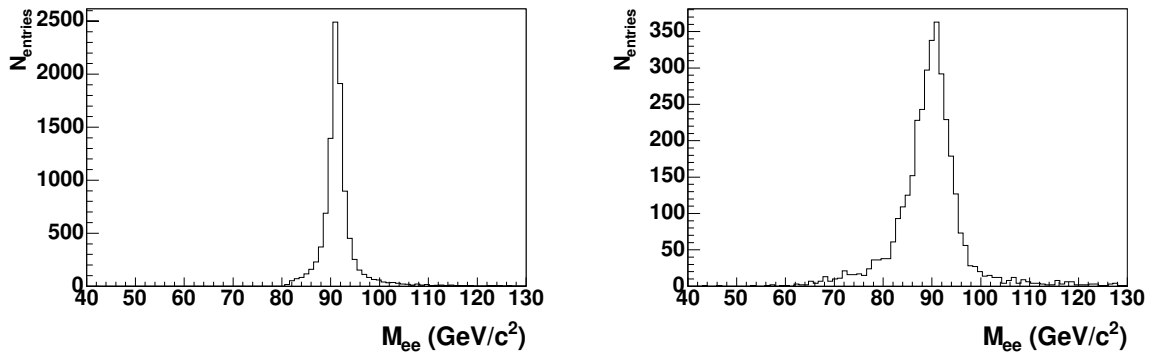
Figure 5.2: *Invariant mass distributions of the generated (left) and reconstructed (right)* $Z \to e^+e^-$ *sample. For those events in which more than two electromagnetic clusters were reconstructed, the invariant mass was calculated using the two clusters with highest transverse momentum*

5.4 Background Contributions

Events other than $Z \to e^+e^-$ can sometimes pass the Z selection criteria and contaminate the data samples. These background events can be physical or instrumental. Physical backgrounds are the result of other physical processes with a final state which is indistinguishable from the one under study (e.g. QCD events in which two jets mimic the $Z \to e^+e^-$ signature). Instrumental backgrounds are the result of physical processes with final states different from the one under study, but which are misidentified by the detector.

The event selection cuts are designed to accept a large fraction of Z events while rejecting as much background as possible. Since it is desirable to have a large sample of signal events in order to reduce statistical and even systematic uncertainties, these cuts represent a compromise between retaining high efficiency and reducing the background, and as a result a small amount of background is unavoidable.

The $Z \to e^+e^-$ channel presents, nevertheless, a rather clean signature and is thus ideal for studying electron identification efficiencies. Its resonance peak is well defined, and the background dependence on the ee mass is weak, which makes the parametrization of true and false signal contribution easy. The largest source of background are QCD di-jets, containing a real electron($bb \to e\nu x$) and a fake electron (a jet faking an electron), or two fake electrons. Other contributions come mainly from the Drell-Yan process($q\bar{q} \to \gamma^* \to l^+l^-$) and $Z \to \tau\tau$ events, where the taus decay into electrons. Figure 5.3 shows the reconstructed invariant mass spectrum of di-jet events. .

5.5 $Z \to e^+e^-$ Data Event Selection

Candidate $Z \to e^+e^-$ events are identified through their decay to two electrons which have an invariant mass consistent with the mass of the Z boson. The decay
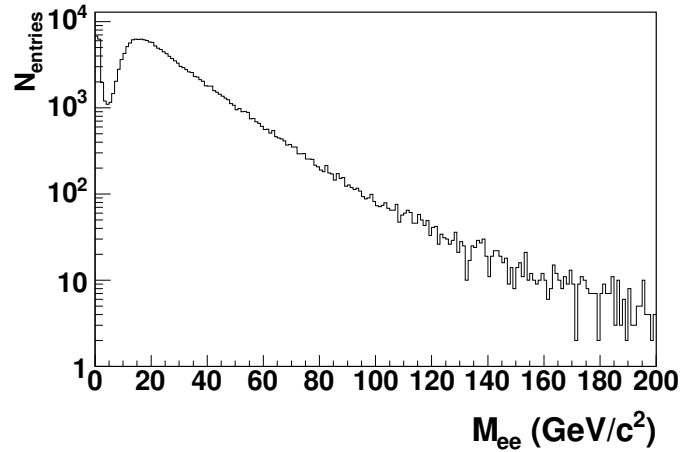
Figure 5.3: *Invariant mass spectrum of the QCD di-jet reconstructed sample. For those events in which more than two electromagnetic clusters were reconstructed, the invariant mass was calculated using the two clusters with highest transverse momentum. No trigger selection was applied*

leptons have a transverse energy distribution (Fig. 5.1) peaking towards half the mass of the vector boson(i.e $45\,GeV$).

The particles that balance the component of the Z momentum transverse to the beam axis are referred to as the "recoil" and they ususally deposit little transverse energy since the p_T distribution of the Z boson peaks at about $7\,GeV$, and falls off rapidly at higher values. These particles are indistinguishable from the underlying event(particles from the break-up of the proton and anti-proton in the inelastic collision), which, as it can be observed in Fig. 5.4, it only contains low p_T elements. Backgrounds to the $Z \to e^+e^-$ samples are discussed in section 4.9.
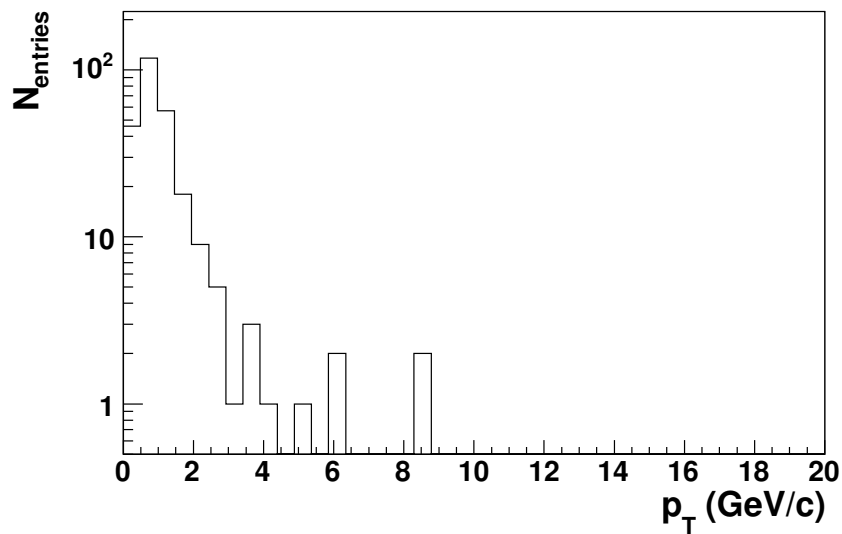
Figure 5.4: *Generated transverse momentum distribution of particles comming from underlying event interactions.*

This section gives an overview of the proposed selection strategy of $Z \to e^+e^-$ event candidates, for determining high level electron trigger efficiencies. The LVL1, and HLT trigger configuration will be briefly described in terms of selection signatures and requirements, followed by the envisaged offline selection criteria.

5.5.1 LVL1 Trigger Configuration

A single electron trigger will be applied for the selection of $Z \to e^+e^-$ events. The LVL1 trigger for single electrons demands that there is at least one EM trigger tower within an RoI, with transverse energy above $19\,GeV$. A trigger tower covers in this case $\Delta\eta \times \Delta\varphi = 0.2 \times 0.2$, and contains most of the energy of an EM shower. In addition, some isolation requirements must be fulfilled (see chapter 3).

After the LVL1 selection of $Z \to e^+e^-$ events yield mainly single object RoIs, where one of the electrons does not meet the acceptance requirements of the detector, and double object RoIs. Three RoIs could also be present in a smaller proportion if one or two of the decay electrons radiates a photon (Fig. 5.5).
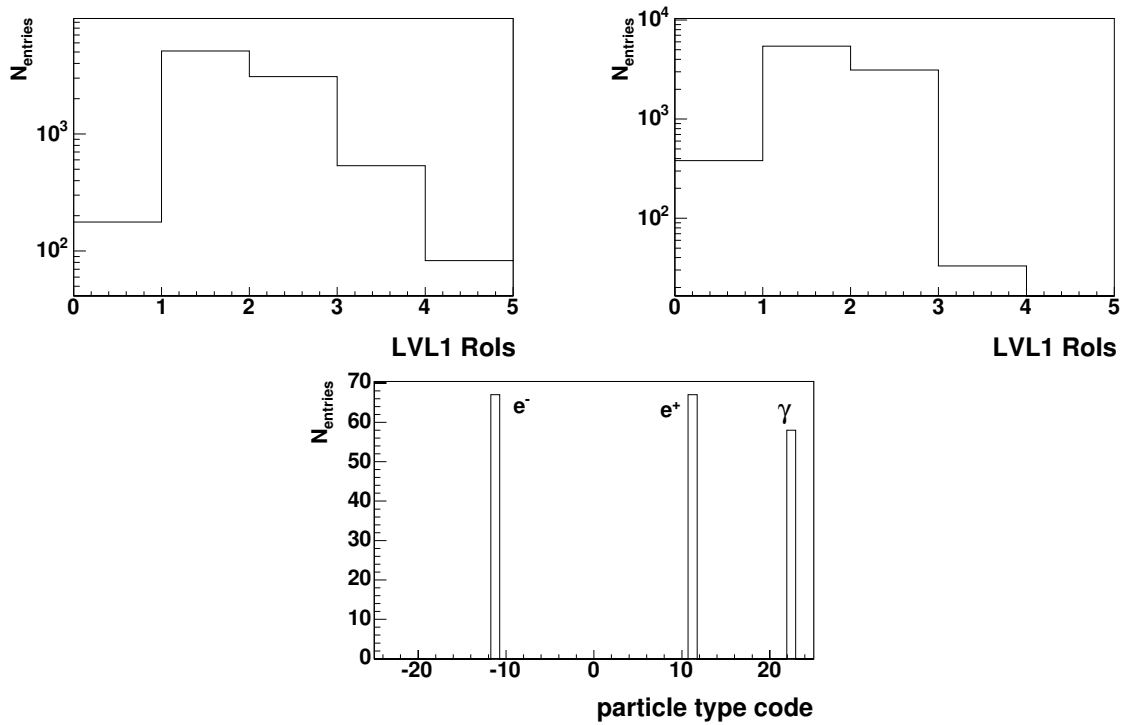
Figure 5.5: *LVL1 RoIs generated by $Z \to e^+e^-$ events before (top left), and after (top right) applying the LVL1 RoI trigger selection. The botton figure shows the particle composition of those events for which three RoIs pass the LVL1 selection.*

Figure 5.6 shows the number of LVL1 RoIs generated by QCD di-jet events, before, and after applying the LVL1 trigger selection. As can be observed, the main background contamination that gets transmited to the HLT system consist of single and double RoIs.
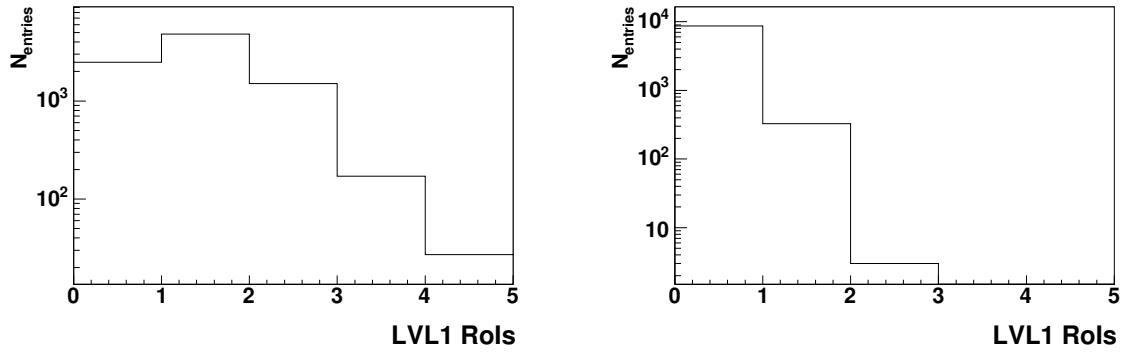
Figure 5.6: *LVL1 RoIs generated by QCD di-jet events. Distributions are shown before (left), and after (right) applying the LVL1 RoI trigger selection.*

5.5.2 HLT Trigger Configuration

After the LVL1 trigger, $Z \to e^+e^-$ events will yield single and double electron candidates. These will be triggered by the HLT high p_T single electron trigger e25i, which has been extensively studied in chapter 3, including a detailed description of the different selection criteria and cuts employed. Therefore, they will not be covered again here. Distributions of the selection variables employed at LVL2 are shown in Fig. 5.7 for Z decayed electrons, and QCD di-jets.

A flag will be added online to those events in which two electron candidates satisfied the trigger requirements. This information can be included in the event stream data and be read back again for offline analysis.

5.5.3 Offline Selection

After the full trigger chain, offline $Z \to e^+e^-$ candidate events will be selected according to the following requirements:

- One electron candidate must pass the single electron e25i trigger.

- The presence of a second electron candidate with $E_T > 25\,GeV$. Events with more than two electron candidates are not selected.

- The pseudorapidity distribution of any electron candidate must be in the range $|\eta| < 2.5$.

- The invariant mass of the two electron candidates must lie within the range $70 - 110\,GeV$.

   The final set of $Z \to e^+e^-$ candidates obtained this way will be tagged as the diagnostic sample. From this events, a second sub-sample must be extracted, containing the events in which a flag was added by the online system (indicating that at least two electron candidates passed the HLT single electron trigger). These events will form the flagged sample. The meaning and purpose of each dataset will be made clear in the following section.

May 26, 2006
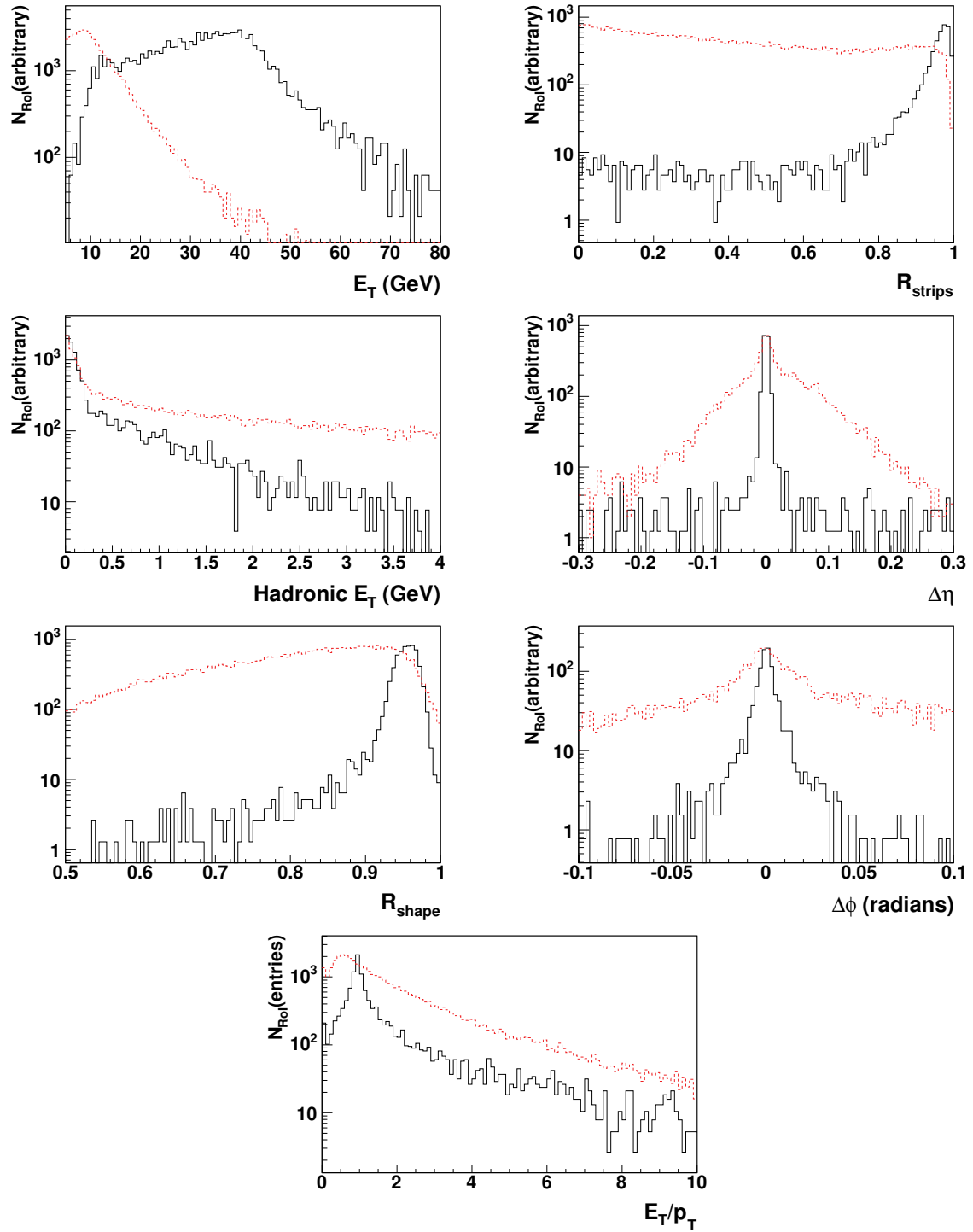
Figure 5.7: *Variables used for high-p_T electron identification at LVL2. Distributions are shown for electron candidates coming from $Z \to e^+e^-$ decays (solid line) and QCD di-jets (dotted lines).*

5.6 $Z \to e^+e^-$ Production Rates

One of the most important factors to determine when assessing the possibility of using $Z \to e^+e^-$ events as a way of determining the electron trigger efficiencies is

the rate at wich this events will be produced. As in any other counting statistics measurement, the amount of collected data will determine essentially its statistical uncertainty. Considering that $Z \to e^+ e^-$ candidates will be selected using the single electron trigger, and taking into consideration the kinematical and offline constraints discussed in the previous sections; their production rate can be calculated using the expression:

$$R = \sigma L (2\epsilon - \epsilon^2) A_Z \epsilon_{rec} \qquad (5.1)$$

where

- σ is the Zee production cross section

- L is the luminosity given by the accelerator

- ϵ is the overall single electron trigger efficiency (including LVL1). The term $2\epsilon - \epsilon^2$ represents the probability to trigger on one of the $Z \to e^+ e^-$ electrons.

- A_Z is the acceptance for the Z decay, which includes the efficiency for the kinematic cuts on the leptons and the geometric acceptance of the detector

- ϵ_{rec} is the efficiency for the Z to pass the offline selection criteria

In our case, the production cross-section, and the luminosity are those used by Pythia in the simulation of the $Z \to e^+ e^-$ physics channel. The efficiencies were calculated using Monte-Carlo based information. A summary of quantities used is given in the following lines:

$\sigma_{zee} = \sigma_{pythia}$	$1.515\,mb\ (1.515 \cdot 10^{-33}\,cm^2)$
ϵ	$\approx 76\%$
A_Z	$\approx 22\%$
ϵ_{rec}	$\approx 98\%$
Luminosity	$2 \times 10^{33}\,cm^{-2}\,s^{-1}$

Table 5.1: *Summary of the values used for the calculation of the Zee production rates*

Inserting these values into equation(5.1), the $Z \to e^+ e^-$ production rates at low luminosity is expected to be $\approx 0.5\,Hz$.

5.7 Extracting HLT Electron Trigger Efficiencies from Data

The $Z \to e^+ e^-$ physics channel is of common use nowadays by the high energy physics community for determining electron identification efficiencies. A common procedure exists in currently running experiments, (CDF or D0) that focuses mainly

on the offline identification performance [2] [3]. Only few variations deal with the trigger efficiencies [4] [5], but they assume a perfect trigger system functioning and therefore do not consider possible online(non-algorithmic) degrading factors that might affect the efficiency calculations, like buffer overflows, network related problems, etc. Given the complexity of the ATLAS TDAQ system, imposed by the very demanding LHC enviroment, these factors cannot be neglected.

The method described in this section adopts, essentially, some of the basic ideas cited above, but in addition, it propose to add specific online information to the reconstructed event, yielding a more realistic estimate of the HLT electron trigger performance.

The basic strategy is the following:

1. Apply a single e25i electron trigger signature to trigger on $Z \rightarrow e^+e^-$ candidates.

2. Flag online the events for which at least 2 electron candidates satisfy a given electron selection criteria. This flag could in principle be added after a full HLT level(i.e Level 2, or EF), or after a particular identification criteria (i.e energy deposition in the calorimeter, or calorimeter-tracking matching)

3. Obtain a $Z \rightarrow e^+e^-$ diagnostic sample using the procedure described in Section 4.5.

4. From the diagnostic sample, extract the events for which a flag was added. This will be the flagged sample.

5. Estimate the amount of $Z \rightarrow e^+e^-$ signal and background present in the diagnostic and flagged samples using a standard technique(fit, side-band, etc..)

As will be shown in the next subsection, using the estimated amount of signal and background in both the diagnostic and flagged sample, one can determine the HLT electron trigger efficiency for a given trigger level, or for a specific selection criteria (This will be determined by the position in the HLT selection chain where the flag is added).

5.7.1 Efficiency Calculation

Let us consider that the HLT system is configured to trigger on events containing at least one isolated high p_T electron, and that, under this condition, the LVL1 is also setup to select events containing at least one, high energetic electromagnetic cluster candidate.

After a certain acquisition time there will be N_0 events passing the LVL1 trigger, out of which a certain number N_Z^0 will be true $Z \rightarrow e^+e^-$ events, and the rest, B_0 are background:

$$N_0 = N_0^Z + B_0 \tag{5.2}$$

Considering that only one trigger level was applied and therefore the full rejection power is not yet achieved, B_0 will be the predominant term, containing mainly dijets events coming from minimum bias interactions;

Let us now assume the trigger efficiency(probability) ϵ, of selecting a high-p_T electron coming from a $Z \to e^+e^-$ event, to be statistically independent of whether the second one was accepted or not. Under these assumptions, the number of reconstructed events, N_1, with an invariant mass close to M_Z must yield:

$$N_1 = \epsilon_{rec}(2\epsilon - \epsilon^2)N_0^Z + B_1 \tag{5.3}$$

where

- $2\epsilon - \epsilon^2$ is the probability of accepting a Zee event if one triggers at least on one of the electrons of the Z;

- ϵ_{rec} is the offline Zee reconstruction efficiency;

- B_1 is the number of background events remaining after the full trigger chain, and for which the reconstructed invariant mass is close to M_Z;

- N_1 is the diagnostic sample.

Let us now assume that the HLT system offers the possibility of tagging all the information leading to the decision of whether an event should be rejected or not. In that case one could add a flag to the event data stream for those events for which 2 electron candidates satisfied the trigger electron identification criteria. The number of events, N_2, found in this case after the full reconstruction, for which, the invariant mass is close to M_Z is then a subset of N_1, and its value must be:

$$N_2 = \epsilon_{rec}\epsilon^2 N_0^Z + B_2 \tag{5.4}$$

where

- ϵ^2 is the probability of accepting a Zee event if one asks for two electron candidates.

- $B_2 = \epsilon^2 B_0$ is the same as B_1, but restricted to those events with a flag indicating that a second electron candidate passed the selection criteria.

- N_2 is the flagged sample.

The result is a system of two equations (5.3), and (5.4) with two unknowns: ϵ, and N_0^Z, from which one obtains the following expression for the efficiency(N_1, B_1, N_2, and B_2 can estimated experimentally):

$$\epsilon = \frac{2(N_2 - B_2)}{(N_1 + N_2) - (B_1 + B_2)} \tag{5.5}$$

May 26, 2006

Equation 5.5 can be further simplified to its final form considering that what one typically obtains from a fit procedure is $(N_1 - B_1)$, and $(N_2 - B_2)$.

$$\epsilon = \frac{2(\bar{N}_2)}{\bar{N}_1 + \bar{N}_2} \qquad (5.6)$$

where $\bar{N}_1 = N_1 - B_1$, and $\bar{N}_2 = N_2 - B_2$ represent the estimated amount of the true $Z \to e^+ e^-$ signal in respectively the diagnostic and flagged sample.

5.8   Efficiency Uncertainties

When estimating efficiencies from data, one is faced with the question of how to express the uncertainties on the estimate in a way that does not break down at the limits of small numbers or near the boundaries. This section gives a prescription for determining these uncertainties using the Bayesian formalism [6].

When determining efficiencies in high energy physics, whether for detector performance or signal event selection, one typically collects a number of trials (N) and successes (n), and estimates the efficiency from their ratio: $\epsilon = n/N$. This is a clear example of a binomial process; given N and the true value of the efficiency ϵ, the probability for n successes is governed by the binomial distribution:

$$P(n|N, \epsilon) = \frac{N!}{n!(N-n)!} \epsilon^n (1 - \epsilon)^{N-n} \qquad (5.7)$$

For many "runs" of N trials each, one finds that the observed n has a distribution with variance $N\epsilon(1-\epsilon)$ about the mean value $N\epsilon$. In a given run, then, one estimates the uncertainty on the estimate of ϵ as:

$$\sigma_\epsilon = \frac{\sigma_n}{N} = \sqrt{\frac{\epsilon(1-\epsilon)}{N}} \qquad (5.8)$$

While this definition makes some sense in the limit where the variance is correct, it clearly breaks down when n is near 0 or N. In those extremes, the distribution of observed n becomes very asymetric and at the limits, the calculated error vanishes. Clearly a more rigorous approach is desirable.

Starting from the binomial distribution in equation (5.8), the true value $\hat{\epsilon}$ for the efficiency is not known; rather, only n, and N can be determined experimentaly. The quantity that needs to be determined is therefore $P(\epsilon|n, N)$, which is the probability that the true efficiency is between ϵ and $\epsilon + d\epsilon$. Knowing this, one can determine the most probable value of ϵ, given the acquired data and also a confidence interval for it.

Baye's theorem offers the method for inverting a probability. In this context, the expression for $P(\epsilon|n, N)$ is:

$$P(\epsilon|n, N) = \frac{P(n|\epsilon, N)P(\epsilon)}{A} \qquad (5.9)$$

where A is a constant to be determined by normalization, and $P(\epsilon)$ is the probability one assigns for the true efficiency to be between ϵ and $\epsilon + d\epsilon$ before data taking. $P(\epsilon)$ is commonly known as the prior, and $P(\epsilon|n, N)$ as the posterior probability.

Considering that ϵ must be in the inclusive range [0,1], and the fact that, there is in principle no reason to favor one value of the efficiency over another[1]; a reasonable expression for the prior would be:

$$P(\epsilon) = \begin{cases} 1 & \text{if } 0 \leq \epsilon \leq 1, \\ 0 & \text{otherwise} \end{cases} \qquad (5.10)$$

Note that the use of probability theory allows to include in the calculation the knowledge that the efficiency must be between zero and one; this knowledge is built into the pre-data probability distribution describing the knowledge one has about ϵ, which assigns zero probability to those values of ϵ which are certanly known to be impossible.

With $P(n|\epsilon, N)$ given in equation (5.7), the normalization constant A, and thus the probability distribution describing post-data knowledge of ϵ can now be determined in a closed form solving the following equation:

$$\int_{-\infty}^{\infty} P(\epsilon|n, N)d\epsilon = \frac{\int_{-\infty}^{\infty} P(n|\epsilon, N)P(\epsilon)d\epsilon}{A}$$

$$= \frac{1}{A}\frac{N!}{n!(N-n)!}\int_{0}^{1} \epsilon^n(1-\epsilon)^{N-n}d\epsilon$$

$$= 1$$

Considering that the Beta function $B(x, y)$ is defined by $B(x, y) = \int_{0}^{1} t^{x-1}(1-t)^{y-1}dt$, and using the relation $B(x, y) = \Gamma(x)\Gamma(y)/\Gamma(x+y)$, the posterior probability density for ϵ is:

$$P(\epsilon|n, N) = \frac{\Gamma(N+2)}{\Gamma(n+1)\Gamma(N-n+1)}\epsilon^n(1-\epsilon)^{N-n} \qquad (5.11)$$

---

[1]This is a plausible argument if we do not have any previous knowledge about the prior (i.e. efficiency). This value should be updated once we have some knowledge about the prior(e.g. after a detector run).

May 26, 2006

Note the following:

- Zero probability is assigned when ϵ is zero or one.

- Zero probability is assigned to $\epsilon = 0$ unless $n = 0$; this is necessary, of course, since if there is a least one event passing the selection criteria, the efficiency can not be zero.

- Similarly, zero probability is assigned to $\epsilon = 1$ unless $n = N$, since if even a single event fails the selection criteria, then the efficiency can not be one.

Given the probability distribution for a certain parameter; the mean of it is actually a more practical estimator for the parameter than the value for which the probability distribution has a global a maximum. The maximum could lie at or near one end of the distribution, and thus not be representative of the distribution as a whole.

The posterior mean efficiency, is the expected value, or mean of the posterior distribution (equation (5.11)):

$$< \epsilon > = \int_0^1 \epsilon P(\epsilon|n, N)d\epsilon \tag{5.12}$$

$$= \frac{n+1}{N+2} \tag{5.13}$$

At this stage, one could replace the variables n, and N by the values derived in the previous section, equation (5.6), yielding:

$$< \epsilon > = \frac{2\bar{N}_2 + 1}{\bar{N}_1 + \bar{N}_2 + 2} \tag{5.14}$$

In other words, given that ones obtains $\bar{N}_1$, and $\bar{N}_2$ as the output of an experiment, bayesian statistics tells that the mean efficiency value will not be the "logical" frequentist one given by equation (5.6), but rather the value obtained in equation 5.14. Obviously, for the case in which $0 << \bar{N}_2 < \bar{N}_1$, both expressions will be equivalent, but the bayesian approach offers a better answer for the extreme cases in which $\bar{N}_1 \simeq \bar{N}_2$, and both quantities are relatively small.

Another information one wants to know about the posterior distribution is how spread out it is. If it has large spread, then, the knowledge about the efficiency, even after analyzing the data, will be still imprecise. There are many measures of this uncertainty that can be extracted from the distribution $P(\epsilon|n, N)$: upper and lower limits at various confidence levels; the variance, or its squared root, the standard

deviation, etc. The variance will be considered in this case, since for the posterior distribution (equation (5.11)), it can be determined analytically:

$$\sigma^2 = \int_0^1 (\epsilon - <\epsilon>)^2 P(\epsilon|n, N) d\epsilon \tag{5.15}$$

$$= \frac{(n+1)(N-n+1)}{(N+2)^2(N+3)} \tag{5.16}$$

$$= \frac{<\epsilon>(1-<\epsilon>)}{N+3} \tag{5.17}$$

Replacing the variables n, and N by the values derived in the previous section, and considering that:

$$\bar{N}_2 = \frac{<\epsilon>}{2-<\epsilon>}\bar{N}_1 \tag{5.18}$$

one obtains

$$\frac{\sigma^2}{<\epsilon>^2} = \frac{(1-<\epsilon>)}{<\epsilon>}\frac{2-<\epsilon>}{2}\frac{1}{\bar{N}_1} \tag{5.19}$$

According to this result, the final uncertainty on the calculated efficiency is only a function of the efficiency, and the the number of $Z \to e^+e^-$ signal events in the diagnostic sample. Figure (5.8) shows the distribution of $\frac{\sigma}{<\epsilon>}$ for a range of different expected efficiency values. According to the distributions, in 1 hour of data acquisition under the start-up luminosity conditions, one can collect enough $Z \to e^+e^-$ statistics so that the calculated HLT electron trigger efficiency has always a relative statistical error less than 3%.

5.9 Efficiency Studies Using $Z \to e^+e^-$ Monte-Carlo Data

The LVL2 single electron trigger performance was calculated using the $Z \to e^+e^-$ Monte-Carlo sample described in section 1.2.(no background present). This obviously represent an idealistic case, but it provides a first cross-check of wether the method provides satisfactory results or not. The efficiency was calculated by constructing plots of the reconstructed invariant mass of events that passed the e25i single trigger(the diagnostinc sample), and the invariant mass plots of events were, in addition, a flag was added after the LVL2 trigger chain, indicating that a least 2 electron candidates satisfied the single e25i electron trigger(the flagged sample). The total amount of signal and background for both distributions was estimated by a fit using a Breit-Wigner convoluted with a Gaussian and a linear background (the initial number of background events parsed to the fitting routine was set to zero) in
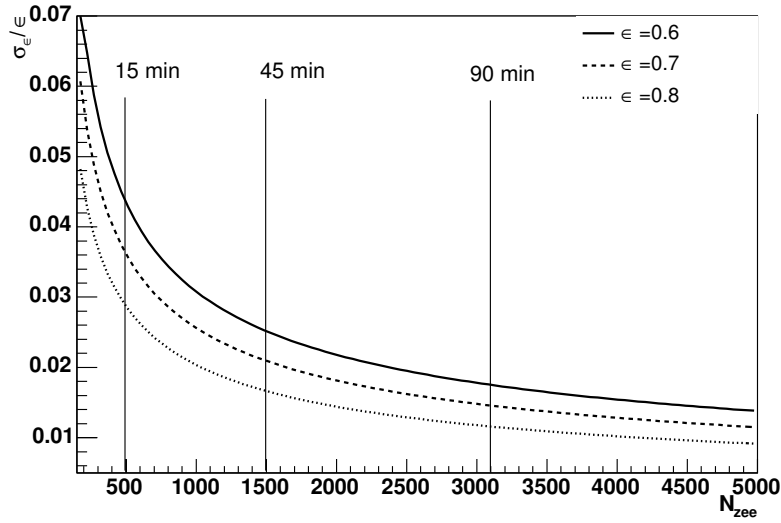
Figure 5.8: *relative error distribution on the calculated efficiency $((\sigma_\epsilon / < \epsilon >)^2)$ as a function of the number of real $Z \to e^+ e^-$ events reconstructed in the disgnostic sample for different HLT electron trigger efficiencies.*
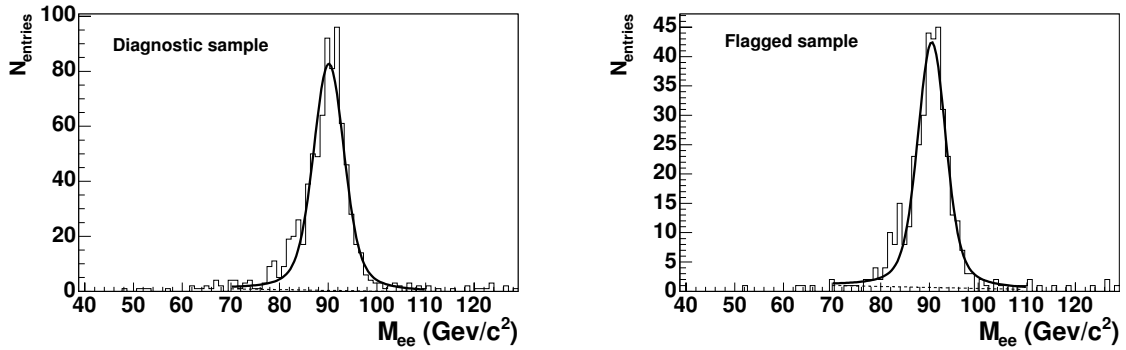
Figure 5.9: *Left: fitted invariant mass distribution of events that passed the LVL2 single inclusive e25i selection criteria. Right: fitted invariant mass of events passing the LVL2 e25i trigger criteria, and containing a flag, indicating that at least two electron candidates satisfied the LVL2 e25i trigger.*

the region $70 < M_{ee} < 110\,GeV$. Figure 5.9 shows the outcome of the fit for both the diagnostic and the flagged sample.

The number of signal events in the diagnostic and flagged sample was then found to be 2065, and 1590 respectively. Under the start-up, low luminosity conditions, this would represent ≈ 1 hour of data acquisition. Using these values, and considering equations 5.6 and 5.19, the calculated LVL2 single electron efficiency was 87.0 ± 0.5. This result is in agreement, within the statistical uncertainty, with the result obtained in Chapter 3, using single electrons and Monte-Carlo information. It suggest that, under ideal noise-free conditions, the single electron efficiency is well reproduced by the procedure described in 4.7.

For the $Z \rightarrow e^+e^-$ method to be fully validated, the efficiecny value given above should be reproduced under more realistic conditions, including the presence of background. The next subsection deals with this issue.

5.9.1 Effect of Background and Systematic Uncertainties

There are large theoretical and experimental uncertainties on the jet production rate and on the fraction of jets [7] which survive the electron identification criteria. These uncertainties are estimated to be:

- A factor ~ 2 on the production cross-section, due to higher order corrections, structure function parametrisations, choice of the Q^2 scale, etc.

- A factor ~ 1.5 per jet (determined with LEP data [8]), arising from limited knowledge of the hard tails of the parton fragmentation function (i.e. the probability for a parton to fragment into a particular hadron carrying a certain fraction of the parton's energy).

- A factor of ~ 2 per jet, coming from various uncertainties related to the detector response: knowledge of the detector geometry and of the amount of inactive material, physics processes in GEANT describing the interactions of hadrons in the calorimeters, etc.

These contributions add (quadratically) up to a total uncertainty of more than 5 on the jet-jet rate. Due to this large uncertainties in the final trigger rate, leading to unknown levels of background contribution to the $Z \rightarrow e^+e^-$ channel, it was considered more convinient not to estimate approximately what the final background will be, but rather, use the invariant mass distribution of QCD di-jets after the LVL1 trigger (Fig. 5.10) as a fairly good estimation of the final reconstructed background profile, and then, test the robustness of the method against arbitrary large levels of background contributions.

The di-jet contribution was normalized by a constant factor and added to the histograms bin content of the $Z \rightarrow e^+e^-$ diagnostic sample, so that it represents 5%, 10%, 20%, and 60% of the entries within the Z mass window. 60% was randomly chosen in this context as an upper, very improbable[2],limit.
The same procedure was applied for the flagged sample. In this case, the amount of background must always be less or equal than in the previous one, since for these events, a second electron passing the trigger selection is required. A direct relation between the levels of background in the diagnostic and flagged sample can be derived from Equation 5.5.

---

[2]In a recent result reported by the CDF collaboration [4]; for an integrated luminosity of $72.0\,pb^-1$, the background fraction under the $Z \rightarrow e^+e^-$ mass window is $\simeq 1\%$
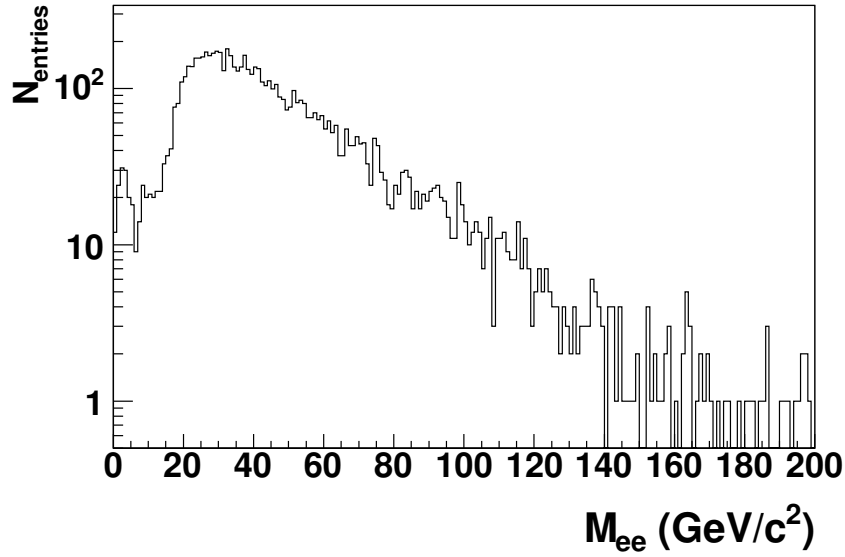
Figure 5.10: *Invariant mass spectrum of the QCD di-jet reconstructed sample after the LVL1 trigger. This profile was considered a good approximation to the final background shape after the full trigger chain plus offline reconstruction.*

Considering our efficiency to be 87.0%, the amount of signal and background events for both samples, was then estimated for every background configuration using a Gaussian convoluted Breit-Wigner plus a linear background fit (Fig. 5.11), and the single electron efficiency was calculated using these values. Table 5.2 summarize the amount of signal and background given by the fitting procedure for the different background scenarios. The calculated efficiencies and its associated uncertainties are also shown.
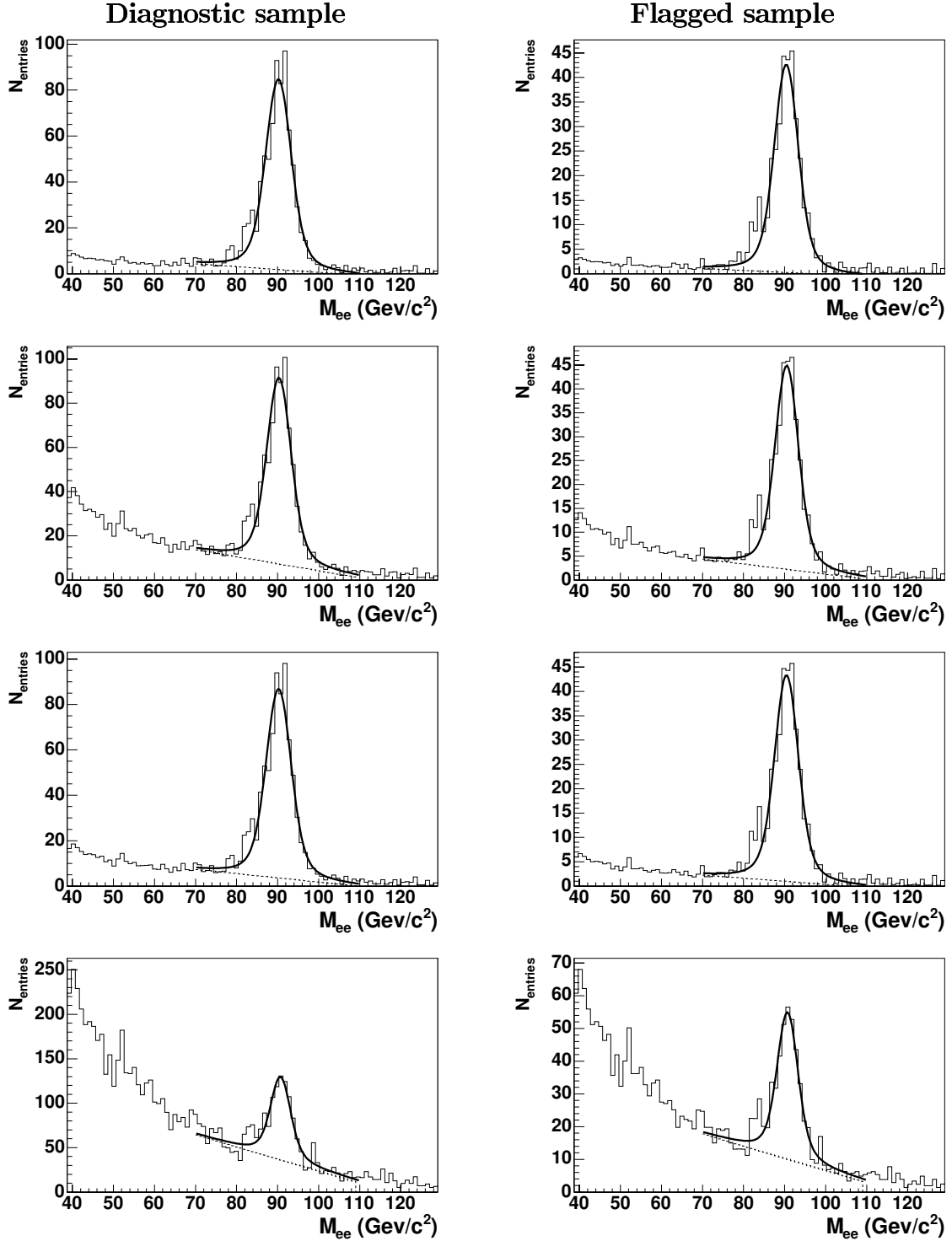
Figure 5.11: *Invariant mass distribution of the diagnostic (left column), and flagged (right column) sample under different background levels scenarios. The contribution from QCD dijet events was normalized so that it represents: 5% (4%), 10% (9%), 20% (17%), and 60% (52%) of the diagnostic (flagged) sample. The output of the fit is also shown.*

Background scenario		Calculated values		
B_1 (%)	B_2 (%)	$N_1 - B_1$	$N_2 - B_2$	$\epsilon(\%)$
0	0	2065	1590	87.0 ± 0.5
5	4	2063	1588	87.1 ± 0.5
10	9	2056	1586	87.2 ± 0.6
20	19	2052	1584	87.1 ± 0.8
60	59	1998	1569	87.5 ± 0.9

Table 5.2: Summary of the background-substracted signals obtained from the fitting routine. Results are shown for the different background configurations, and they include the calculated single electron efficiency in each case.

According to this values, the calculated efficiencies (for an equivalent of ≈ 1 hour of data acquisition) were the same in each case, within the statistical uncertainty, and do not vary as a function of the background.

A systematic error contribution is to be expected for the calculated efficiency ϵ (Equation 5.5), due to the background subtraction mechanism used. In order to quantify this uncertainty, four methods were used to determine the signal and background contribution in both, the diagnostic, and the flagged $Z \to e^+e^-$ sample:

A. A sideband averaging technique. Lower and upper sideband regions are defined outside the signal region of $86 < M_{ee} < 96\,GeV$ in order to estimate the amount of background. The lower sideband region is $60 < M_{ee} < 70\,GeV$ and the upper sideband region is $110 < M_{ee} < 120\,GeV$. These regions are chosen to be symmetric about the signal region, and cover the same range in invariant mass. The number of background events is then taken to be the average of the two sideband regions;

B. Method A is repeated for a signal region $80 < M_{ee} < 100\,GeV$. With this signal region the number of background events is taken to be the sum of the two sideband regions.

C. The dielectron mass spectrum is fitted using a Breit-Wigner convoluted with a Gaussian (to account for the resolution in the measurement) and a linear background in the region $70 < M_{ee} < 110\,GeV$. The linear fit parameters are then used to estimate the number of background events which must be subtracted out. The signal window is $86 < M_{ee} < 96\,GeV$;

D. Method C is repeated for a signal window $80 < M_{ee} < 100\,GeV$

Figure 5.12 illustrates the background subtraction methods used in this study.

An exponential shape for the background was also used as a check, and the efficiencies resulting from such a fit agree well within the corresponding uncertainties. Table 5.3 summarizes the four method employed.
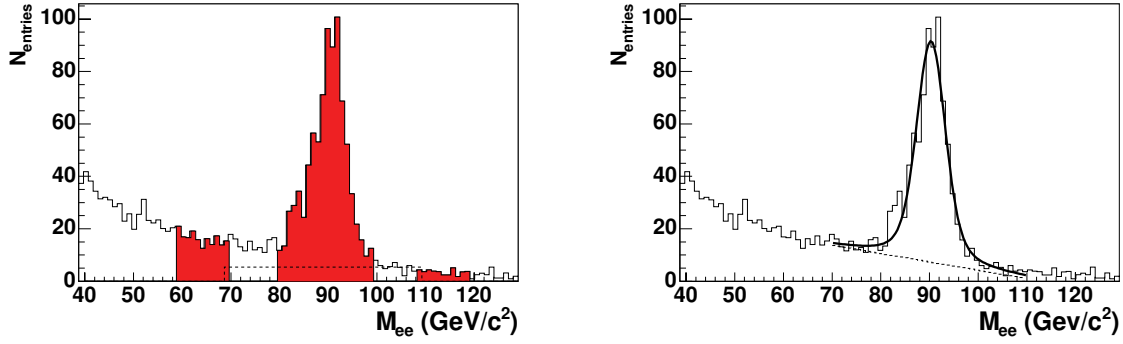
Figure 5.12: *Illustration of the background substraction method used in the determination of electron identification efficiencies. Sideband technique (top), and fit technique (bottom). The dashed line shows the estimated background.*

Method	Background Subtraction	Signal Region
A	Sideband [60-70][110-120]GeV	$86 < M_{ee} < 96\,GeV$
B	Sideband [60-70][110-120]GeV	$80 < M_{ee} < 100\,GeV$
C	$BW \otimes G$ + Linear fit	$86 < M_{ee} < 96\,GeV$
D	$BW \otimes G$ + Linear fit	$80 < M_{ee} < 100\,GeV$

Table 5.3: Summary of the background subtraction methods used in estimating electron selection efficiencies

The results obtained with each background substraction mechanism are summarized in Table 5.4 for the different methods used. The systematic error contribution to the calculated efficiency was taken to be half the maximum difference between the various methods. According to these values, an upper limit to the systematic error due to different background substraction methods used can be set to 1.0%.

Method	Calculated values		
	$N_1 - B_1$	$N_2 - B_2$	$\epsilon(\%)$
A	2043	1570	86.9 ± 0.9
B	2346	1806	87.0 ± 0.8
C	1998	1569	87.5 ± 0.9
D	2252	1757	87.7 ± 0.8

Table 5.4: Summary of the background substracted signals obtained from each method under the worst background configuration. The calculated single electron efficiency is shown for each case.

5.10   Conclusions

A new procedure to estimate the HLT electron trigger efficiency using $Z \rightarrow e^+e^-$ data was described in this chapter. This method was tested on a $Z \rightarrow e^+e^-$ Monte

Carlo sample resulting in an efficiency of 87.0% for the particular set of cuts used in the e25i signature. The same value was found by counting simulated events selected by this signature. Moreover, assuming an instantaneous luminosity of $10^{33}\,cm^{-2}\,s^{-1}$, for a $Z \rightarrow e^+e^-$ cross section of 1.515 nb, the method can provide an estimate for the overall electron trigger efficiency with a statistical uncertainty of less that $\sim 3\%$, after 1 hour of data acquisition.

The robustness of the method was tested against different levels of background contribution. The QCD di-jet reconstructed invariant mass profile, assumed to be the main source of noise, was normalized to arbitrary large values so that it represented up to 60% of the signal under the $Z \rightarrow e^+e^-$ mass window. For the equivalent of ~ 1hour of data acquisition, the calculated efficiency was found the same, within the statistical uncertainty, for each background scenario. In addition, an upper limit to the systematic error contribution due to different background substraction methods was found to be $\sim 1.0\%$, and therefore it is not expected to countribute significantly to the overall uncertainty.

Bibliography

[1] ATLAS collaboration, ATLAS Data Challenge DC1, ATL-SOFT-2003-012, (2003).

[2] R. Demina et al., Track Finding Efficiency Study Using $Z \to e^+e^-$ Sample. D0 Note 4050.

[3] M. Coca, E. Halkiadakis, Central Electron Identification EWfficiencies for the $200\,pb^{-1}$ Run 2 Dataset. CDF Note 6580, January 2004.

[4] G. Manca, YK. Kim, Z^0 Cross Section Measurements Using Run II Electrons, CDF Note 6281, March 2003.

[5] M. Cooke, Y. Maravin, Efficiency Study of the Central Track Trigger in $Z \to e^+e^-$ Events. D0 Note 4342, February 2004.

[6] William M. Bolstad, Introduction to Bayesian Statistics, ISBN 0-471-27020-2

[7] F. Gianotti and I. Vichou, ATLAS Note PHYS-No-78, (1996).

[8] O. Adriani et al. (L3 Collaboration), Phys. Lett. B 292(1992) 472.

Chapter 6

Performance of the Second Level Trigger Electron Selection Algorithms with the 2004 ATLAS Combined Test Beam Data

6.1 Introduction

Excellent particle identification is one of the most important design criteria for the ATLAS experiment. The ATLAS Liquid Argon (LAr) electromagnetic (EM) calorimeter together with the Inner Detector (ID) system are designed to identify photons and electrons in a wide energy range. Good electron identification and electron/pion (e/π) separation capability are especially critical in the low momentum range, where a large number of pions produced in proton-proton collisions at 14 TeV are expected. A fraction of hadronic showers may be fully contained within the EM calorimeter, creating a potential source of particle misidentification.

After the First Level Trigger (LVL1), the Second Level Trigger (LVL2) system has a critical role in the EM identification performance. Indeed, the trigger must be able to select electrons in a very efficient manner, while keeping the background rate to a minimum.

In this chapter, the e/π separation in the LVL2 system has been studied using test beam electrons and pions at momenta of 20 and 50 GeV/c. The results of this analysis are important, since this is the first and only occasion that a full slice of ATLAS has been assembled and tested before the full ATLAS detector becomes operational.
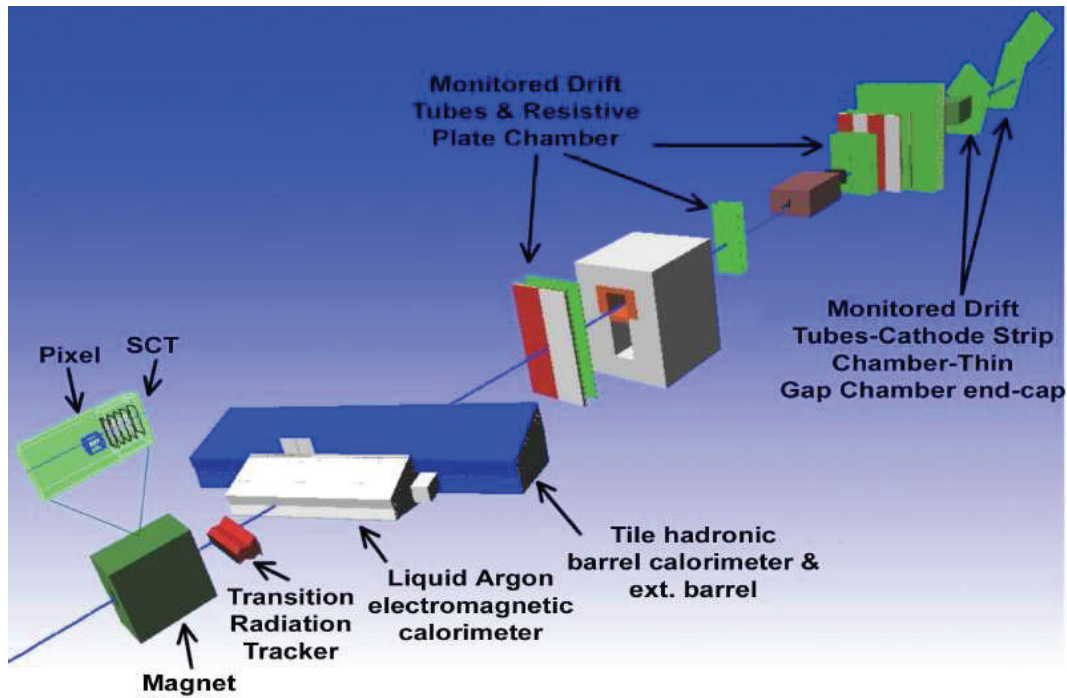
Figure 6.1: Schematic view of the experimental setup in the CERN H8 area.

6.2 The 2004 Combined Test Beam Experimental Setup

Test beam periods are of great importance during the research and development period of a detector, since they represent a great opportunity to face and solve unexpected problems that might arise in a later stage of the detector operation. The Combined Test Beam (CTB) activity carried out between the spring and fall of 2004 was particularly important, because small sections of all the ATLAS subdetectors using final or quasi-final readout electronics were integrated altogether for the first time with the Trigger and Data Acquisition system (TDAQ). A schematic view of all detectors installed in the CERN H8 beam line is shown in Fig. 6.1. A detailed description of the experimental setup in the CTB can be found in Ref. [1].

The CERN $400 - 450\,\text{GeV}$ Super Proton Synchrotron (SPS) provides either secondary or tertiary beams to the H8 beam line. A primary proton beam is extracted from the SPS towards the CERN North areas and directed onto the primary target. The magnets located after the primary target provide the momentum selection for the secondary beam that contains mostly pions. Electrons are obtained in tertiary beams. The H8 beam line provided electron and pion beams with a momentum range from 2 to $250\,\text{GeV/c}$.

6.2.1 ATLAS subdetectors in the CTB

Small parts of the following subdetectors were installed (see Ref. [2] for a detailed description of the technologies used in the detectors):

- **Inner detector**: three pixel layers, four SCT layers, two TRT barrel wedges;

- **Calorimetry**: two barrel modules of LAr EM calorimeter, and six modules of the hadronic Tile Calorimeter (TileCal), three barrel and three extended barrel modules.

- **Muon spectrometer**: six barrel MDT chambers, installed on three rails, reproducing one barrel alignment tower. Six end-cap MDT chambers installed on three large structures, reproducing the end-cap octant geometry.

The ID and calorimetry detectors are the first elements of the combined ATLAS assembly along the beam line. The pixel and SCT layers are placed within a bending magnet, providing a magnetic field of about 1.4 T; the distance between the last pixel layer and the first SCT layer is the same as in ATLAS ($\simeq 175$ mm). The next element along the beam is the TRT system, at a distance of about 55 mm from the last layer of the SCT. This distance is larger than the one designed for ATLAS (40 mm) due to the extension of the coils outside the MBPS magnet [3]. The TRT subdetector is followed by the LAr EM calorimeter and the TileCal. The distance between the last TRT layer and the LAr calorimeter is about 782 mm. Following the beam line a magnet for bending the tracks in the horizontal plane and then the detectors of the muon spectrometer [4] (RPC, MDT, and TGC chambers) are found. The distance between the TileCal and the first component of the muon spectrometer is about 28 m.

To ensure the compatibility of the test beam data with the ATLAS general software framework, the slice assembled in H8 has been corresponded by convention to sector one in η and sector one in φ, as shown by the yellow area in Fig. 6.2.

The reference frame for the whole experimental setup is shown in Fig. 6.3 (the gray plane represents a generic subdetector layer). The beam goes through the different subdetectors (from left to right) along the X axis; the Y axis goes up vertically and the Z axis direction completes the right-handed reference. All the distances are referred to the interaction point, which is 50.5 mm from the first pixel layer.

6.2.2 Trigger and DAQ System

During the CTB, the latest prototype of the ATLAS TDAQ system was used for the data taking of all the subdetectors. All ATLAS subdetectors need their own detector-specific DAQ development. The readout electronics is controlled by a Readout Driver (ROD), custom-built electronics board for each subdetector. The ROD
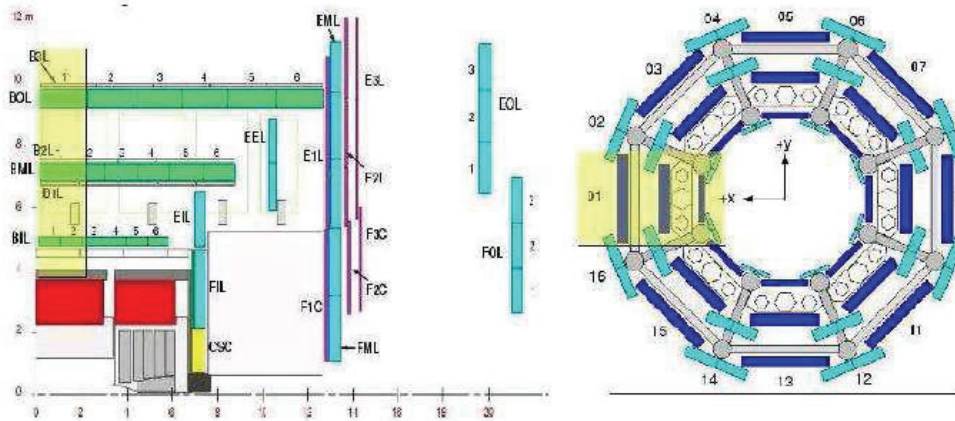
Figure 6.2: The H8 slice referred to the ATLAS reference frame.

receives data events that are accepted by the LVL1. The detector-specific part of the DAQ system needs to control the ROD and respond to commands of the central DAQ (e.g. "Start of run"). The ROD module sends event data to a Readout System (ROS). The LVL2 runs specific algorithms in a computer farm. It can request portions of data from different detectors in order to make the decision. During the CTB, it was always running in "spy" mode and was not filtering events. The data fragments received from the ROS are collected by the SubFarm Input (SFI) application and sent to the Event Filter (EF) system. After this step, without modification or filtering, the SubFarm Output (SFO) stores them in a local disk. Finally, output files are transferred to a mass storage system (CASTOR). Their data format is very similar to the one expected in ATLAS in 2007. Figure 6.4 shows an schematic view of the TDAQ setup during the CTB, indicating also the connections to the monitoring computers and other services. Around 90 PCs and Single Board Computers were used.

Further development of the TDAQ subsystems that has taken place afterwards has benefited from the direct experience of the system integration during the test
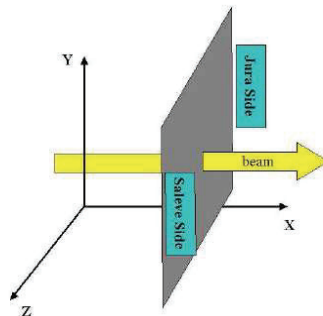
Figure 6.3: The H8 Reference Frame.
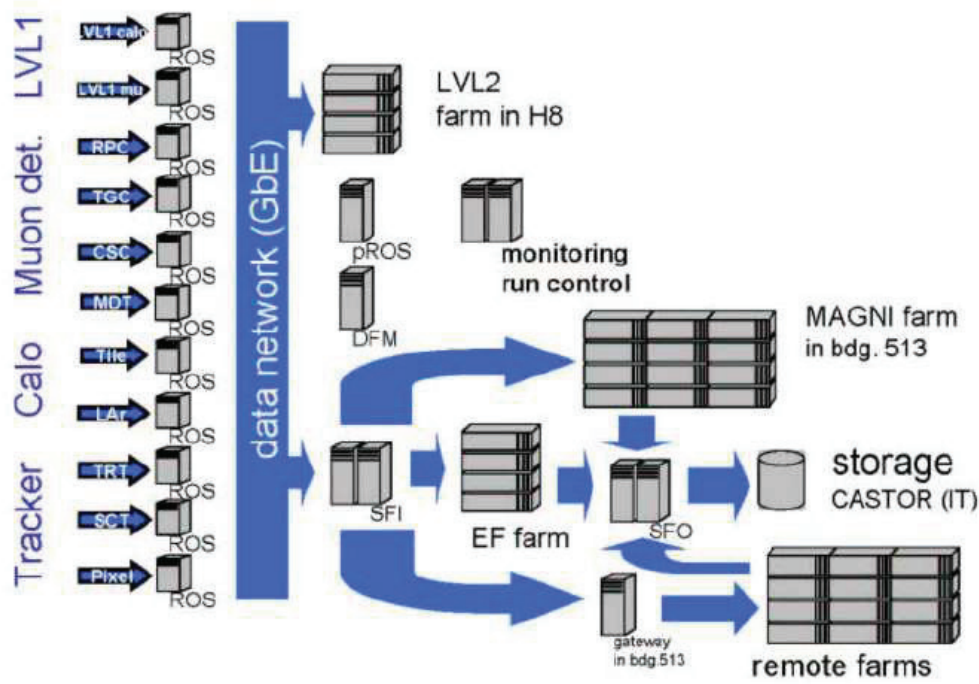
Figure 6.4: Schematic diagram of the TDAQ setup in the CTB. Around 90 PCs and Single Board Computers were used to manage the flow of data, test event selection algorithms, and provide control and monitoring.

beam period. Most ATLAS subdetectors, representing seven technologies from inner tracking to calorimeters and muon chambers, were integrated with the TDAQ and participated in the CTB runs.

6.3   Pre-selection of Electrons and Pions

The secondary beam entering the H8 beam line contained a mixture of mainly charged pions and photons (from π^0 decays). Pion beams were obtained by inserting a lead plate to absorb the photons followed by magnetic optics to select particles of equal energy. The electron beams were obtained by inserting a copper plate into the beam line where e^+e^- pairs are formed in photon conversions. The magnetic optics following the converter was used again to select particles of equal energies. The optics system was optimized for particles with interaction point at the copper plate, but still, some pion contamination in the electron beam was unavoidable.

Table 6.1 gives a summary of the runs used in the study presented in this note. These runs contain around 10^4 particles and have been selected according to the particle type (electrons or pions), their energy (20 or 50 GeV) and the requirement that the first magnet (where the ID was installed) was switched on. Unfortunately, during the complete CTB data-taking period, there was no pion run taken at 50 GeV with this magnet on. The implications of this to the performance studies presented in this note are explained in Sec. 6.4.
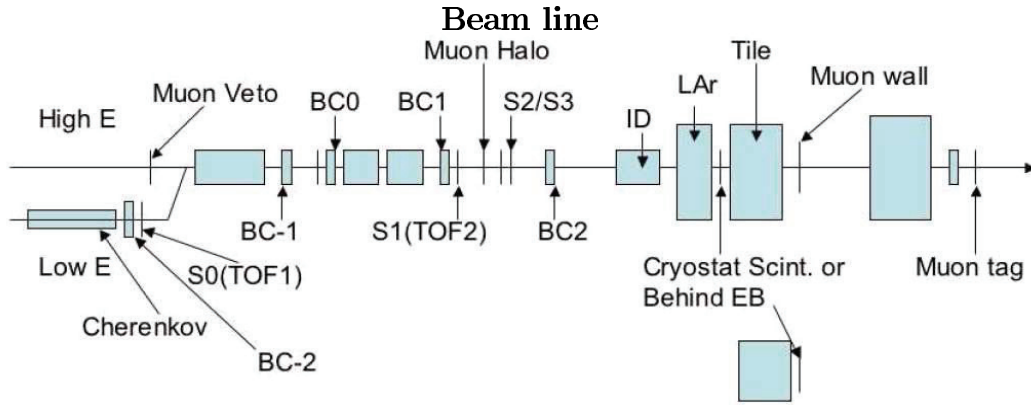
Figure 6.5: Drawing of the H8 beam line element layout. The dimensions are not in scale and the elements are represented by blocks.

E(GeV)	Nominal Beam	Run Number	No. of Events
20	e	2102413	10^4
20	π	2102389	10^4
50	e	2102400	10^4
50	π	2102350	10^4

Table 6.1: Summary of test beam data events used for this study. The beam energies and the dominant beam content is shown for each case. All the runs have the first magnet on except the one of π at 50 GeV.

Before the LVL2 e/π separation performance can be assessed, it is necessary to have a good identification of electrons and pions that can be provided by detectors that are not used by the LVL2 algorithms.

Among the different devices present in the experimental area (see Fig. 6.5), the following ones have been used to select a pure sample of electrons and a pure sample of pions: a pressure gas (filled with Helium) Cherenkov counter, situated at the beginning of the beam line element layout and suitable for e/π separation up to 50 GeV energy, a muon tag scintillator located at the far end of the beam line, and the TRT subdetector. Even though the TRT is not a beam filtering device, it can be used in this study because the HLT selection performance is only studied considering the Pixel, SCT and calorimeter systems.

The signal from the muon tag scintillator situated in the muon area, downstream the beam line, is used first to remove the muon contamination. Figure 6.6 shows the signals in the scintillator for electron and pion beams at different energies. Events with a signal in the muon tag scintillator greater than 480 ADC counts are considered as muons, and therefore excluded from the analysis. As it can be observed, and according to this selection criteria, the muon contribution to these datasets is in general very small, being more important in the 50 GeV pion beam.

The TRT subdetector is used to identify electrons and pions. The criteria applied
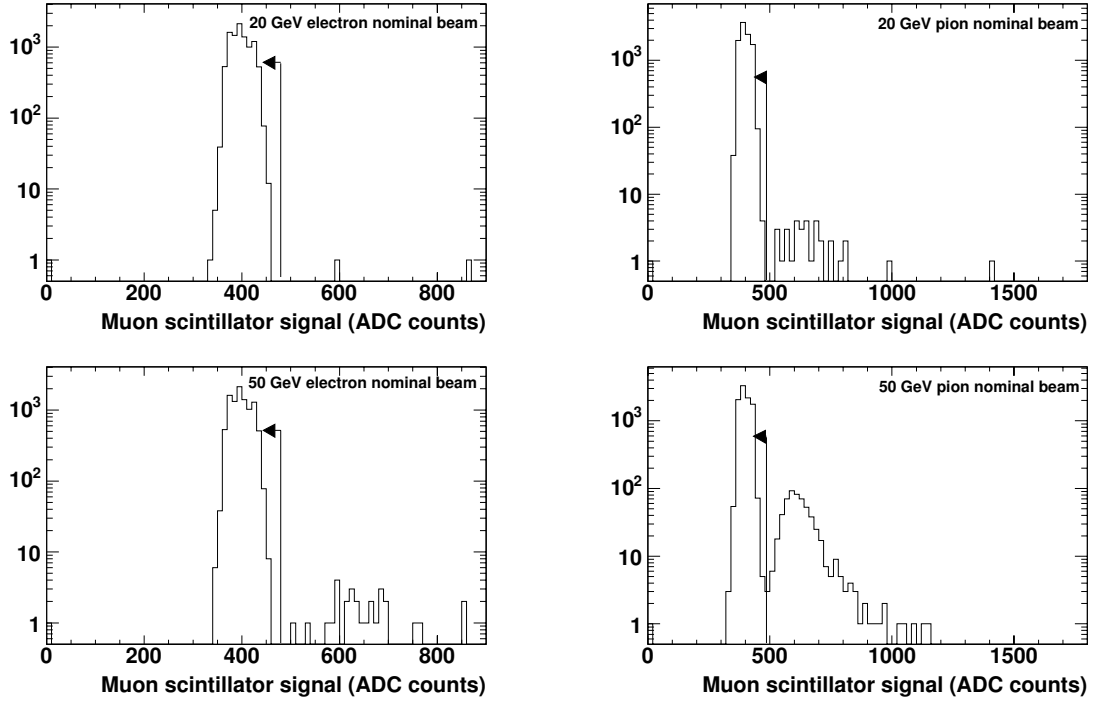
Figure 6.6: Signal distributions (in ADC Counts) in the muon tag scintillator for nominal beams of 20 and 50 GeV electrons and pions.

are the following:

- Selection of good tracks: only the events with one and only one reconstructed track in the TRT are considered. In addition, the number of hits in the track has to be greater than 25. This applies equally to both the electron and pion samples.

- Cut on the number of high level (HL) hits (transition radiation hits) in the track; for electrons, the energy deposition in the TRT straws is dominated by transition radiation hits, while for pions, it is mostly due to δ-rays. Electrons are required to have a track with more than seven HL hits while pions are required to have less than three. Figure 6.7 shows the number of HL hits for pions and electrons for both 20 and 50 GeV beams.

After the TRT filtering, little pion contamination remains in the electron sample and vice versa. The Cherenkov detector is then used to further clean up the electron and pion samples. Electrons are required to have more than 800 ADC counts in the Cherenkov detector. The opposite criteria is used to select pions. Figure 6.8 shows the signal of the Cherenkov detector for electrons and pions already pre-selected by applying the criteria of TRT and muon tag. As it can be observed, the Cherenkov selection performance is worse at 50 GeV than at 20 GeV.

The effect of all the previously defined selection criteria is shown in Fig. 6.9, where the scatter plots of the signal in the LAr EM calorimeter and the Tile hadronic
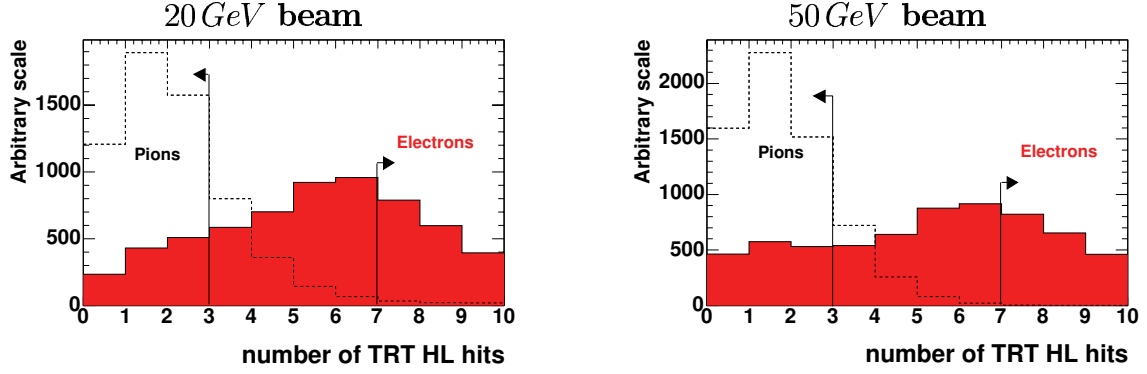
Figure 6.7: The number of High Level (HL) hits of the reconstructed tracks in the TRT subdetector. Distributions are shown for all events satisfying the good track condition criteria for nominal beams of electrons (shaded) and pions.
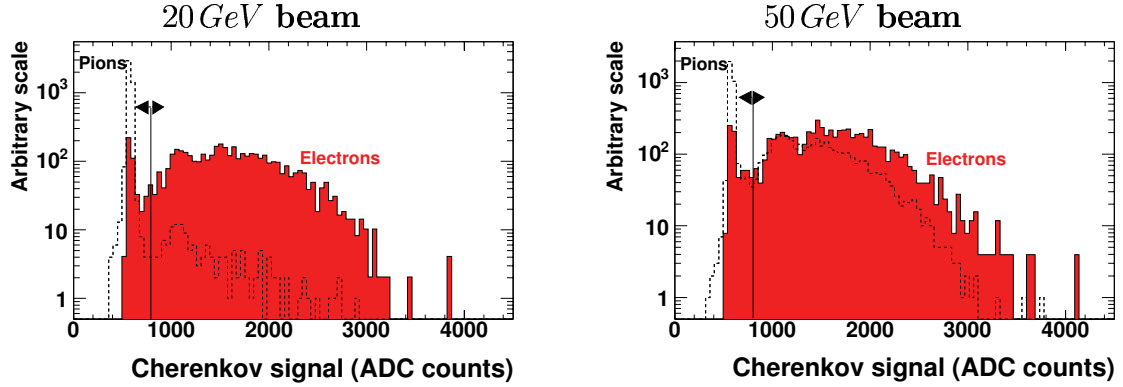
Figure 6.8: Signal distribution in the Cherenkov detector for nominal beams of electrons (shaded) and pions. Only events satisfying The TRT and muon tag filtering criteria are shown.

calorimeter for nominal beams of 20 and 50 GeV electrons and pions are shown, before and after beam filtering. As it can be observed, very little contamination remains in both samples after the selection. The final number of events in each sample after this pre-selection is ~ 2500.

6.3.1 Purity Calculations

A good estimation of the purity of the pre-selected samples is needed in order to compute the LVL2 trigger efficiency. The purity of an electron (pion) sample can be estimated in this context if one knows the fraction of pions (electrons) present in the sample. In that sense, the probability of finding electrons using the particle filtering cuts for pions ϵ_e^π, and the probability of finding pions using the particle filtering cuts for electrons ϵ_π^e, are the two important numbers to determine.

ϵ_e^π is best measured in a beam of predominantly electrons, and an upper limit can be calculated assuming the signals in the Cherenkov counter and the TRT are independent, which is the case here. The efficiency for finding electrons when making cuts for pions is:

Figure 6.9: Correlation plots of the signal in the LAr EM calorimeter and the Tile hadronic calorimeter for nominal beams of 20 and 50 GeV electrons and pions. The plots are shown before (left column) and after (right column) beam filtering.

$$\epsilon_e^\pi = (\epsilon_e^\pi)_{TRT}(\epsilon_e^\pi)_{Ch} \tag{6.1}$$

with $(\epsilon_e^\pi)_{TRT}$, and $(\epsilon_e^\pi)_{Ch}$ the probabilities for the TRT and the Cherenkov counter to misidentify a pion as an electron. It is, nevertheless possible to estimate an upper limit by setting up a system of equations using the following set-ups:

A Pion identification cuts in both the Cherenkov counter and the TRT.

B Pion identification cut in the Cherenkov counter, and electron identification cut in the TRT.

C Electron identification cut in the Cherenkov counter, and pion identification cut in the TRT.

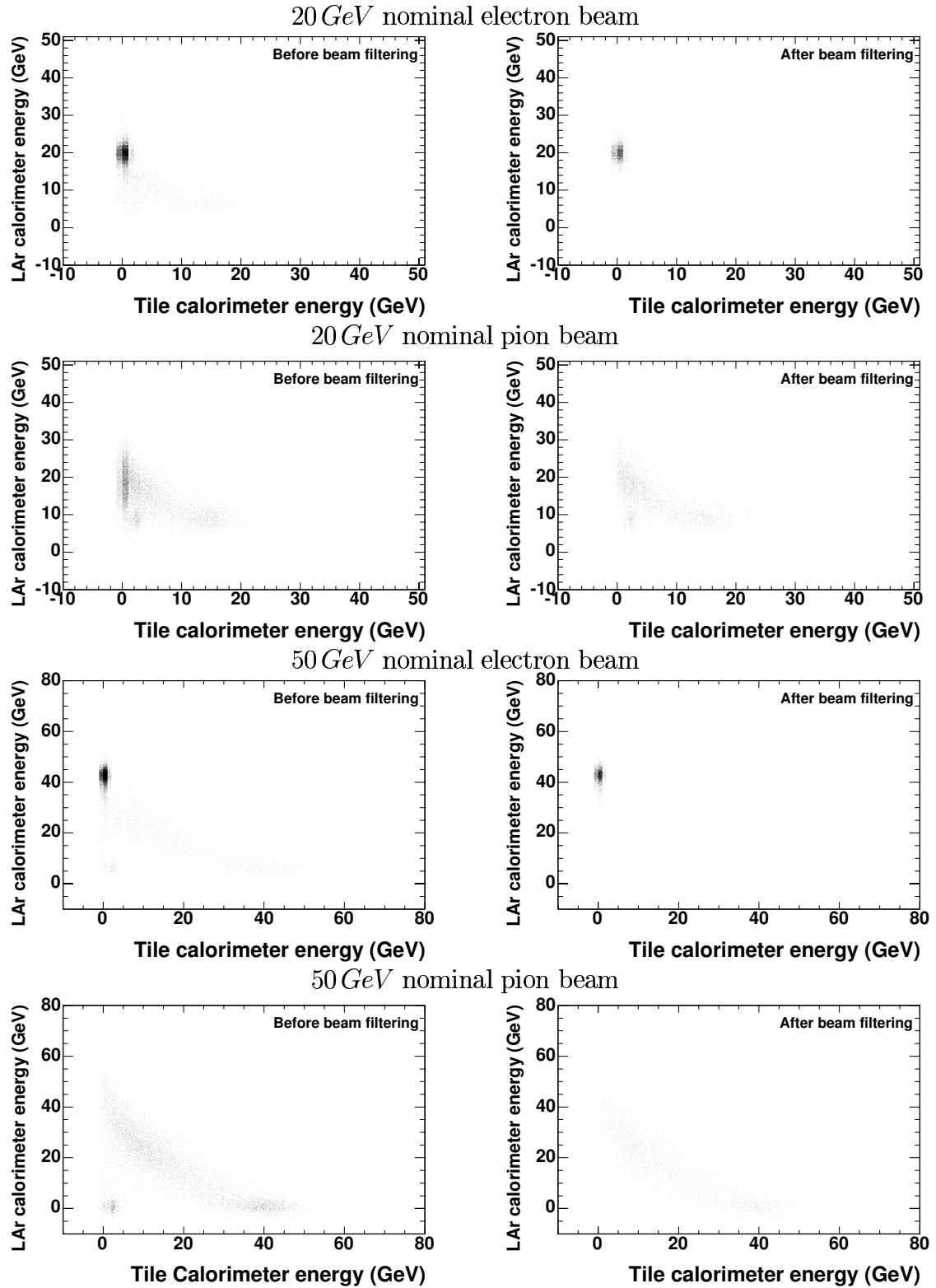**D** Electron identification cuts in both the Cherenkov counter and the TRT.

E Pion identification cut in the Cherenkov counter, and TRT selection cuts for anything other than an electron or a pion.

F Electron identification cut in the Cherenkov counter, and TRT selection cuts for anything different than an electron or a pion.

With X_e and X_π defined as the number of electrons and pions after the selection criteria X, the total number of particles X_{total} is given as (assuming that no muons are left after the Muon tag filter):

$$X_{total} = X_e + X_\pi = xX_e \quad , \text{ where } x > 1 \tag{6.2}$$

Since the cuts on the Cherenkov counter and the TRT are independent, one can write the following equations:

$$C_e = (\epsilon_e^e)_{Ch}(\epsilon_e^\pi)_{TRT}N_0$$
$$D_e = (\epsilon_e^e)_{Ch}(\epsilon_e^e)_{TRT}N_0$$
$$F_e = (\epsilon_e^e)_{Ch}(\epsilon_e^o)_{TRT}N_0$$

where N_0, and $(\epsilon_e^o)_{TRT}$ are the initial number of electrons in the nominal electron beam, and the probability that an electron pass the TRT cuts for anything other than an electron or a pion (This is needed due to the fact that the cut in the TRT is not an OR statement). $(\epsilon_e^\pi)_{TRT}$ can be the factored out (considering that $(\epsilon_e^\pi)_{TRT} + (\epsilon_e^e)_{TRT} + (\epsilon_e^o)_{TRT} = 1$), giving:

$$(\epsilon_e^\pi)_{TRT} = \frac{C_e}{C_e + D_e + F_e} = \frac{1}{1 + \frac{D_e}{C_e} + \frac{F_e}{C_e}} \tag{6.3}$$

The fraction of pions in region D and F will be lower than in region C, so $\frac{c}{d} > 1$,

May 26, 2006

and $\frac{c}{f} > 1$. Using the notation from 6.2, and inserting this in 6.3 results in an upper limit on the efficiency

$$(\epsilon_e^\pi)_{TRT} = \frac{1}{1 + \frac{cD}{dC} + \frac{cF}{fC}} < \frac{1}{1 + \frac{D}{C} + \frac{F}{C}} \qquad (6.4)$$

The analysis of $(\epsilon_e^\pi)_{Ch}$ and $\epsilon_\pi^e < (\epsilon_\pi^e)_{TRT}(\epsilon_\pi^e)_{Ch}$ are similar to the calculation of $(\epsilon_e^\pi)_{TRT}$, yielding:

$$(\epsilon_e^\pi)_{Ch} = \frac{1}{1 + \frac{aC}{cA}} < \frac{1}{1 + \frac{C}{A}}$$

$$(\epsilon_\pi^e)_{TRT} = \frac{1}{1 + \frac{bA}{aB} + \frac{bE}{eB}} < \frac{1}{1 + \frac{A}{B} + \frac{E}{B}}$$

$$(\epsilon_\pi^e)_{Ch} = \frac{1}{1 + \frac{dB}{bD}} < \frac{1}{1 + \frac{B}{D}}$$

The results are summarised in Table 6.2.

$20\,GeV$	$\epsilon_e^\pi < (\epsilon_e^\pi)_{TRT}(\epsilon_e^\pi)_{Ch} < 0.072 \cdot 0.063 = 4.5 \cdot 10^{-3}$
	$\epsilon_\pi^e < (\epsilon_\pi^e)_{TRT}(\epsilon_\pi^e)_{Ch} < 0.0042 \cdot 0.16 = 6.6 \cdot 10^{-4}$
$50\,GeV$	$\epsilon_e^\pi < (\epsilon_e^\pi)_{TRT}(\epsilon_e^\pi)_{Ch} < 0.053 \cdot 0.17 = 8.7 \cdot 10^{-3}$
	$\epsilon_\pi^e < (\epsilon_\pi^e)_{TRT}(\epsilon_\pi^e)_{Ch} < 0.00099 \cdot 0.62 = 6.2 \cdot 10^{-4}$

Table 6.2: *Upper limits in the probability of finding electrons using the particle filtering cuts for pions and vice versa. The values are calculated separately for both the 20, and 50 GeV samples.*

An upper limit on the amount of electrons in the pion beam before the particle identification is given by the fraction of events passing selection criteria D in the pion beam, scaled with the fraction of electrons passing this selection criteria (estimated from the electron beam). The electron contamination in the pion beam of $20\,GeV$ ($50\,GeV$) is 4.5% ($\sim 0.1\%$), while the pion contamination in the electron beam at both energies is $\sim 19\%$. The results are summarised in table 6.3

6.4   LVL2 e/π Separation Performance

In this section, the study of the e/π separation at LVL2 is presented. The samples used are specified in the previous section. Electron and pion samples of 20 and 50 GeV are used. As presented in Table 6.3, with a very good approximation, the samples can be considered pure and consisting of a single Region of Interest (RoI) per event, containing electrons and charged pions.

	Maximum fraction before selection		Maximum fraction after selection	
	20 GeV (%)	50 GeV (%)	20 GeV (%)	50 GeV (%)
electrons in pion beam	4.5	8.7	$2.9 \cdot 10^{-3}$	$5.4 \cdot 10^{-2}$
pions in electron beam	18.7	18.5	$8.3 \cdot 10^{-2}$	0.16

Table 6.3: Values of the purity of the samples used for the HLT electron identification studies. They are call alculated after applying the muon tag identification criteria. The left and right columns show the maximum fraction of electrons (or pions) into the pion (electron) samples, before and after applying the identification criteria using the Cherenkov and TRT detectors.

6.4.1 LVL2 Electron Trigger Selection

All algorithms at LVL2 are seeded by the information coming from RoI identified by the LVL1 trigger. Since the simulation of the LVL1 trigger is not used in this study, in order to seed the LVL2 trigger, a fixed LVL1 RoI with the $\eta - \phi$ position of the beam (as specified in the online database) is used. The LVL1 RoI is then transferred to T2Calo [5,6], the algorithm used at LVL2 to analyze the calorimeter information. T2Calo has access to the full calorimeter granularity and an improved energy calibration. It first retrieves the calorimeter data around the $\eta - \phi$ position given by the LVL1 RoI and constructs a cluster, which is used to compute several variables suited to discriminate electrons from hadrons or jets. Afterwards, the algorithm IDSCAN [7] is executed. This algorithm retrieves data around the RoI from the Pixel and SCT detectors and reconstructs track segments. In the events pre-selected for this study (described in Sec. 6.3) only one track is reconstructed by IDSCAN.

The cluster and track reconstructed by T2Calo and IDSCAN respectively, are used to select electrons based on the following variables:

- E_T^{EM} (transverse energy in the EM calorimeter): EM showers initiated by electrons are expected to be fully contained in the EM calorimeter. The hadronic showers start deeper in the calorimeter system and there is often a substantial fraction of the total energy shower that leaks into the hadronic calorimeter. Figures 6.10 a) and b) show the distribution of the Transverse Energy deposited in the EM Calorimeter for electrons (full line) and pions (dotted line) of 20 and 50 GeV respectively. Figures 6.10 c) and d) show the electron and pion efficiency of an E_T cut for the two energies under consideration. It can be clearly seen that the energy deposited by electrons in the second sampling of the EM calorimeter peaks at values below, but close to the nominal particle energy, while the distribution for pions extends to low energy values. The arrows in Figs. 6.10 a) and c) indicate the selected region in E_T^{EM} in order to obtain the performance numbers specified in Sec. 6.4.2.

- E_T^{Had} (transverse energy in the hadronic calorimeter): Electrons deposit only
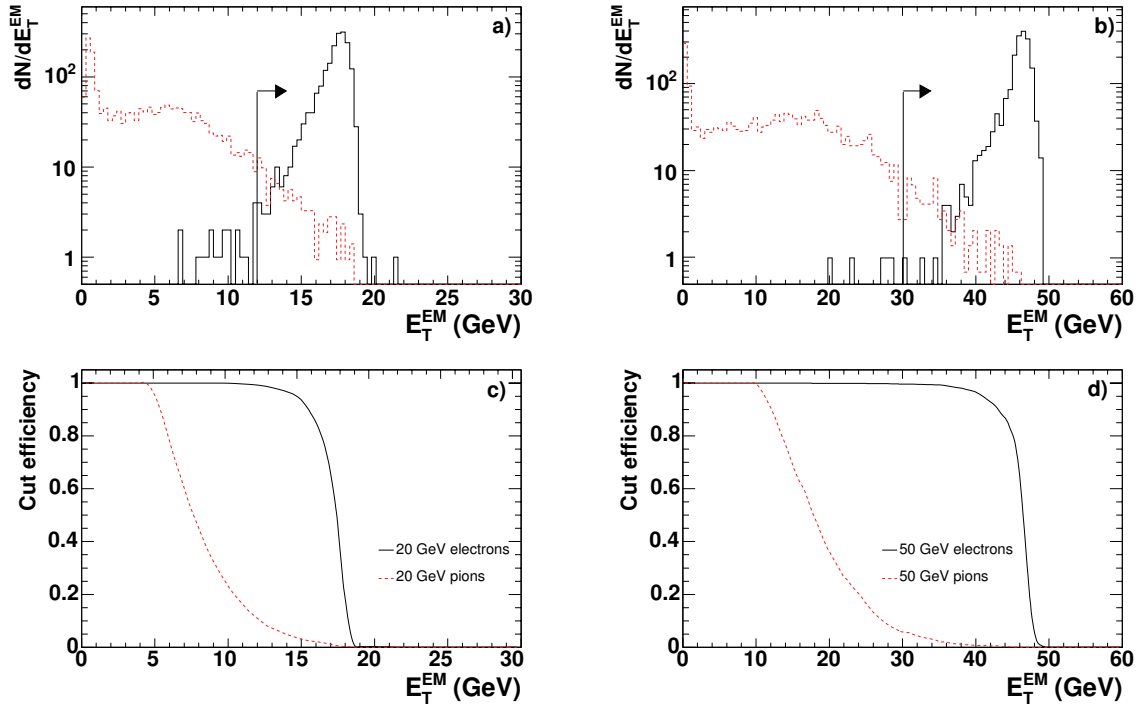
Figure 6.10: Transverse energy deposited in the second sampling of the EM calorimeter. Distributions are shown for 20 GeV, a), and 50 GeV, b), particles. The continuous line corresponds to electrons and the dotted one to pions. The arrow shows the selected events after the optimization done as explained in Sec. 6.4.2. Figures c) and d) show the efficiency of selecting the corresponding particles as a function of the cut in the E_T^{EM} variable, for 20 GeV and 50 GeV, respectively. No additional selection cuts in addition to the ones presented in Sec. 6.3 have been applied to the events shown.

a small fraction of their energy in the hadronic calorimeter (typically less than 5%). The transverse energy deposition in the hadronic calorimeter is therefore a good discriminator against pions, as it can be observed in Fig. 6.11. The cut efficiency for electrons at 20 and 50 GeV promptly reaches 100% below the 0.5 GeV cut, while for pions it increases smoothly, not reaching full efficiency before more than half of the pion energy.

– R_η^{shape} (lateral shape in the second sampling of the EM calorimeter): The shower shape created by an electron is usually more regular and narrower than the one created by a hadron, which tends to be more irregular and wider because of nuclear interactions. Thus, in order to distinguish between electron and pion clusters, the quantity R_η^{shape}[1] is calculated. The distributions for electrons and pions of 20 and 50 GeV are shown in Fig. 6.12. It can be observed that the distribution for electrons peaks close to one, indicating that their shower is rather well contained in a region of $\Delta\eta \times \Delta\varphi = 3 \times 7$.

---

[1]$R_\eta^{shape} = E_{3\times7}/E_{7\times7}$, the ratio of the energy sum of the cells contained in a $\Delta\eta \times \Delta\varphi = 3 \times 7$ cell window and the energy sum of the cells contained in a 7×7 cell window.
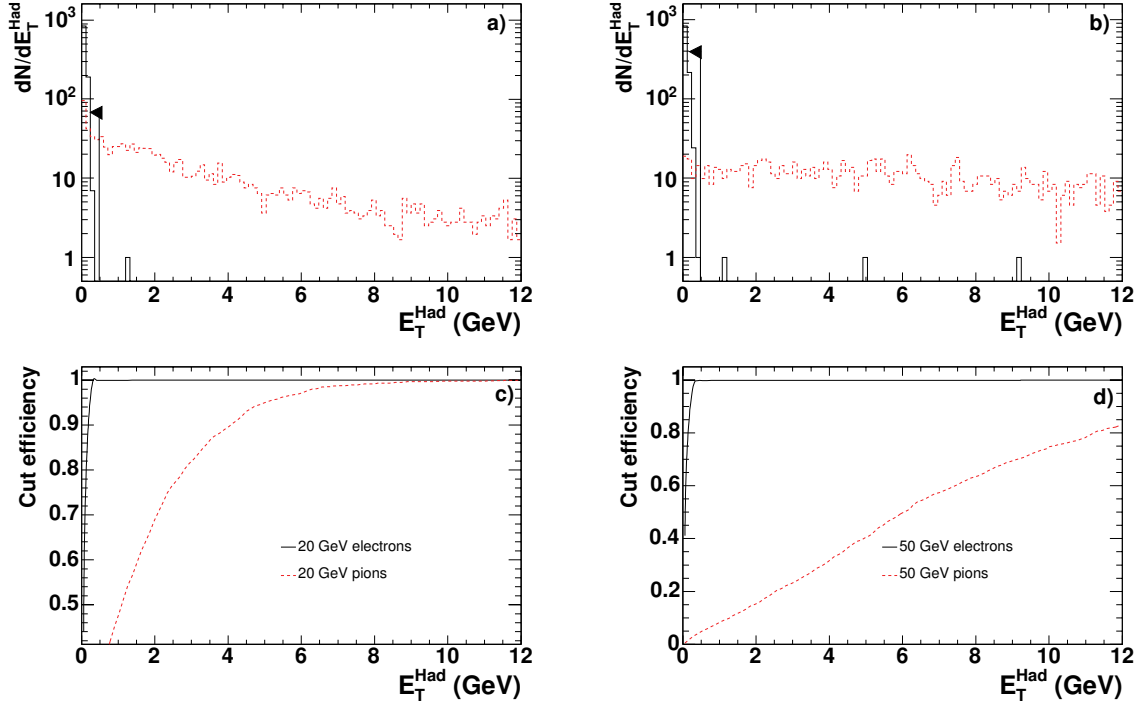
Figure 6.11: Transverse energy deposited in the first sampling of the hadronic calorimeter. Distributions are shown for 20 GeV, a), and 50 GeV, b), particles. The continuous line corresponds to electrons and the dotted one to pions. The arrow shows the selected events after the optimization done as explained in Sec. 6.4.2. Figures c) and d) show the efficiency of selecting the corresponding particles as a function of the cut in the E_T^{Had} variable, for 20 and 50 GeV respectively. No additional selection cuts in addition to the ones presented in Sec. 6.3 have been applied to the events shown.

– R_η^{strips} (lateral shape in the first sampling of the EM calorimeter): After applying the selection criteria based on the hadronic calorimeter and the second sampling of the EM calorimeter, only pions with very little hadronic activity and narrow showers in the calorimeter remain. The very fine granularity of the first sampling of the EM calorimeter can be exploited by looking for substructures and by analyzing the shower shape. The variable $R_\eta^{strips2}$ is a powerful discriminator against pions, as it can be observed in Fig. 6.13. In the case of electrons, E_1 and E_2 tend to be very different, resulting in values of R_η^{strips} close to one. For pions, it can happen that both energies are close to each other, producing values of R_η^{strips} close to zero.

– E_T/p_T (ratio between the cluster energy and the momentum of the reconstructed track): Track to cluster matching cuts are used to discriminate events where the EM cluster is due to an electron, or converted electron, from those in which the cluster is due to a photon or a charged or neutral hadron. One criteria that provides significant discrimination against pions is the ratio of

---

[2] $R_\eta^{strips} = (E_1 - E_2)/(E_1 + E_2)$, the fractional difference in energy between the first sampling cell with the maximum energy, E_1, and the second maximum energy, E_2.
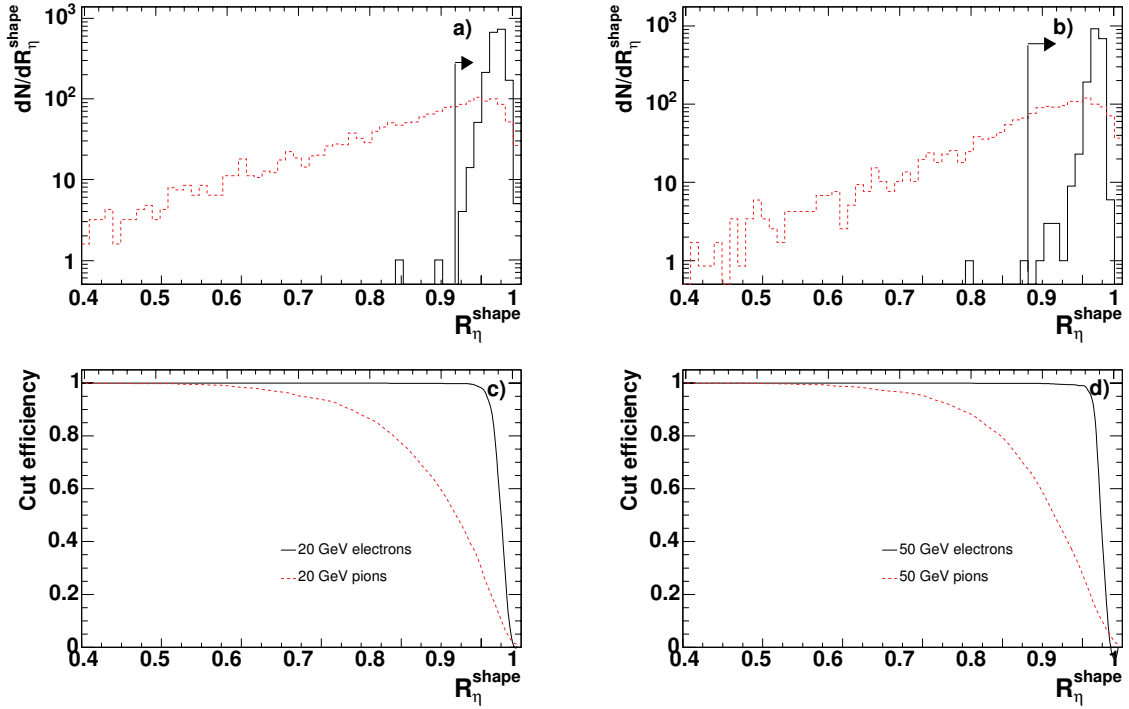
Figure 6.12: Lateral shape in the second sampling of the EM calorimeter. Distributions are shown for 20 GeV, a), and 50 GeV, b), particles. The continuous line corresponds to electrons and the dotted one to pions. The arrow shows the selected events after the optimization done as explained in Sec. 6.4.2. Figures c) and d) show the efficiency of selecting the corresponding particles as a function of the cut in the R_η^{shape} variable, for 20 and 50 GeV respectively. No additional selection cuts in addition to the ones presented in Sec. 6.3 have been applied to the events shown.

the transverse energy (E_T) of the cluster and the transverse momentum of the track (p_T). Ideally, for electrons, the E_T/p_T distribution would be a narrow peak at $E_T/p_T = 1$. Due to the effect of bremsstrahlung, the p_T of the particle is reduced, whilst the EM cluster frequently contains contributions from both the electrons and the bremsstrahlung photons, and therefore measures the initial E_T of the particle. As a result, the E_T/p_T distribution for electrons has a tail towards high values. On the other hand, charged pions usually deposit only minimum ionizing energy, or some random amount of energy if nuclear interactions occur between pions and nucleons. Their distribution usually peaks at lower values as it can be observed in Fig. 6.14. As explained in Sec. 6.3, there is no run of pions at 50 GeV with the first magnet switched on. As a consequence, there is no measurement of the momentum for these particles. This can be observed in Fig. 6.14 b), that shows an anomalous E_T/p_T distribution for the pion sample, coming from the fact that the fitted momentum distribution shows an arbitrarily high value.

– $\Delta\eta, \Delta\varphi$ (position difference between the cluster and the track): Due to the precision of the particle track and cluster reconstructed positions, the distance
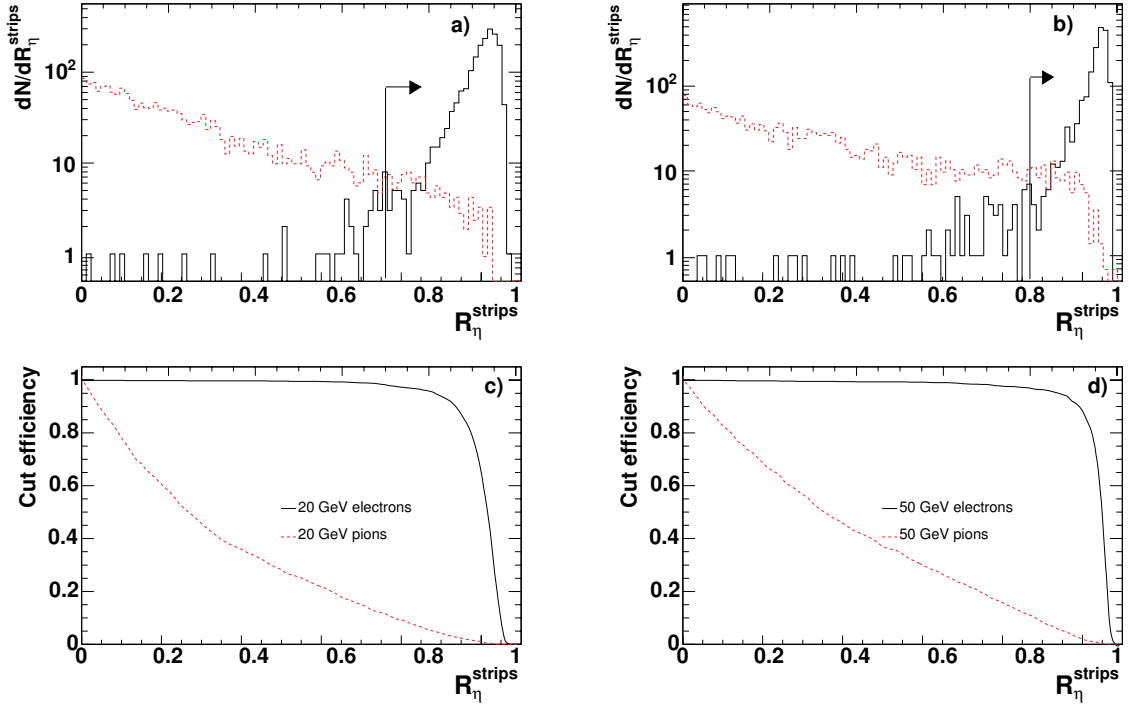
Figure 6.13: Lateral shape in the first sampling of the EM calorimeter. Distributions are shown for 20 GeV, a), and 50 GeV, b) particles. The continuous line corresponds to electrons and the dotted one to pions. The arrow shows the selected events after the optimization done as explained in Sec. 6.4.2. Figures c) and d) show the efficiency of selecting the corresponding particles as a function of the cut in the R_η^{strips} variable, for 20 and 50 GeV respectively. No additional selection cuts in addition to the ones presented in Sec. 6.3 have been applied to the events shown.

between the centroid of the cluster and the extrapolation of the corresponding track at the surface of the EM calorimeter can provide additional rejection against hadrons. The distribution of this distance, measured in $\Delta\eta$ and $\Delta\varphi$, is narrower for electrons than for pions, as it can be observed in Fig. 6.15.

6.4.2 Selection Optimization and Results

The variables described in Sec. 6.4.1 are optimized in order to obtain the best pion rejection by independently varying the limit for each variable, while retaining $\sim 90\%$ LVL2 overall selection efficiency on the electron subsample. The optimization is performed first on the calorimeter based variables, by manually tuning every selection criteria independently, trying to get the best pion rejection, while not loosing more than 4% of the electrons. Figures 6.10-6.13 are used as guidance in order to get a first set of optimal cuts, and then, some fine tunning is performed around these values. The cluster to track matching variables are then optimized applying the same criteria, and trying to obtain a final $\sim 90\%$ electron efficiency.

A set of optimized cuts are obtained separately for the 20 and 50 GeV samples. The values shown in Table 6.4 yield the best results. The performance achieved by the LVL2 single electron trigger using the optimization criteria described above is
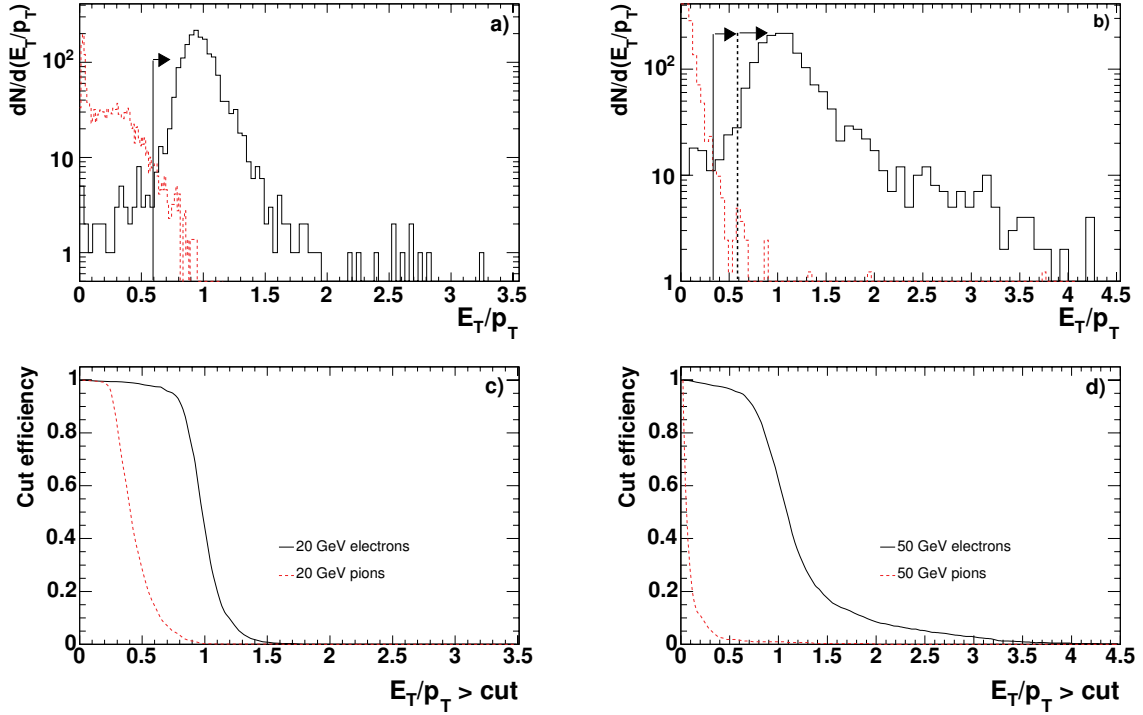
Figure 6.14: Ratio between the cluster energy and the momentum of the reconstructed track Distributions are shown for 20 GeV, a), and 50 GeV, b), particles. The continuous line corresponds to electrons and the dotted one to pions. The arrow shows the selected events after the optimization done as explained in Sec. 6.4.2. Figures c) and d) show the efficiency of selecting the corresponding particles as a function of the cut in the E_T/p_T variable, for 20 and 50 GeV respectively. No additional selection cuts in addition to the ones presented in Sec. 6.3 have been applied to the events shown.

given in Table 6.5. As it can be seen, for both energies under consideration, a pion fake rate of the order of seven per mil can be obtained for a LVL2 selection efficiency of around 90%.

As explained in Sec. 6.4 the magnetic field was switched off for the run of pions at 50 GeV. As a consequence, it is difficult to optimize the selection cut in the variable E_T/p_T. As a conservative performance estimate, the value of the cut is chosen to be the same as for the 20 GeV particles. These are the values given in Tables 6.4 and 6.5. As a cross-check the performance optimization has been done assuming that the distributions of E_T/p_T for pions in Figs. 6.14 b) and d) are correct. In this case, the 50 GeV electron LVL2 selection efficiency would be 87.12% and the pion fake rate would be four per mil.

During real data-taking in ATLAS, the selection optimization will be performed for the lowest possible particle energies, i.e. close to 20 GeV. Therefore, as a final cross-check, the performance has been calculated for 50 GeV electron and pions using the cuts optimized for the 20 GeV samples. The results, summarized in Table 6.5, show no performance degradation as particle energy increases.
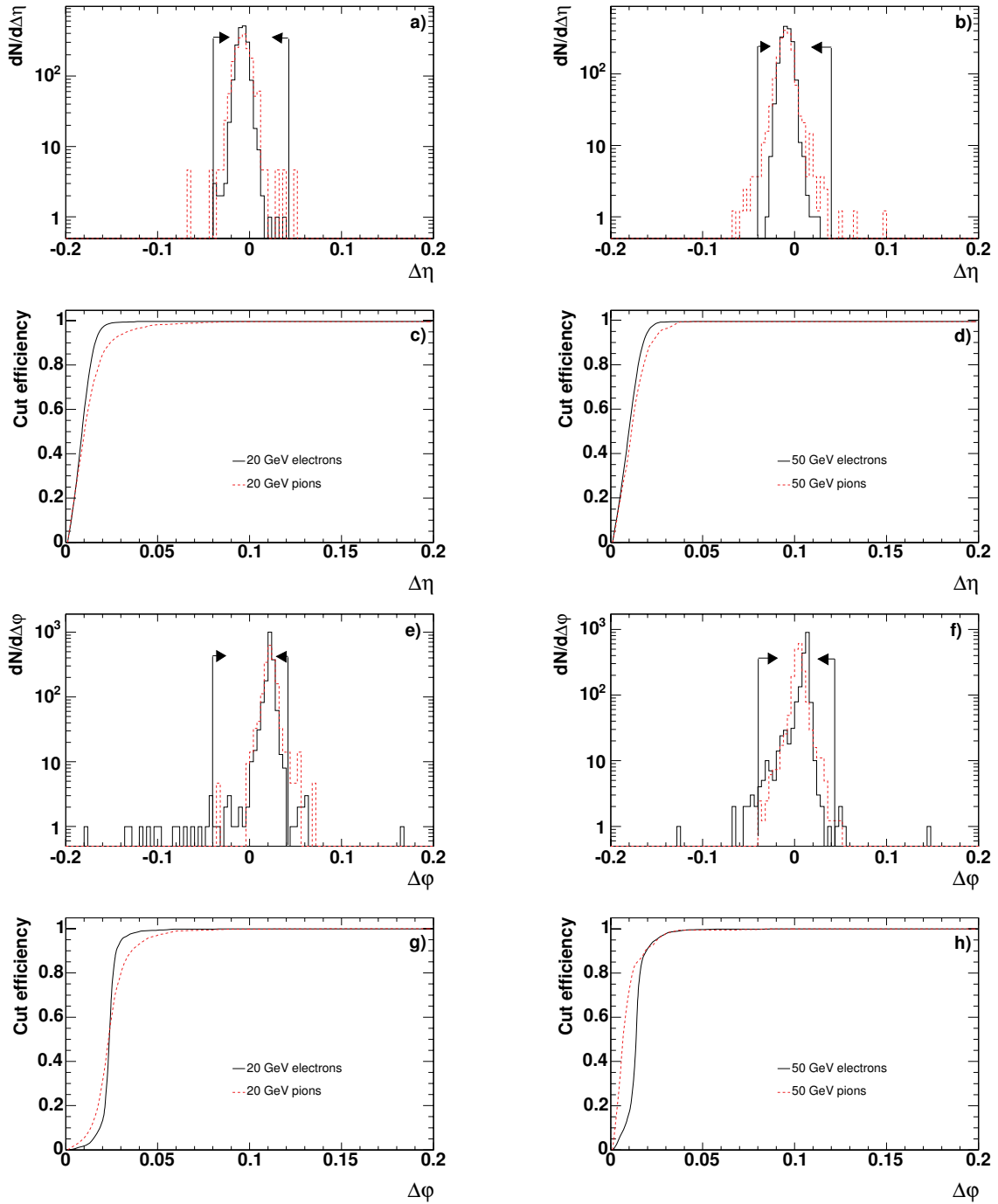
Figure 6.15: Position difference between the cluster and the track in the $\eta - \varphi$ coordinate system. Distributions are shown for 20 GeV, a),e), and 50 GeV, b),f), particles. The continuous line corresponds to electrons and the dotted one to pions. The arrow shows the selected events after the optimization done as explained in Sec. 6.4.2. Figures c), d), g) and h) show the efficiency of selecting the corresponding particles as a function of the cut in the $\Delta\eta$, $\Delta\varphi$ variable, for 20 and 50 GeV respectively. No additional selection cuts in addition to the ones presented in Sec. 6.3 have been applied to the events shown.

Sample Energy	E_T(GeV)	E_T^{Had}(GeV)	R_η^{shape}	R_η^{strips}	E_T/p_T	$\Delta\eta$	$\Delta\varphi$
	$>$	$<$	$>$	$>$	$>$	$<$	$<$
20 GeV	12.0	0.5	0.92	0.70	0.6	0.04	0.04
50 GeV	30.0	0.5	0.88	0.80	0.6	0.05	0.05

Table 6.4: Summary of the LVL2 electron identification cuts used in this study. They are optimized in order to obtain the best pion rejection rate, while retaining a $\sim$ 90% LVL2 overall electron selection efficiency.

Sample energy	Selection cut	Efficiency	Fake rate
20 GeV	LVL2 Calo	$(96.56 \pm 0.04)\%$	$(0.92 \pm 0.04)\%$
	LVL2 Matching	$(89.94 \pm 0.04)\%$	$(0.67 \pm 0.04)\%$
50 GeV	LVL2 Calo	$(96.05 \pm 0.04)\%$	$(0.33 \pm 0.04)\%$
	LVL2 Matching	$(90.02 \pm 0.04)\%$	$(0.07 \pm 0.04)\%$
50 GeV using 20 GeV tuned cuts	LVL2 Calo	$(97.56 \pm 0.04)\%$	$(0.51 \pm 0.04)\%$
	LVL2 Matching	$(91.27 \pm 0.04)\%$	$(0.04 \pm 0.04)\%$

Table 6.5: Efficiency results for 20 and 50 GeV samples. The cuts are tuned independently for both samples in order to have the best pion rejection, while retaining $\sim$ 90% LVL2 overall electron efficiency. The performance is also calculated for 50 GeV electron and pions using the cuts optimized for the 20 GeV samples.

6.5   Conclusions

The e/π separation performance by the LVL2 system of ATLAS has been studied in a full combined slice of the detector under the exposure to nominal beams of electrons and pions at momenta of 20 and 50 GeV/c. Pure samples of electrons and pions have been obtained using Cherenkov counters and the TRT subdetector. These samples have been used as input to the LVL2 system, where the high-p_T single electron trigger algorithms have been executed.

This study shows that using LVL2 calorimeter and calorimeter-tracking matching information, electron selection efficiencies of $\sim$ 90% can be obtained while maintaining the pion fake rate at a level of 7 per mil.

These results are comparable to the ones obtained in Ref. [8], where 2002 test beam data and offline selection algorithms were used and an electron selection efficiency of 90% was obtained for a pion fake rate of 5 per mil.

Bibliography

[1] ATLAS collaboration, *ATLAS Barrel Combined Run in 2004 Test Beam Setup and its evolutions*, ATC-TT-IN-0001, (2005)

[2] ATLAS collaboration, ATLAS: Detector and Physics Performance Technical Design Report, CERN/LHCC/99-15, (1999)

[3] B. di Girolamo, *MBPS Magnet Characteristics*, ATC-TT-EN-0006, (2003)

[4] ATLAS collaboration, *Proposed measurement program for H8 2004 muon system test*, ATL-COM-MUON 2004-006, (2004)

[5] S .Gonzalez, B .Gonzalez-Pineiro, T.G. Shears, *First Implementation of Calorimeter FEX Algorithms in the LVL2 Reference Software*, ATL-DAQ-2000-020, (2000)

[6] S. Gonzalez, T.G. Shears, *Further Studies and Optimisation of the Level-2 trigger electron/photon FEX algorithm*, ATL-DAQ-2000-042, (2000)

[7] N. Konstantinidis, H. Drevermann, *Algorithms to select space points of tracks from single primary interactions in ATLAS*, ATL-COM-DAQ-2003-040, (2003)

[8] L. Lu, Y. Gao, R. Strynowski, *e/π Separation in the Barrel Electromagnetic Calorimeter with 2002 Test Beam Data*, ATL-COM-LARG-2003-004, (2003)